UNIVERSITY
OF TRENTO - Italy
DEPARTMENT OF INDUSTRIAL ENGINEERING

XXVI cycle

Doctoral School in Materials Science and Engineering

Polyolefin nanocomposite with different types of nanofillers

Izabela Dąbrowska

November 2013

POLYOLEFIN NANOCOMPOSITES WITH DIFFERENT TYPES OF NANOFILLERS

Izabela Dabrowska

Approved by:

Prof. Luca Fambri, Advisor
Department of Industrial Engineering
University of Trento, Italy.

Prof. Alessandro Pegoretti, Advisor
Department of Industrial Engineering
University of Trento*, Italy.*

Ph.D. Commission:

Prof. Alberto Molinari
Department of Industrial Engineering
University of Trento, Italy.

Prof. Antonio Marigo
Department of Chemistry Science
University of Padova, Italy.

Prof. Frank Giesselmann
Institute of Physical Chemistry
University of Stuttgard, Germany.

Prof. Robert Dinnebier
Max Planck Institute for Solid State Research
Stuttgard, Germany.

Prof. Thomas Schleid
Institute of Inorganic Solid-State Chemistry
University of Stuttgard, Germany.

University of Trento, Italy.

Department of Industrial Engineering

November 2013

University of Trento - Department of Industrial Engineering

Doctoral Thesis

Izabela Dąbrowska - 2013
Published in Trento (Italy) – by University of Trento

ISBN: - - - - - - - - -

Abstract

The PhD project was details on the polyolefin nanocomposites compounding, processing and preparation. Two different types of polymer matrix with low melt flow rate for fiber forming polymers have been selected; high density polyethylene (HDPE) and isotactic polypropylene (PP). High density polyethylene was compounded with double layered hydrotalcite (LDH) while in case of polypropylene reinforcement by adding fumed silica and kaolinite was performed. In this way the influence of the nanofiller type on the thermo-mechanical properties of the prepared nanocomposites were studied.

In recent years several research efforts have been focused on the preparation of polymer/layered inorganic nanocomposites because of the excellent properties in comparison to the neat polymer. The main reason of this interest lies certainly in the properties of the nanoclay, like high stiffness, and high aspect ratio, that induce enhancement of various polymer properties (thermal stability, mechanical properties, flame resistance and gas barrier) even with small amount of filler. Moreover, nanocomposites can be processed more easily than microcomposite. Recently literature evidences a lot of progress in the nanofilled bulk materials; on the other hand, there are relatively a few publications on fibers made of nanofilled polyolefins. For instance, PP fibers were produced with various types of nanofillers, e.g. layered silicates, carbon nanotubes and montmorillonite. In the case of HDPE, composite fibers containing calcium carbonate, carbon nanotubes, silica and layered silicates were reported. It is worth to mention that so far, no publication could be found on this work using the same nanofillers with the same matrix.

This thesis is divided into six chapters; Introduction and Background, Experimental activities, after obtained Results with discussions are reported and finally Conclusions.

In the Introduction and Background (Chapter I and II) general information about nanocomposites and characteristic of different nanofillers type were

summarized. After that polymer processing method with particular attention on the melt extrusion and fiber spinning were described.

Third Chapter is dedicated to the experimental part. Here, the used material characterization, nanocomposite preparation procedure and description of experimental techniques were reported. All nanocomposites were characterized by different experimental techniques. First nanofiller morphology by microscope (SEM and TEM) and X-ray diffraction technique was tested. Thermal stability was investigated by Thermal Gravimetric Analysis (TGA) and crystallization behavior by Differential Scanning Calorimetry (DSC). Finally mechanical properties were characterized by tensile test, Dynamical Mechanical Thermal Analysis (DMTA) and creep test.

The Results and Discussion have been divided into two parts; first one was dedicated to the high density polyethylene layered double hydrotalcite nanocomposites (HDPE-LDH), while in the second polypropylene with fumed silica (PP-FS) and kaolinite (PP-K) nanocomposite were described.

i. High density polyethylene hydrotalcite (HDPE-LDH) nanocomposites after different process of plates and fibers production will be compared in Chapter IV. At the beginning a polypropylene matrix, suitable for fiber production, was firstly melt compounded with organically modified hydrotalcite up to 5% by wt. Similar compositions with up to 3% wt. of LDH were performed by melt spinning. The incorporation of the clay into both bulk and fiber nanocomposite enhanced the thermal stability and induced heterogeneous nucleation of HDPE. Hydrotalcite positively affected the mechanical properties in term of higher Young's modulus and tensile strength.

   After the preliminary characterization on bulk and as-spun material the fibers were hot drawn up to draw ratio (DR) 20. XRD analysis revealed intercalation with high degree of exfoliation for the composites with 1-2% wt. of LDH. For this compositions higher elastic modulus 9.0 GPa - 9.3 GPa (with respect to 8.0 GPa of the

neat HDPE), and maintain tensile strength and deformation at break were observed. Moreover, the addition of low amount of LDH significantly improved the creep stability.

ii. Nanocomposites of isotactic polypropylene fumed silica (PP-FS) were described in the Chapter V. Two types of hydrophobic fumed silica with different surface area ($170 m^2 \cdot g^{-1}$ and $150 m^2 \cdot g^{-1}$) and surface treatment (treated respectively by dimethyldichlorosilane and octylsilane) up to 2% vol. were used. Similar as in case of HDPE-LDH nanocomposites plates production and characterization was a preliminary step to select the best compositions for the fiber preparation. After that, the work has been focused on the iPP-FS fiber production. Introduction of the nanofiller enhanced thermal stability and mechanical properties of the nanocomposite. Elastic modulus at draw ratio 10 increased from 5.3 GPa for neat iPP up to 7.5 – 8.6 GPa for compositions with 0.25 – 0.5% vol. Together with this improvement enhancement in strength at break and maintaining deformation at break were observed. Moreover, isothermal creep tests evidenced improvement in the creep stability due to the FS introduction, over the whole range of investigated draw ratios.

iii. The last results of recent research dedicated to the polypropylene kaolinite (PP-K) nanocomposites are reported in Appendix 1. Nanocomposite fibers were successfully spun up to draw ratio (DR) 15 at very high nanofiller content up to 30% wt. The presence of kaolinite not only increased the thermal stability but also enhanced elastic modulus up to 5.6 GPa – 7.0 GPa for compositions with 1% up to 30% wt. of kaolinite, in comparison to 5.4 GPa for neat PP at draw ratio 10. Moreover, for the composition with 10% wt. of kaolinite better drawability with maximum modulus was obtained in comparison to neat PP.

Finally the most important observation made on polyolefin nanocomposites fibers were summarized in the Chapter VI. It can be concluded that polyolefin fibers nanocomposites were successfully prepared by two different processing conditions: melt compounding and melt spinning followed by hot drawing.

In case of plates the introduction of nanosilica remarkably improved the thermal stability and elastic modulus, with retention of the pristine tensile properties at break. Nanocomposites fibers showed a higher improvement of the elastic modulus with respect to the nanocomposites plates containing the same percentage of nanofiller. Moreover, the introduction of the nanofiller enhanced tensile dynamic mechanical properties especially for higher draw ratio. Similar behavior was also observed in case of creep compliance. Higher creep stability was observed for the drawn fibers with nanofiller in comparison to neat polymer. This behavior could be a consequence of the different orientation and morphology related to the crystallinity developed in the spinning. These results confirmed that polyolefin containing nanofiller could be easily spun into nanofilled fiber. TEM images revealed how the experienced improvements of the mechanical properties could be probably related to the orientation of nanofiller aggregates along the strain direction and to the consequent increase of the filler-matrix interfacial area.

It can be conclude that polyolefin nanocomposites were characterized by higher elastic modulus with maintaining stress and strain at break especially observed for drawn fibers. The most interesting results were the improvement of thermal stability and reduction of creep compliance of the polymer.

Table of Contents

List of Figures

List of Tables

List of abbreviation and acronyms

DMTA - Dynamic mechanical thermal analysis

DR - Draw Ratio

DSC - Differential Scanning Calorimetry

E - Elastic Modulus

E' - Storage Modulus

E'' - Loss Modulus

FS – Fumed Silica

FTIR - Fourier Transform Infrared

HDPE - High Density Polyethylene

K - Kaolinite

LDPE - Low Density Polyethylene

LDH - Layered Double Hydrotalcite

MFI - Melt Flow Index

PE - Polyethylene

PP - Polypropylene

SEM - Scanning Electron Microscopy

T_C - Crystallization Temperature

T_g - Glass Transition Temperature

T_M - Melting Temperature

TEM - Transmission Electron Microscopy

TGA – Thermo Gravimetric Analysis

WAXD - Wide-angle X-ray Diffraction

Chapter I

Introduction

Polymer fibers are widely used for various textile applications, such as automotive, carpets, geotextile, sail, or as reinforcements in composite materials. The most common polymers used for melt spinning are polypropylene, polyethylene, polyamides, or polyethylene terephthalate. The interest in the production of oriented polymers with high stiffness and strength dates back to 1960-1970. In the case of polyethylene drawn films Young's modulus of about 200 GPa and tensile strength of about 3 GPa were reported by Treloar [1]. However, molecular alignment achieved after melt spinning and drawing was much lower than predicted, as described by White et al. and in references therein [2]. The development of high modulus polyethylene fibers was presented in the pioneer research of Andrews and Ward, where a direct correlation between the draw ratio and modulus was established [3]. For instance, after increasing draw ratio from 7 to 13, Young modulus of cold-drawn fibers rose from 4 GPa to 20 GPa. Capaccio and Ward compared the drawing behavior of several commercial polyethylenes. They observed the best results for the polymers with low molecular weight and narrow distribution, analogously to the conclusions of White and co-workers [2, 4]. Nowadays polyolefins for fiber spinning have reached an extensive application, not only for economic reason, but also for easy processability, excellent melt dyeability and low moistures absorption [5-7].

Along with melt spinning, polyolefin fibers were produced by other processing and drawing methods, e.g. solid state hot drawing, solid state extrusion, gel-spinning of UHMWPE [8-10]. Solid state deformation was used by Ward and co-workers, who succeeded in stretching polymers in the solid state at temperatures sufficient to permit molecular mobility of polyethylene; thus they obtained Young's moduli of 70 GPa and tensile strength of 1.5 GPa at very high draw ratios (greater than 30) [11]. Melt spinning remains widely used processing method despite of the fact that that mechanical properties of produced fibers are lower than those of e.g. the gel-spun fibers [5].

The challenge to produce stronger, tougher, light-weight materials continues apace, being driven by demands for property improvements, economy, and material availability. In order to improve polymer properties, the introduction of small amount (up to 5% wt.) of inorganic nanofillers in polymer matrices is an interesting method. It is evident that nanocomposites offer similar or better properties at significantly lower filler loading levels than materials with conventional fillers. The addition of nanofillers to polymers makes possible to produce composite materials with improved mechanical and barrier properties, flame retardancy, electrical conductivity, etc [12].
Recent literature evidences a lot of progress in the nanofilled bulk materials; on the other hand, there are relatively a few publications on fibers made of nanofilled polyolefins. According to the ISI Web of Knowledge database, about 2 225 papers published in scientific journal in the period 1990-2013 contain the keywords "nanocomposite" and "fibers" [13].

Starting from these considerations, the aim of this work was mainly to compound nanocomposites based on polyolefins matrix, that still represents one of the most used and versatile polymers and investigate their thermal and mechanical properties. In order to evaluate the effect of the filler on the fiber properties, nanocomposites fiber were then compared with traditional composites in the form of plates. To achieve these purposes, different kinds of nanocomposites were considered:

- ***nanocomposite of high density polyethylene and organically modified hydrotalcite (HDPE-LDH).*** In this case nanocomposites were based on the HDPE matrix filled with low amount organically modified hydrotalcite if form of masterbatch. The nanocomposites were prepared by two different processing: melt compounding followed by a hot pressing process and melt spinning with further hot drawing in order to obtain nanocomposite in bulk and fiber form. Deep thermo-mechanical characterization was conducted to obtain information about the influence of nanofiller content and processing condition on the final material properties (see Chapter IV).

- ***nanocomposite of isotactic polypropylene and fumed silica (PP-FS).*** For this purpose two nanosilica types having different specific surface area and different surface treatments were used. Similar processing methods as in case of HDPE-LDH nanocomposite were applied in order to obtain bulk and fibers PP-FS materials. To study the influence of different silica type and different processing condition on the final properties different thermal and mechanical analyses were performed (see Chapter V).
- ***nanocomposite of isotactic polypropylene and kaolinite (PP-K).*** In this case polypropylene was reinforced by low and high (up to 30% wt.) kaolinite amount. Successful melt spinning and hot drawing up to draw ratio 15 was performed and the effect of the addition of a kaolinite on the final properties was evaluated (see Appendix I).

These nanocomposites were characterized mainly in terms of thermo-mechanical properties obtained after melt-spinning and drawing process because the literature offers limited data on the nanocomposites fibers. In particular:

- ***HDPE-LDH nanocomposites fibers*** were for the first time successfully produced during the melt-spinning process. Obtained fibers were characterized with a particular attention to the influence of nanofiller presence on the thermo-mechanical behavior after drawing process.
- ***PP-FS nanocomposites fibers*** performed from isotactic polypropylene with low melt flow rate were for the first time produced. During fibers characterization main focus was on the influence of nanofiller presence and nanofiller type on the thermo-mechanical properties obtained after hot drawing process.
- ***PP-K nanocomposite fibers,*** in this case particular attention should be focused on the successful spinning of the polypropylene fibers with high nanofiller content because of no literature available for PP-K filled nanocomposites fibers. This type of nanocomposite is still under

investigation and in Appendix 1 preliminary thermal and mechanical analysis with promising results were reported.

In addition to correlate the mechanical behavior with microstructure of the nanocomposite several techniques were applied. Scanning electron microscopy (SEM) and transmission electron microscopy (TEM) combined together with XRD techniques were employed to evaluate the filler dispersion in the matrix. In order to examine the crystallization behavior of composites differential scanning calorimetry analysis were conducted. The elastic modulus, the fracture behavior at yield and break and creep compliance were assessed by quasi-static tensile tests. Moreover, a more detailed analysis on the viscoelastic behavior of nanocomposites at different temperature was conducted by the dynamic mechanical thermal analysis.

The main target was to compare the results obtained for plates and fibers, to understand the influence of processing condition on the material behavior and finally to assess the influence of drawing process on the final nanofilled fiber properties.

Chapter II

Background

2.1. Polymer Nanocomposites

Polymer nanocomposites have been an area of intense industrial and academic research for the past twenty years. As compared to neat polymer or microcomposites polymers, polymer nanocomposites exhibit markedly improved properties like modulus, strength, impact performance, and heat resistance at low concentration of the inorganic components (1-10% wt.). In this context, the nanocomposites are lighter in weight and easier to be processed [14].
Polymer composites are distinguished by the characteristic size of the inorganic filler particles:

- traditional composites or micro-composites that contain micrometre-scale fillers;
- nanocomposites that contain nanometre-scale fillers, i.e. fillers that have at least a characteristic size less than 100 nm.

According to the nanofiller shape three types of nanocomposites can be distinguish:

- The first type of nanocomposites is characterized by only one dimension in the nanometer range. In this case the filler is present in the form of sheets of one to a few nanometer thick to hundreds to thousands nanometers long.
- When two dimensions are in the nanometer scale and the third is larger, forming an elongated structure, we speak about nanotubes or whiskers as, for example, carbon nanotubes or cellulose whiskers.

- When the three dimensions are in the order of nanometers, we are dealing with isodimensional nanoparticles, such as spherical silica nanoparticles obtained by in situ sol-gel methods [15] or by polymerization promoted directly from their surface [16], but also can include semiconductor nanoclusters [17] and others.

Due to the nanometer size these nanocomposites are characterized by remarkable improvement of mechanical, thermal, optical and physic-chemical properties in comparison to the neat polymer. The key factor in order to obtain all these advantages is good nanofiller dispersion. In other word, the potential problem in preparation is poor dispersion and distribution of nanoparticles in polymer matrix. Generally, agglomerations are highly dependent on dispersion of particles in a matrix, i.e. increase in the degree of particle dispersion results in decreasing particle agglomeration. On the other hand, distribution indicates how uniformly the primary particles or their agglomerates are distributed through the volume (Fig 2.1) [18].

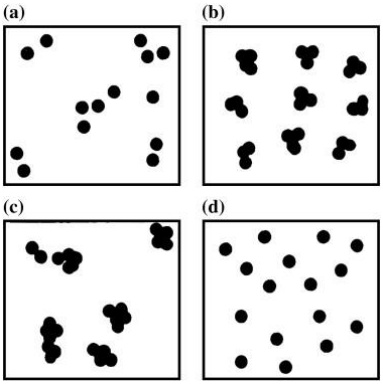

Figure 2.1. Schematic representation of the degree of dispersion and distribution of particles in a polymer matrix: (a) good dispersion, poor distribution, (b) poor dispersion, good distribution, (c) poor dispersion, poor distribution, (d) good dispersion, good distribution [18].

Therefore the processing becomes very important a several techniques were employed together with such as traditional melt mixing with twin screw extruder and injection moulding, solution mixing assisted with the aids of sonication and surfactants, in-situ polymerization. In addition, the dispersion can be improved with modification treatment of the filler surface in order to hinder agglomeration

phenomena: moreover these treatments can be employed to improve the filler-polymer interaction

Composites prepared in this way showed improvement in mechanical, thermal and electrical properties. However, because of complex interaction between the inorganic nanofiller and the polymer matrix it is difficult to construct a general scheme for the interpretation of the results available in the scientific literature on polymer based composites. For example, if one property changed for the better, another property changed for the worse. When nanocomposites are designed it is necessary to take this tendency into account and find the optimum properties for specific application.

2.1.1. Mechanical properties

The main reason for adding inorganic particles into polymers matrix is to improve its mechanical properties such as the tensile strength and elastic modulus. However, poor compatibility between the polymer matrix and the inorganic particles in nanocomposites prepared by simple physical mixing will create defects and consequently result in a deleterious effect on the mechanical properties of the nanocomposite [19]. Reddy *et al*. performed polypropylene (PP)/nano-silica (NS) nanocomposites [20] obtaining much higher modulus than that of neat PP and then epoxy-resin-grafted nanosilica composites. The tensile strength and elongation at break decreases for PP-NS because of nanosilica aggregation and a lack of interfacial adhesion between the matrix and filler. The mechanical properties of nanocomposites did not always increases, sometimes because of nanofiller aggregation in the matrix the properties are decreasing. We have to remember that nano-size particles have high surface energy and thus, they are easy to aggregate. To solve this problem, the amounts of inorganic particles were optimized or were functionalized by organic material called compatibilizer. For example, lower properties at break of poly (ethylene phthalate) (PET) nanocomposite with nano-TiO_2 fibres were assumed as weaker interaction between the PET macromolecules after titanium dioxide addition [21]. Also in case of polyester (PS) reinforced by ZnO nanoparticles both the tensile strength and elongation at break decreases. In this

case because of non-homogenous dispersion the interfacial adhesion was not strong enough the stand up to large mechanical forces [22].

2.1.2. Thermal properties

The presence of a tortuous diffusion path due to the complete dispersion of nanofillers in polymeric matrix can be exploited for a very important reduction of gas and liquid permeability of nanofilled polymers [23]. This is the same reason why the dispersion of nanofiller can affect the degradation temperature of the material. It is well known that exfoliated nanocomposites have in general significant higher degradation temperature than intercalated nanocomposite and traditional microcomposites [24]. As an example of the improvement of thermal stability PMMA/SiO_2 and PMMA/ZrO_2 nanocomposite described by Wang et al. are presented [25]. From the thermal degradation analysis the thermal decomposition temperature of both nanocomposite types was improved, because network structure between inorganic and organic components reduces the movement of polymer chains, and inorganic components may retard the attack of the free radicals [19]. Du *et al.* in his paper about LLDPE/MgAl - layered double hydroxide (LDH) nanocomposites focused on the crystallization behaviour of nanofilled materials. When 5% wt. of LDH was added the exothermic peak temperature increased to about 5°C [26]. It can be concluded that inorganic particles acts as nucleating agents, which have a heterogeneous nucleation effect on the crystallization temperature of polymer.

Moreover the flammability properties of many nanofilled systems can be strongly improved [27]. The studies of the flame retardant properties mainly demonstrate a significant decrease in the heat release rate, a change in the char structure, and a decrease in the mass loss rate during combustion in a cone calorimeter [28]. Building Fire and Research Laboratory (BFRL) research have shown that a new class of nano-based hydrotalcite – type additives for polymers acts as an effective fire retardant at levels that do not adversely affect the polymer properties. This new nano-flame retardant is also useful in fire-resistant coatings on steel and in flame-retarding thermoplastics.

2.1.3. Electrical and optical properties

Nanocomposites are closely related to the design of advanced devices for electronic and optoelectronic applications. Because the dimensional scale for electronic devices has entered the nano-range the utility of polymer nanofiller nanocomposites in this area is quite diverse like a photovoltaic cells and photodiodes, supercapacitors, sensors and light emitting diodes [19]. Polymer based nanocomposites are relevant for the anode, hole injection layer and light emitting layer. Silicon – based photovoltaic devices offer high efficiency, excellent stability and proven commercial utility. Conjugated polymers with various nanoscale fillers have been investigated for sensor application including gas sensors, biosensors and chemical sensors [29]. The market of materials for optical applications expands into the novel materials with functionality and higher transparency. Nanocomposites are also capable of achieving optical clarity of the materials because very small nanoparticles do not scatter light significantly. The transparency of the nanocomposites depends upon the size and distribution of inorganic nanoparticles in the matrix. Neat polyamide and hybrid films containing various amount of silica are transparent, the maximum transmittance was found in the hybrid film containing 5% wt. silica content in the matrix, beyond which the transmittance was gradually decreased [30]. Relatively good optical clarity has been obtained in many nanocomposites, in particular at low volume fraction. For example, in case of modified PMMA the optical clarity was maintained up to 10% wt. of bentonite. Moreover, the presence of nanoparticles may also significantly alter the original refractive index of the material [31].

Today, application of nanomaterials can be found in a wide variety of industries. Most common are electronics but also in synthetic textiles incorporating nanopowders that endow the fabrics with antibacterial, flame retardant, non-wetting or self-cleaning properties are becoming common. Thick coatings composed of nanoparticulate metal oxides are used in waterfast ink-jet media, while the thin coatings can be used for optical amplifying system for light-emitting diodes. Other applications can be found in buildings and construction, in automotive and aerospace component, and in environmental remediation and energy storage

technologies [12]. Obviously many other applications and interesting properties can be obtained by incorporating nanostructured materials in polymer matrix.

2.2. Layered crystals nanomaterials

Layered crystals nanomaterials refer generally to a particle filled materials where nanoparticles have only one dimension in the nanometer range. The nanofiller usually exist is from of sheet of one to a few (1-3) nanometers thick, and hundreds nanometers long, thus with very high aspect ratio (e. g. 10-1000) [32]. Layered inorganic crystals are able to swell the interlayer space and to modify their structure from microsize to nanodispersed particles forming intercalated/exfoliated nanocomposites [33].

There is a wide variety of both synthetic and natural crystalline fillers that are able, under specific conditions, to intercalate a polymer. Table 2.1 presents a list of possible layered host crystals. Among them layered silicates are the most common, particularly with polymer matrix, due to their availability as natural clay. Other interesting layered materials recently investigated in the field of polymer nanocomposites are layered double hydroxides.

Chemical nature	**Examples**
Element	Graphite
Carbon oxides	Graphite oxide
Metal phosphates	$Zr(HPO_4)$
Clays and layered silicates	Montrmorillonite, saponite, kaolinite, hectorite
Layered double hydroxides	$M_6Al_2(OH)_{16}CO_3 \cdot nH_2O$, M=Mg, Zn

Table 2.1. Example of layered host crystals susceptible to intercalation by a polymer [34].

Depending on the nature of the components used as reinforcement and the method of preparation, three main types of composites may be obtained when layered silicates is associated with a polymer (Fig. 2.2.).

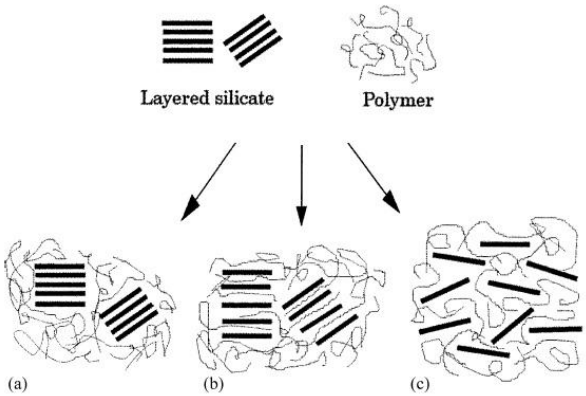

Figure 2.2. Scheme of different types of composite arising from the interaction of layered silicates and polymers: (a) phase separated microcomposite, (b) intercalated nanocomposite, and (c) exfoliated nanocomposite.

When the polymer is unable to intercalate between the nanofiller sheets is forming separated composite with similar properties as traditional microcomposites (Fig.2.2a). If the single or sometimes more than one polymer chain is intercalated between the silica layers intercalated nanocomposite is obtained. Exfoliated structure occurs when the nanofiller layers are completely and uniformly dispersed in a polymer matrix.

To investigate the structure of nanocomposite two techniques are usually used; WAXD analysis and transmission electron microscopy (TEM) observation. It can be observed in Figure 2.3a that WAXD technique let us to monitor shape, the position and intensity of the basal reflection peak from the distributed silicate layers. For intercalated nanocomposites, the layer expansion associated with the polymer intercalation results in the appearance of a new basal reflection what is related to larger gallery height. If we have exfoliated nanocomposites the extensive layer separation associated with the delamination of the original silicate layers in the polymer matrix results in the disappearance of any coherent X-ray diffraction from the distributed silicate layers. To support the results obtained from WAXD analysis, TEM observation allows us to qualitatively understand the internal structure and spatial distribution (Fig. 2.3b) [32, 35].

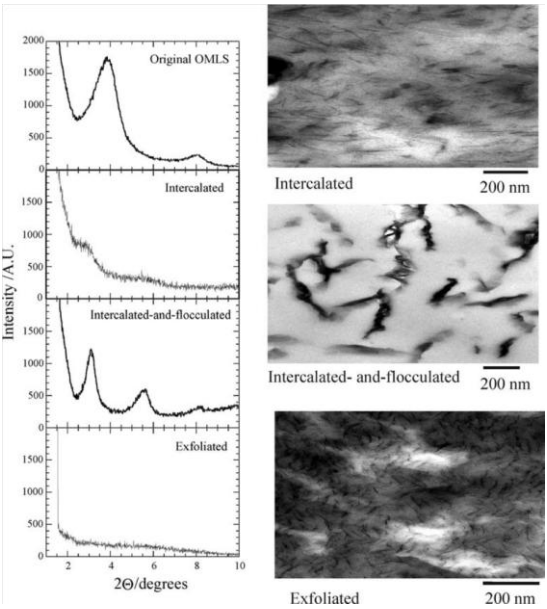

Figure 2.3. (a) WAXD patterns and (b) TEM images of three different types of nanocomposites [32].

2.2.1 Layered double hydroxides

Layered double hydroxides (LDHs) are a class of anionic clays whose structure is based on brucite ($Mg(OH)_2$)-like layers in which some of the divalent cations have been substituted by trivalent ions to form positively charged sheets. LDHs can be represented by general formula $[M^{II}_{1-x}M^{III}_{x}(OH)_2]^{x+} \cdot \left[(A^{n-})_{x/n} \cdot mH_2O\right]$, where M^{II} and M^{III} are divalent and trivalent metal cations, respectively, and A is the interlayer anion (Fig. 2.4) [33].

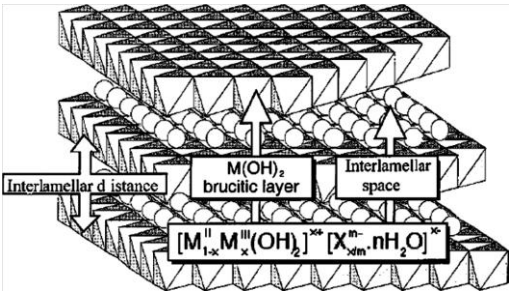

Figure 2.4. Layered double hydroxides structure [33].

LDHs consist of stacks of positively charged mixed metal hydroxide layers with hydrated anions between the sheets to maintain overall charge neutrality. This type of clay is available in both forms as natural and synthetic minerals, called hydrotalcite-like materials, resembling natural hydrotalcite which has the formula $Mg_6Al_2(OH)_{16}CO_3 \cdot 4H_2O$. Most LDHs are containing two kinds of metal cations within the hydroxide layers. The different type of cations have been introduced in the layers of the LDH materials, divalent cations as most of the transition metals of the first row combined with trivalent cations as Fe, Al and Ga [36, 37]. Moreover, also tetravalent cations such as Zr and Sn can be introduced into the nanofiller layers [38]. The presence of interlayer species is important because is directly related to the neat charge values and anion exchange capacity which is quite elevated rendering more difficult the nanocomposites formation [39]. Due to the hydrophilic characteristic LDHs materials are miscible only with hydrophilic polymers. Moreover, because of short intergallery spacing (7.6Å) they are not suitable for polymer chain intercalation. In order to modify these properties, like for example increase the interlayer distance, lower the surface energy and make intercalation with hydrophobic polymers possible, ion exchange modification with cationic or anionic surfactants is practiced [33]. The intercalation of LDHs occurred by following four different approaches:

- anion exchange of a LDH precursor;
- direct synthesis by coprecipitation;
- rehydration of a calcinated LDH precursor;
- thermal reaction.

2.2.2. Polyolefin – LDH nanocomposite

There are several methods reported in the literature to prepare the polymer/LDH nanocomposites. However, the existing synthesis methods involves mostly solution intercalation process, for examples, in situ polymerization [40], direct intercalation in polymer solution [41], in situ synthesis [42], which seems neither environment-friendly nor convenient. No much work has been reported on the melt-intercalation technique to prepare the polymer/ LDH nanocomposites, which is a nonsolvent, environment-friendly, and convenient process and has been extensively used to prepare polymer/MMT nanocomposites [32]. The LDH layers were dispersed in various polymers as for example poly (methyl methacrylate) [43], polyamide [44], nylon [45] and also polyolefines. In case of polyolefines study, it was shown that LDH in carbonate form does not exfoliate and intercalate PE chain during molten state dispersion [46]. For this reason sulfonate and stearated anions because of their easy intercalation and formation organic-inorganic hybrid with large interlayer distance were selected for the LDH modification [47]. However, from the literature review it is hard to have clear view about LDH reinforcement properties. For instance, LDPE-LDH nanocomposites modified with sodium dodecylbenzene sulfonate and MA-grafted HDPE as compatibilizer performed during melt-compounding did not show any significant change in the XRD analysis neither TEM observation. The processing gave only intercalated composites with LDH particles dispersed in the form of thin platelets [48-50]. On the other hand, complete exfoliation was observed for the composition HDPE/ZnAl-LDH performed by melt intercalation [51].

The LDHs nanocomposites similar as layered silicates can be used in order to improve mechanical, thermal, gas barrier properties, while the most promising field for polyolefin/LDH nanocomposites materials are fire retardants. Better thermal properties of these nanocomposites in comparison to MMT nanocomposites are related not only to the morphological structure but also are determined by the chemical components of the clay. In case of MMT nanocomposites the enhanced thermal stability was attributed to the protective charred layer formation by the MMT, while the LDH layers with very high activation energy prevents the diffusion of oxygen from gas phase into polymer nanocomposites, and thus not only protects the

C-C main chain but also hinders the dehydrogenation process of polymer molecules [33]. For example he thermal decomposition temperature measured at 50% mass loss for PE-g-MA/LDH with 2 and 5% wt. of modified LDH was around 50-60°C higher than that of PE-g-MA [52].

2.3. Fumed metal oxide nanoparticles

In 1941 high temperature hydrolysis process of metallic oxides in order to produce fine particle oxide was patented by Degussa. In 1950s was converted into large scale production and has become the process for the preparation of nanoparticles based on silicon dioxide, aluminum oxide and titanium dioxide [53].

Production

In the process the aerosol precursor in the form of a vapor is mixed with oxygen then fed into a reaction chamber and burned. For the pyrogenic silica production silicon tetrachloride vapor as the aerosol precursor is used [54].

The stoichiometry of the reaction can be represented by the equations:

$$2H_2 + O_2 \rightarrow 2H_2O \quad (2.1)$$

$$SiCl_4 + 2H_2O \rightarrow SiO_2 + 4HCl \quad (2.2)$$

In the same process the other metal oxides as aluminum and titanium are produced:

$$4AlCl_3 + 6H_2 + 3O_2 \rightarrow 2Al_2O_3 + 12HCl \quad (2.3)$$

$$TiCl_4 + 2H_2O + O_2 \rightarrow TiO_2 + 4HCl \quad (2.4)$$

Mixed oxides are produced from a vapor precursor mixture, for example, 99% $SiCl_4$ and 1% $TiCl_4$. During the aerosol process, depicted in Figure 2.5 the gas contains silica particles, gaseous hydrochloric acid; hydrogen, a small amount of chlorine leaves the furnace, and passes through a series of tubes to provide residence time for agglomeration. The flame temperature around 1500K causes the collision and coalescence of protoparticles, and primary particles are formed. The rate of coalescence affects the size of primary particles and this depends on the viscosity of the molten oxide, which is exceedingly high at a flame temperature. At lower

temperature, collision and sticking of primary particles only results in partial fusion and stable particle aggregates are formed. The silica aggregates leave the flame and cool, but they still collide. It can be observed that now agglomerates of aggregates are formed because the solid state surfaces are held together by physico-chemical surface interactions [73]. Nominal particle sizes for fumed silica range from 7 to 27 nm, and surface areas range from 100 to 380 m^2/g. Aluminum oxide has an average primary particle size of about 13 nm and a specific surface of about 100 m^2/g. Titanium dioxide has an average primary particle size of about 21 nm and a specific surface of about 50 m^2/g.

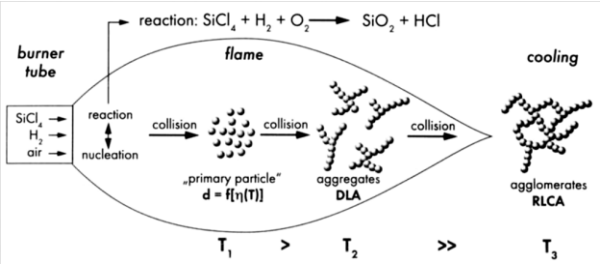

Figure 2.5. Production of fumed silica in a flame process [55].

Particle structure

When we are speaking about fumed silica we have to take into account enormous difference between extremely low bulk density in the range of about 20-50 $g \cdot l^{-1}$ and true density which is around 2200 $g \cdot l^{-1}$ [55].

The surface of fumed silica contains Si-O-Si units, in particular Si-O bonds which will at humid and ambient temperature form silanol groups that are highly reactive. Because of this the surface of fumed silica is highly reactive to chemical reactions, is chacterized by high surface energy and shows hydrophilic character. These properties in some cases are advantages, while it can also causes serious problems. Because of this that important is deactivation of the surface silanol by using alkylchlorosilanes, as dichlorodimethylsilane, or alkylsilazanes, as

hexamethyldisilazan, what will additionally lower the surface energy of the oxide and change fumed silica character from hydrophilic to hydrophobic (Eq.5.) [55].

$$SiO_{4/2} - Si - OH + 1/2[(CH_3)_3Si]_2NH + H_2O \rightarrow SiO_{4/2} - Si - O - Si(CH_3)_3 + 1/2NH_3 \quad (2.5)$$

Hydrophilic *Hydrophobic*

Applications

Due to the large surface area of metal oxide especially in case of fumed silica, and structure of finely dispersed particles variety of fascinating applications are offered.
The most important are reinforcement of elastomers as active filler and thickening of liquids as a rheological additive; both applications cover more than two thirds of the market. Smaller amount of fumed silica are used as free - flow additive in powder-like solids, for example, in toners for copiers and printers, in fire extinguishers, or even food. It also finds use in anti-foam agents, as anti-blocking, in cable insulation, catalysis, cosmetics, adsorbents, paper coating, pharmaceuticals, polishes etc. [53].
The most important properties of fumed silica oxides nanoparticles are their ability to increase viscosity and provide thixotropic effect (Fig. 2.6.). This property is related to the fact that hydrophilic fumed silica aggregates will very strongly interact in a nonpolar medium by hydrogen bonds between surface silanol groups of neighboring particles. This will cause aggregates that coalesce to form into large aggregates. After that the viscosity of the liquid increases greatly getting a gel-like consistence, resisting shear stress until it overcomes the strength of the particle-particle interactions caused by hydrogen bonds. Under shearing, breakdown of hydrogen bonds occurs and the agglomerates become smaller. This will decreases shear stress, then aggregates and small agglomerates will rearrange and restart to interact and grow to larger agglomerates. This will thickened again liquid by the silica, but as the rearrangement of particles requires time the system behaves thixotropic [55].

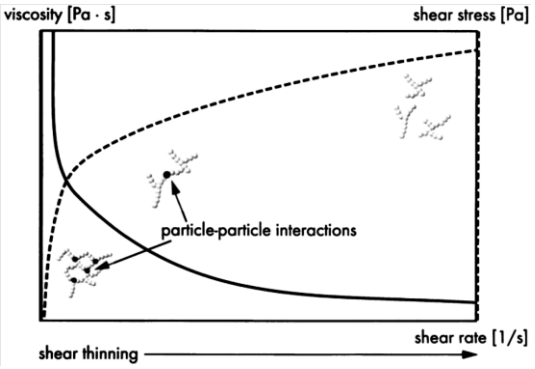

Figure 2.6. Thickening of liquids by fumed silica [55].

2.4. Melt extrusion process

Extrusion is used in all methods of polymer processing as either the main method of forming or as the method of transporting and metering the molten plastic before it is formed. This process covers wide range of application from continuous articles, such as sheets, tubes, fibres, films, it can be also used to mix together different polymers and to introduce the additives. During the extrusion process, high shear stresses are generated and these forces allow the additive to penetrate and disperse homogeneously in the molten polymer. The components of the extrusion line are: polymer feeder, extruder, die, cooling system as shown Figure 2.7 [56].

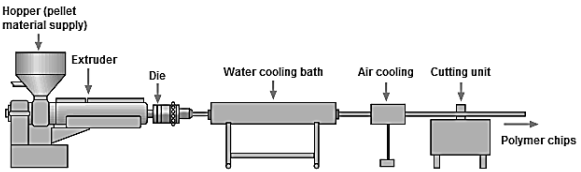

Figure 2.7. The basic component of an extrusion line.

The melting extrusion process is carried out using an extruder – barrel containing one or two rotating screw that transport material down the barrel. Extruders consist of four distinct parts:

- an opening though which material in form of powder or pellets enters the barrel equipped with a hopper filled with the material for extrusion or material can be continuously supplied by external feeders,
- a processing section containing the barrel and the screw(s) that transports and mix the material,
- an die for shaping the material,
- downstream equipment for cooling, cutting and collecting the final product [57].

There are two types of extruders: single- and twin- screw extruders as reported in Figure 2.8.

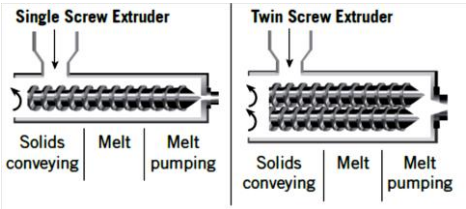

Figure 2.8. Cross-section of single and twin screw extruder barrel.

The diameter (*D*) and the length (*L*) of the screw are the fundamental parameters of the extruder; the first defines the maximum flow rate, while the length/diameter ratio (L/D) defines the ability of mixing extruder.

Single screw extruder is usually used for melting and conveying the polymers, while twin screw is applied for melt-mixing with additives like for example pigments, reinforces and fillers. Where the homogenous and consistent mixing is required in order to obtain good material dispersion the twin-screw extruder is preferred. In this type of screw melting is accomplished by frictional heating within the barrel, the material undergo shearing between rotating screw and between screws and the wall of the barrel. Moreover, the twin screw extruder shows some advantages compare to single screw extruder: higher capacity, narrow range of the residence time, auto cleaning of screws and possibility to work with thermally sensible materials [56].

The screws are generally divided in the three areas: solids conveying, melt and melt pumping, as represented in Figure 2.8.

Solids conveying (feeding zone) - in this zone polymer form inside the hopper fall by gravity into the heated cylinder where the screw rotation begins. In this area the height of the threads of the screw is high and constant and the granules occupy a very high volume due to high voids.

Melting zone (compression zone) - the molten polymer is compressed and transported by the screw threads. The melting occurs due to the heat exchange and friction with the walls of the extruder. In this area the height of the threads decreases and then increases the diameter of the core of the screw, resulting in an increase of the pressure and compression of the polymer. The compression in this area eliminates the cavities and gas incorporated into the molten polymer.

Melt pumping zone (metering zone) - in this area pressure required to push the molten polymer through the die is generated. The height of the thread is defined as a function of the mixing and processing requirements [56].

The screws can be counter-rotating (Figure 2.9a) and co-rotating (Figure 2.9b). The counter-rotating screws, is the most favorable from polymer flow point of view, which is generated in a positive way by the interpenetration of the surfaces of the screws. The co-rotating screws extruder, in the contact zone the circular speed of the screws are in opposite directions while the compartments between the two threads in the same area are considerably larger. The first are suitable for the profiles extrusion, while the second is widely used in the mixing process [57].

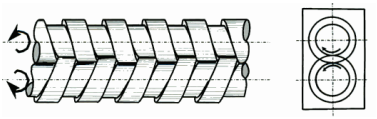

Figure 2.9a. Scheme of the co-rotating screw

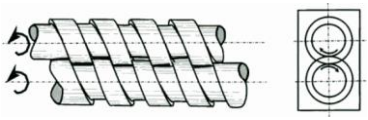

Figure 2.9b. Scheme of counter-rotating screw

The twin-screw extruders are usually used to provide different type of mixing and transformation condition. For this reason during product development modular screw with multiple elements, as reported in the Figure 2.10, allow to tailoring and optimizing the processing condition are designed [56].

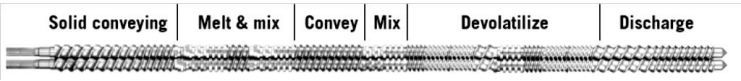

Figure 2.10. Various mixing zones of complete modular screw.

2.5 Fibre production process

The fibers of polyethylene, in particular, are among the most resistant and light fibers in the world. Their resistance may become 10 times higher than steel and about 40% higher than that of the aramid fibers. These fibers also have a good resistance to chemicals, water and abrasion. From 1966 to 1970 an increasing interest in the oriented polymer production with high tensile modulus (>40GPa) and strength (>1GPa) were observed. To achieve this, two routes were followed: synthesis of normal polymers with very rigid units in the polymer chain and novel processing in order to give fully extended molecular chain from flexible polymer. Both of this routes gave satisfactory results, first one by synthesis of the aramids (*Kevlar* and *Twaron*) and the second by high drawn polyethylene (*Dyneema* and *Spectra*) [7]. These fibers are used in various technological fields, like for example to perform bulletproof vests, helmets, lines, ropes and harnesses for the marine, fishing nets or hail and as reinforcing element for the production of composite materials. The high strength polyethylene fibers can be produced with different methods as melt spinning and spinning from solution or gel. This last method involves the use of an appropriate solvent in which the polymer is soluble. This technique is commonly used in case of ultra-high molecular weight polyethylene (UHMWPE) because of its very high viscosity in the molten state. In general, the process of spinning from solution is also employed in the case where polymer degrades in the melt processing temperature. In case of UHMWPE fibers produced by gel spinning elastic moduli can reach values of 70GPa and tensile stress at about 2.7 GPa but, due to the nature of the production method, they are very expensive [7].

The process of melt spinning is an attractive alternative for the production of fibers from low molecular weight polyethylene. This process, do not required the use of

solvent; it is cheaper and more environmentally friendly than the spinning process from the solution. The polyethylene fibers produced by melt spinning generally have worse mechanical properties than those produced by gel spinning. In order to improve these properties is necessary to apply very high stretching ratios [58].

The stretching ratio, often referred as DR (draw ratio) is given by the ratio of the initial section of the fiber and the final section of the stretched fiber. If mass flow of material during the stretching process is constant, the stretching ratio is also given by the ratio between two speeds; the released and collecting drums speed.

$$DR = \lambda = \frac{A_i}{A_f} = \frac{D_i^2}{D_f^2} = \frac{v_f}{v_i} \quad (2.6)$$

Where D_i and D_f are respectively the diameter of the fiber before and after drawing.

Melt spinning process

The melt spinning process is diverse from the processes of spinning from solution for the absence of the solvent. It is often used to produce polyolefin fibers, of polystyrene or nylon 66. The schematic illustration of this process is depicted in Figure 2.11.

Melt spinning is a specialized extrusion process that employs a spinneret to form multiple continuous filaments which form polymeric fibers after solidification. The polymer material, generally in the form of granules or powder is used. The polymeric melt is forced out through tiny holes of a device called a spinneret in the form of high viscosity continuous polymer filaments which are solidified by cooling/quenching. In most cases the holes have circular cross section, but can also have different shapes. Once exit from the die, the filaments are cooled by air or water and are collected on the rotating drums [59]. The higher the speed of collecting rate, the smaller the final section of the fiber.

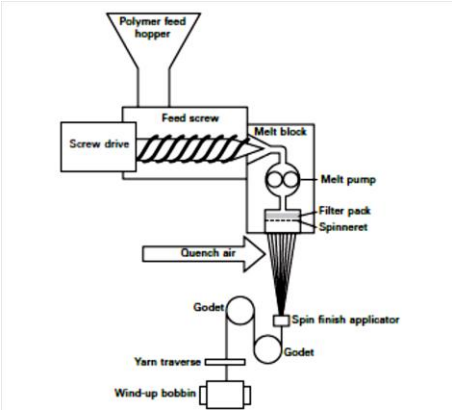

Figure 2.11 Schematic illustration of the melt spinning process.

Spun filaments of low orientation are subjected to a stretching or drawing process to convert it into commercially useful fibers of high orientation. The process involves passing the filaments around driven rollers with successively higher speed to produce the degree of stretch (draw ratio) required. To obtain a uniform product, it is necessary to draw at temperature above the glass transition temperature. The process of drawing introduces some crystallinity into the filaments, but insufficient to stabilize them against thermal shrinkage during further processing and usage [60]. The spinning process, determines the internal structure of the fibers. Several investigators have studied the molecular orientation developed in melt-spun polyethylene fibers [61]. Dees and Spruiell proposed the morphological model reported in Figure 2.12.

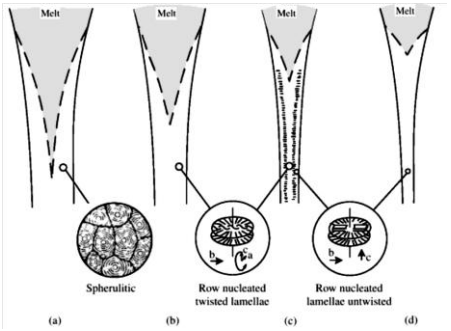

Figure 2.12. Model of morphology development in as-melt spun HDPE filaments [62].

In most cases, the fiber obtained by melt spinning is subjected to a further process of drawing to maximize its mechanical properties, working at a temperature slightly lower than the melting point. The high temperature, coupled with the condition of uniaxial tension imparted by stretching process, contributes to increase the degree of alignment of the polymer chains along the fiber axis and consequently the elastic modulus and stress at break are improved. The heating of the fiber can be performed in a simple oven or in an oil bath.

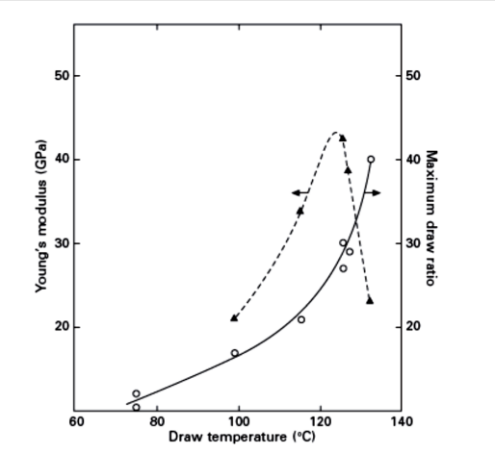

Figure 2.13. Plots of maximum draw ratio attainable (○) versus draw temperature for high molecular weight linear polyethylene, (▲) the values of the corresponding room temperature moduli for different draw ratios [7].

In the Figure 2.13 is reported that by increasing the drawing temperature higher molecular weight samples could be drawn to higher draw ratios, for example in case of linear PE with $M_w=8\cdot10^5$ maximum draw ratio was equal 40. However, above 120°C flow drawing occurs where there is a reduction in cross-section but the molecular network is not being extended effectively to increase moduli [7].

2.6. Polymer fibres – structure development

The polymer fiber development firstly focused on the polyvinyl and polyvinylidene fibers starts in the 1920s. The major breakthrough in this field was a synthesis of nylon 66 and nylon 6, by Carothers in the 1930s. However, more important from the structural point of view was the development of melt spinning. Subsequently, polyethylene terephthalate (PET), now the most produced textile fiber, was synthesized and melt spun with tensile strength of around 1.0 GPa (0.72 N/tex) and elongation at break of around 10%, while undrawn PET fibers have values of around 100–200 MPa and 300–500%, respectively [63]. In case of polyethylene, ordinary polyethylene fibers have a strength of around 200–300 MPa while high-strength PE fibers produced through the gel spinning and super-drawing processes of ultra-high-molecular weight polymer reach 3 GPa. These big differences in the properties are related to the different arrangement of molecular chains in the fiber developed during processing.

Fiber structure

Synthetic polymers are classified into crystalline and amorphous, moreover from the processing point of view the crystalline polymers are divided into two groups; depending if their glass transition temperature (T_g) is higher (for example PET, PA66, PA6) or lower (PE, PP) than room temperature (T_R). Synthetic fibers are produced from crystalline polymers mainly because of high heat resistance. This classification is useful to understand fundamental mechanisms of fiber structure formed during melt spinning and drawing processes. Spinning process can be achieved by either melt spinning or solution spinning. Because of the simplicity, low production cost and environmental friendliness more common is melt spinning [63].

To discuss the mechanism of structure development in the fiber production we have to come back to the glass transition temperature classification that was reported before. Polymers with $T_g > T_R$ are characterized by low crystallization rate, after melt spinning molten polymer is cooled down and after solidifies in form of fibers. In this

way amorphous with low molecular orientation fibers are formed. During drawing process, such fibers are heated up to a temperature slightly higher than T_g in order to improve molecular mobility and stretched while crystallinity content will be still low. Then fibers pass through an annealing zone where temperature is between T_g and T_m to gain higher crystallinity. It can be concluded that polymers with glass transition higher than room temperature required multiple-step drawing and annealing with increasing temperature to apply high drawing tension and a high annealing temperature [63].

In the case of polymers with $T_g < T_R$ crystallization has to occur during spinning process to obtain solidified fibers. Drawing temperature for this type of polymers should be higher than its crystalline dispersion temperature to allow gaining enough mobility to molecules in the crystals. However, in many cases the molecular mobility of the polymers in this category is fairly high and the drawing of those fibers can be carried out even at room temperature. In this stage highly oriented structure through destruction and reorganization of crystallites may progress. Similar as in case of polymers with $Tg > T_R$ an additional annealing process may be necessary to obtain a well-ordered and stabilized structure Differences in the structure development behavior in the spinning and drawing processes of the two types of polymers are schematically summarized in Fig. 2.14 [63].

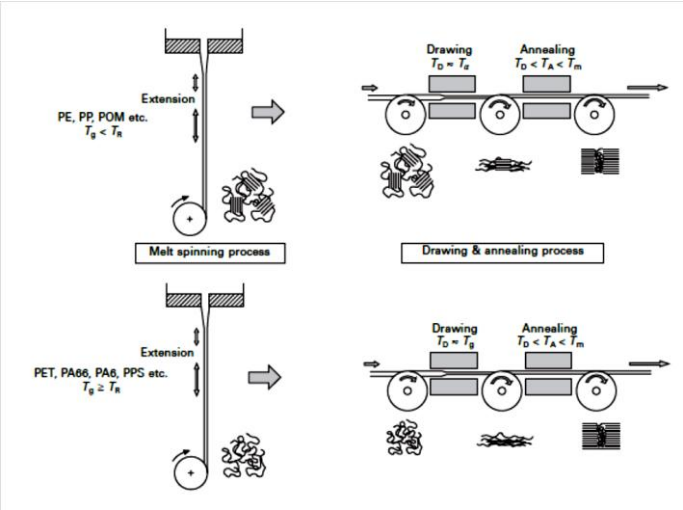

Figure 2.14. Schematic of structure formation behavior during spinning and drawing process for the polymers with their T_g higher and lower than T_R. T_g –glass transition temperature, T_R – room temperature, T_m – melting temperature, T_D – drawing temperature, T_A - annealing temperature and T_α - crystalline dispersion temperature [63].

Fundamental mechanism of molecular orientation

Molecular orientation in the molten polymer generally follows the stress-optical rule (SOR) which is based on the correlation between the developments of entropic stress and optical anisotropy of elongated chains. SOR rule can be written in following formula:

$$\Delta n = C\sigma \tag{2.7}$$

where Δn is birefringence, σ is the tensile stress and C is the stress-optical coefficient described by following equation:

$$C = \frac{2\pi}{45kT}\frac{(n^2+2)^2}{n}(\alpha_1 - \alpha_2) \tag{2.8}$$

where k is the Boltzmann constant, n the mean refractive index and α_1 and α_2 are the polarizability of the segment in the parallel and perpendicular directions to the molecular chain axis respectively. If the intrinsic birefringence of the melt polymer can be defined as Δn_c^*, the orientation factor f can be described as follows:

$$f = \frac{\Delta n}{\Delta n_c^*} = C^*\sigma \tag{2.9}$$

where C^* called the stress-orientation coefficient, represents the orientability of polymers in the flow and should be related with the molecular chain rigidity is described by following equation:

$$C^* = \frac{C}{\Delta n_C^*} \tag{2.10}.$$

In Table 2.3 stress-optical coefficients and stress-orientation coefficients of various polymers were compared [63, 64].

Polymer	Stress-optical coefficient C [GPa^{-1}]	Intrinsic birefringence Δn_c^*	Stress-orientation coefficient C* [GPa^{-1}]
Polyethylene (PE)	1.2	0.12	10
Polypropylene (PP)	0.8	0.06	13
Polyamide 6 (PA6)	1.8	0.09	19
Poly(ethylene terephthalate) (PET)	4.9	0.22	22
Poly(ethylene naphthalate) (PEN)	13	0.49	27

Table 2.2. Stress-optical coefficients and stress-orientation coefficients of various polymers.

It can be concluded that the rigid polymers (the one heaving high stress optical coefficient) can be aligned easily in a molten state during spinning process, while it would be more reasonable to align flexible molecules such as those of PE and PP in a solid state using the drawing process [64]. However, orientation developed in solid state is governed by the degree of deformation i.e. the draw ratio is uniaxial stretching.

Fundamental mechanism of crystallization under non-isothermal conditions

The crystallization in the fiber processing occurs under anisotropic and non-isothermal conditions. The time-course increase of crystallinity can be described by Avrami equation:

$$\frac{X(t)}{X_\infty} = 1 - exp\left[-(Kt)^{n^*}\right] \tag{2.11}$$

where *X(t)* is the crystallinity at time *t* and X_∞ is the infinite crystallinity, *K* is the crystallization rate constant and *n** is the Avrami exponent. The Avrami equation can be extended to the equation for the non-isothermal crystallization as follows:

$$\frac{X(t)}{X_\infty} = 1 - exp\left\{-\left[\int_0^t K(t)dt\right]^{n^*}\right\} \tag{2.12}$$

The exponential function corresponds to the imaginary non-dimensional volume of the crystal without the effects of overlapping and impingement during the crystal growth. It is well known that crystallization does not occurred at temperature below T_g and above T_m and has a bell-shaped curve with a maximum around the midpoint of T_g and T_m [63]. Crystallization in the melt spinning process occurs under the cooling condition and it occurred at a constant temperature where the heat removed by the cooling and the heat generated by the crystallization are balanced and were depicted in Figure 2.15. Figure 2.15.a represents behavior of polymers with $T_g<T_R$ (PP, PE) and Figure 2.15.b polymers with $T_g>T_R$ (PA6, PA66, PET). From this diagram it can be easily understood that the crystallization temperature becomes lower with the increase of cooling rate. In the slow cooling range the behavior of both polymers type is similar, however in the rapid cooling there can be condition where

there is no intersection point between the crystallization and cooling rate lines. This condition may affect amorphous fibers production [65].

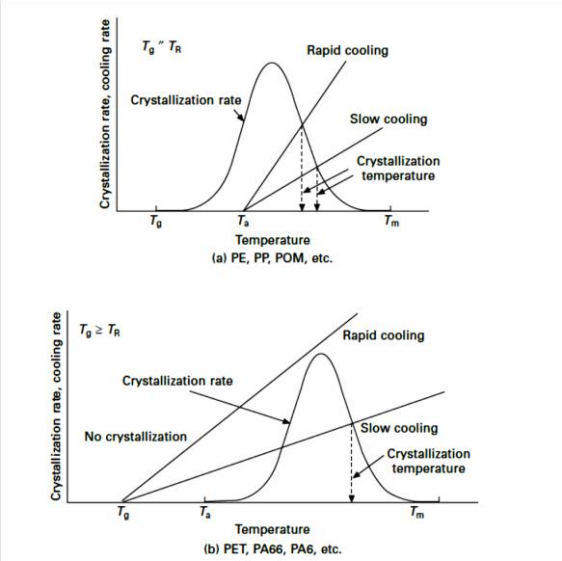

Figure 2.15. Schematic relation between temperature - dependent crystallization rate curve and cooling rate line of different cooling rates a) polymers with $T_g<T_R$ and b) polymers with $T_g>T_R$ [7].

2.5. Properties of oriented polyolefins

Elastic modulus

The main effort to orient polyolefines to high degrees is made in order to improve mechanical properties, especially tensile modulus. Till now the highest reported experimental elastic modulus have been in range 230-264 GPa [66]. The reason of the extremely high modulus of oriented material in comparison to typical specimens (around 1GPa [67]) is related to the different tensile deformation of isotropic samples that involves deformation of molecules which is largely accommodated by bond rotation. In case of oriented sample we have to use force to extend the configuration which involves bond elongation. As it is reported on the Figure 2.16 the elastic

modulus increases monotonically with the draw ratio. There are many factors that affect the molecular orientation as for example; an absence of branches, high molecular weight and elevated temperature but not higher than T_m.

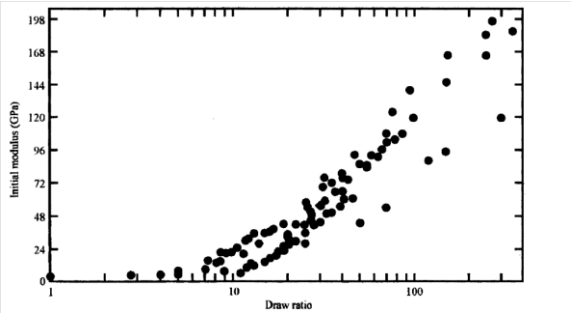

Figure 2.16. Tensile modulus as a function of draw ratio for the samples oriented in the solid state [68].

Since, for high modulus values high molecular orientation induced by high draw ratio is required the maximum achieved modulus is a function of the maximum draw ratio. For melt-crystallized samples following equation which takes into account entanglement density and the square root of the molecular weight has been proposed [69]:

$$Maximum\ draw\ ratio = M^{\frac{1}{2}}/20.8 \qquad (2.13)$$

where *M* is molecular weight. To approach the values estimated from this equation, it is necessary to introduce even higher draw temperature as the molecular weight increases. While the modulus can fall when the deformation temperatures will reach a value at which molecular relaxation occurs faster than orientation process [70]. This value is related to the drawing rate and molecular weight of the sample. Usually the effect of the relaxation can be counteracting by faster orientation and higher molecular weight.

Tensile strength

Tensile strength values are related to the molecular characteristic of the resin and its degree of entanglement. Usually tensile strength initially increases with the degree of

molecular orientation but levels off or passes through a maximum at higher draw ration. For example in case of melt-crystallized ultra-high molecular weight PE tensile plateau is observed at draw ratio of approximately 9 for drawing temperature equal 120°C [65]. For lower molecular weight the maximum occurs at higher draw ratio. For example for linear polyethylene resin with average molecular weight 224.000 is around 20-35 and around 30-40 for resin with molecular weight equal 115. 000 [71]. It has been discovered that leveling off of tensile modulus is caused by the dominant chain slippage process occurred during drawing process [72]. It can be concluded that high tensile strength is promoted by high molecular weight, narrow molecular weight distribution, reduced entanglement density, and high draw ratio. The highest tensile strength equal 9.9 GPa was obtained for individual hot drawn fibers of ultra-high molecular weight PE. The average vales observed for melt-crystallized samples are around 0.8-1.3 GPa obtained at draw ratio of 15 and 20 [71, 72].

Elongation at break

The elongation at break is inversely proportional to their orientation. The relation between draw ratio and elongation is reported in Figure 2.17. In case of ultraoriented fibers the elongation is not higher than 10% at room temperature.

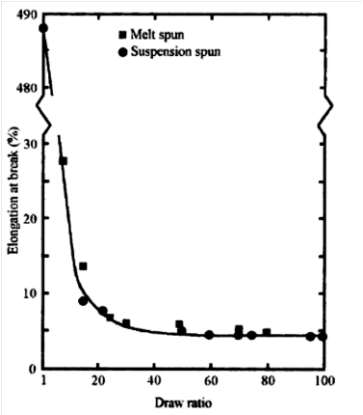

Figure 2.17 Elongation at break as a function of draw ratio.

The maximum elongation at break can be described by the following equation:

$$DR = 1 + \frac{e(\%)}{100} \quad (2.14)$$

$$\varepsilon = \ln DR \quad (2.15)$$

where e and ε are engineering deformation and the deformation at break respectively.

Following assumptions can be considered:

- each fiber has a maximum failure strain ε_{max}
- each stage of deformation acts independent of the previous stage

it is possible to identify the maximum strain as the sum of the imposed deformations in the individual deformation processes:

$$\varepsilon_{max} = \sum_i \ \varepsilon_i \quad (2.16)$$

Applying the principle of independence of deformation is possible to calculate the residual strain at break after spinning and eventual drawing:

$$e_b(\%) = \left(\frac{DR_{max}}{DR_m \cdot DR_{spun}} - 1\right) \cdot 100 = \left(\frac{\exp(\varepsilon_{max})}{DR_m \cdot \exp(\varepsilon_{spun})} - 1\right) \cdot 100 \quad (2.17)$$

where DR_m is the total draw ratio imposed to the fiber from the equipment during drawing, DR_{spun} and ε_{spun} are respectively the draw ratio and the deformation really imposed during the process of fiber formation.

If the N stages of drawing will be consider, the draw ratio DR_m can be determined by the following relationship:

$$DR_m = DR_1 \cdot DR_2 \cdot \ldots \cdot DR_N \quad (2.18)$$

In Figure 2.18 schematically the principle of independence of the processes of drawing applied to a fiber is shown: the higher the draw imposed in the fiber out of

the extruder ε_{spun}, the more reduced the residual deformation that the fiber is capable of supports before reaching the break [61].

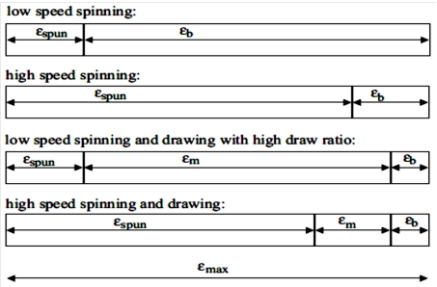

Figure 2.18 Schematic of the principle of independence of the deformations applied to a fiber.

Crystallinity

Increased molecular alignment has a positive effect on the degree of crystallinity and melting temperature, more pronounced in case of linear resin and high molecular weight samples. In the Figure 2.19 the effect of draw ratio on the melting temperature peak was depicted [73]. It can be noted that an improvement of melting temperature with draw ration, which is related to the increase in the crystallite *c* axis dimension. What is more, peak of melting temperature show a reduction of the width what indicates narrower distribution of crystallite thickness. Similar tendency can be observed in case of degree of crystallinity, increasing with orientation and leveling off at higher degrees of alignment [65].

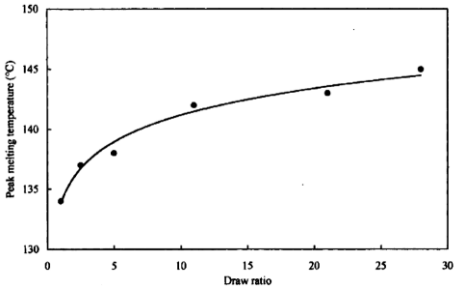

Figure 2.19. Melting temperature peak as a function of draw ratio of linear polyethylene drawn at 100°C [73].

Chapter III

Experimental

3.1. Materials

3.1.1. High Density Polyethylene – HDPE

High density polyethylene (HDPE) is the most widely used commercially available thermoplastics. The linear nature of this polymer permits the development of high degrees of crystallinity, which provide it with the highest stiffness and lowest permeability of all the types of polyethylene. This combination of properties together with low cost of production makes it suitable for many applications such as food container and bottles, pails, chemical storage tanks, pipe for water, sewer, and natural gas transportation [65]. Moreover, good tensile strength makes it proper for short-term load-bearing film application as for example grocery sacks.

High density polyethylene is composed of covalently linked carbon atoms backbone with pendant hydrogens and it consists primarily of unbranched molecules with very few flaws to mar its linearity. Because of low level of defects high degree of crystallinity can be achieved and density in the range of approximately 0.94-0.97g/cm^3 [65].

The organic matrix used in this work was Eltex® A4009MFN1325, a high density polyethylene (density 0.96 g/cm^3; melt flow index 0.85 dg/min at 190 °C, 2.16 kg) kindly supplied by BP Solvay (Brussels, Belgium) in the form of fine powder. From a chemical point of view Eltex® A4009MFN1325 is a homopolymer with a narrow molecular weight distribution primarily intended for the extrusion of monofilaments. It is recommended for the production a high tenacity tapes, cereal liners film and injection moulding. The main benefits is high tenacity of produced monofilament and tapes, very low gel content, superior processability and surface quality and very low moisture vapor transmission rate (MVTR). Table 3.1 summarized the main features of this material.

Properties	Test Method	Values
MFI (190°C, 2.16kg) [g/min]	ISO 1133	0.90
Density [g/cm³]	ISO 1183/A	0.96
Melting Point [°C]	ISO 11357-3	136

Table 3.1. Technical datasheet of INEOS Polyolefins Eltex® A4009MFN1325.

3.1.2. Polypropylene – PP

The significant growth of polypropylene (PP) use is attributed to a combination of many factors beside a good balance in physical and chemical properties. Because of appropriate melt rheology and thermal behaviour, PP-based materials are widely process by different equipment from injection moulding, calendaring till air quenched blow films [74]. Additionally, low density, excellent thermal stability, chemical inertness together with wide design flexibility and simplicity of recycling make is attractive material of construction.

Polypropylene homopolymer consists of molecular chains with repeating units of polypropylene monomer. It is characterized by high rigidity, heat resistance and melting point (~157°C) but is plagued by poor impact resistance at low temperature (<0°C) and relatively poor transparency [74].

Polypropylene Moplen HP500H (density 0.9 g/cm³; melt flow index 1.8 dg/min at 190 °C, 2.16 kg) kindly supplied by Basell Polyolefins (Ferrara, Italy) in the form of pellets was used as a organic matrix. It is a homopolymer for extrusion and injection moulding. Moplen HP500H exhibit good stiffness/impact balance. The main applications of this product are thermoformed containers, strapping, raffia and housewares applications. Table 3.2 summarized the main features of this material.

Properties	Test Method	Values
MFI (190°C, 2.16kg) [g/min]	ISO 1133	1.8
Density [g/cm³]	ISO 1183	0.9
Vicat Softening Point [°C]	ISO 306	76
Tensile stress at yield [MPa]	ISO 527-1	33
Tensile strain at break [MPa]	ISO 527-1	>50
Tensile Modulus [MPa]	ISO 527-1	1450

Table 3.2. Technical datasheet of Basell Polyolefins Moplen HP500H.

3.1.3. Layered Double Hydrotalcite – LDH

Perkalite is commercially available since April 2008 organically modified synthetic clay based on layered double hydroxides (LDH), also referred as hydrotalcite. Upon compounding in polymers, Perkalite can be delaminated to nanoscale level, resulting in improved polymer properties such as: thermo-mechanical, flame retardant, barrier and rheological. It also works as char promoting agent. The addition of LHD leads to a kind of in tumescent behavior, resulting a thicker char layer at the component surface. Thus the thicker char layer provides a better barrier of heat radiation and evaporation of volatile component reduction burning behavior. Moreover, together with flame retardants reduction the better mechanical and processing properties are obtained. The main features of the hydrotalcite used in this work are high temperature stability (>250°C), possible to be compounded in conventional method, good compatibility with apolar polymers and rubbers and it can be used for contact with foodstuffs [75, 76].

Synthetic hydrotalcite organically modified with fatty acid, Perkalite F100 from Akzo-Nobel (CAS number 39366-43-3 and 67701-03-5; density 1.35-1.40 g/cm^3) was provided from Clariant Masterbatches S.p.A.-Italy in the form of masterbatch pellets at 12% by wt. of LDH containing 12% by wt. of maleate polyethylene as compatibilizer HDPE-g-MA. Before processing, masterbatch was dried in a vacuum oven for 24h at 90 °C.

Property	Perkalite F100
Bulk density [kg/m^3]	200-300
Primary particle diameter [nm]	<20
Tapped density [g/l] DIN EN ISO 787	1.35-1.40
Moisture content [% wt.] [2h, 105°C]	<7%
Modifier content on LD	50%

Table 3.3. Technical datasheet of Clariant Perkalite F100.

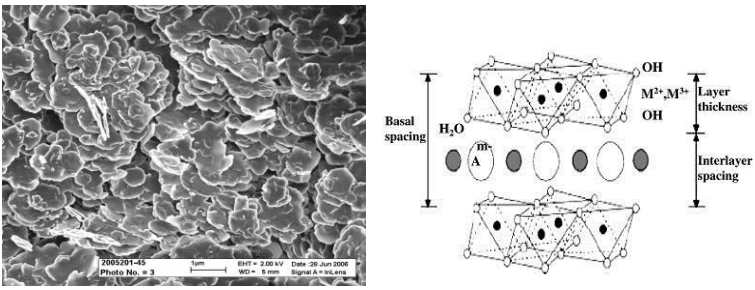

Figure 3.1. TEM image and schematic structure of Perkalite F100.

3.1.4. Fumed Silica Nanoparticles - FS

Aerosil is highly dispersed, amorphous, very pure silica that is produced by high-temperature hydrolysis of silicon tetrachloride in an oxyhydrogen gas flame [53]. Aerosil® hydrophobic products are characterized, among other things, by a low moisture adsorption, excellent dispersibility, and their ability to adjust rheological behaviour, even that of polar systems. They have plenty of applications. They can be found, for instance, in the cosmetics industry, where it increases the temperature stability of lipsticks. It is also used in the production of offshore yachts and in the electronics industry. At the same time, AEROSIL® is used in silicone sealants which can be found in any bathtub as well as in car paints. By the addition of these nanoparticles an excellent reinforcing properties in silicone rubber at high filler loading can be obtained [77].

Aerosil®805 is mostly used in paints and coatings systems, as adhesives and sealants improving effective rheology control in complex liquid systems and can be applied in coatings systems as an anti-settling agent, for the stabilization of pigments and to enhance the effect of corrosion protection.

Aerosil®AR974 found an application in adhesives, silicon sealants, coatings polymers, cosmetics. It improves shelf-life of silicone sealants, hydrophobicity and rheology of offset printing inks, water resistant, in coatings as

anti-settling agent, due to large surface area improved thickening and thixotropic effect as well as transparency.

Fumed silica nanoparticles Aerosil®R974 and Aerosil®805 were kindly supplied by Evonik (Essen, Germany). Both type of nanosilica are hydrophobic and are different for surface area and for the surface treatment. Aerosil®AR974 has a surface treated with dimethyldichlorosilane and specific surface area $170 m^2 \cdot g^{-1}$, while Aerosil®AR805 is treated with octylsilane and has specific surface area equal $150 m^2 \cdot g^{-1}$. The main features of the fumed silica used in this work are summarized in Table 3.4 and in Figure 3.2 are reported the scheme of the fumed nanosilica surface modifier.

Property	Aerosil®AR805	Aerosil®AR974
BET surface area [m^2/g]	150±25	170±20
Density [g/cm^3]	1.84	1.99
Primary particle diameter [nm]	12	12
Tapped density [g/l] DIN EN ISO 787	60	50
Moisture content [% wt.] [2h, 105°C]	≤0.5	≤0.5
SiO_2 content [% wt.]	≥99.8	≥99.8

Table 3.4. Technical datasheet of Evonik Aerosil® fumed silica nanoparticles.

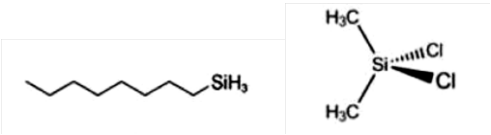

a) b)

Figure 3.2. Organic surface modifier respectively (a) for Aerosil®805 - octylsilane and b) Aerosil®AR974 - dimethyldichlorosilane.

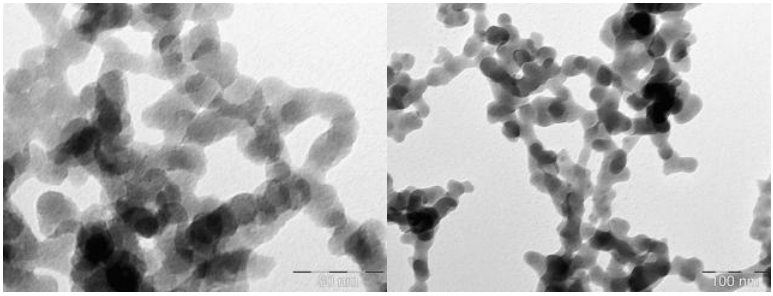

Figure 3.3. TEM image of Aerosil®AR974 fumed silica nanoparticles.

3.2. Composite Preparation

For the preliminary tests materials were melt compounded followed by a hot pressing in order to perform plates for the thermo-mechanical characterization. Polyethylene or polypropylene (depends on the nanocomposites) were utilized as received, while the fillers were dried in a vacuum oven for 24h at 90 °C. The polymer matrix and the selected amount of clay were physically mixed at room temperature Each mixture was then melt compounded in co-rotating Thermo-Haake Polylab Rheomix internal mixer (Fig.3.4.a and b) at 155 °C; rotor speed 60 rpm and residence time of 10 minutes. Subsequently square sheets of 160 mm wide and 1.5 mm thick were obtained by compression moulding in a Carver Laboratory press (Fig. 3.4.c) at 155°C in 10 minutes; consolidation pressure of 0.2MPa. The molten plates were then water cooled at 20°C min^{-1}. The internal mixer and the hot plate press are represented in Figure 3.4.

a)

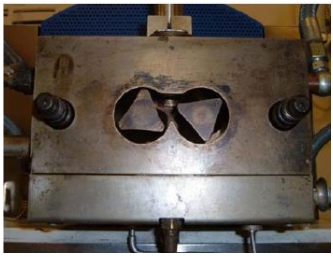

b)

c)

Figure 3.4. Photographs of (a) Haake® internal mixer (b) view inside and (c) Carver® hot press.

Nanofilled polymer fibers were produced after direct mixing and compounding of selected formulation by using a Thermo Haake PTW16 intermeshing co-rotating twin screw extruder (screw diameter=16 mm; L/D ratio=25; rod die diameter 1.65 mm) presented in Figure 3.5 and 3.6. The screws rotation speed was regulated depending on the melt flow of material in order to maintain residence time of 20 min and to produce nanofilled polyolefines fibers with diameter of about 500 μm. The temperature profile was gradually increased from hopper to rod die T_1 = 130 °C, T_2 = 200 °C, T_3 = 210 °C, T_4 = 220 °C, T_5 = 220 °C for HDPE and T_5 = 230 °C for PP

with an output of 140 g/h. The spun fibers were rapidly cooled in water and wound around a collecting roll/drum at room temperature (Figure 3.7, Table 3.6).

a) b)

Figure 3.5. Photographs of (a) twin screw extruder Thermo Haake PTW16, (b) head of the extruder.

Figure 3.6. Photographs of (a) twin screw extruder Thermo Haake PTW16 view inside.

Twin screw extruder Thermo Haake PTW16		
Parameter	**Value for HDPE**	**Values for PP**
T_1	130 °C	130 °C
T_2	200 °C	200 °C
T_3	210 °C	210 °C
T_4	220 °C	220 °C
T_5	220 °C	230 °C
Screw diameter	16 mm	16 mm
Rod die diameter	1.65 mm	1.65 mm

Table 3.5. Working parameters of twin screw extruder Thermo Haake PTW16.

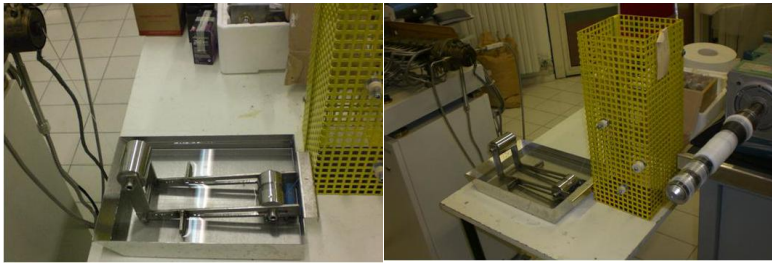

Figure 3.7. The collecting process of as-spun material.

Collecting process	
Parameter	**Value for HDPE and PP**
Temperature of cooling water	~15 °C
Diameter of the collecting roll	40 mm
Velocity of the collecting roll	67 rpm
Diameter of the collected fiber	~0.5 mm

Table 3.6. Working parameters of the collecting process of the fibers.

Figure 3.8. The hot-plate drawing apparatus SSM-Giudici srl, Galbiate-LC, Italy.

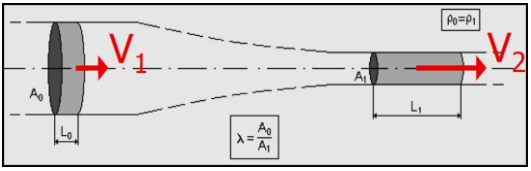

Figure 3.9. Scheme of drawing process.

Drawing Process		
Parameter	Value for HDPE	Value for PP
Temperature of drawing	125 °C	145°C
Velocity of roll release roll	10 rpm	10 rpm
Velocity of collecting roll	variable	variable

Table 3.7. Working parameters of hot-plate drawing apparatus.

Fibers were drawn at 125°C in case of HDPE and at 145°C for PP by using a modified hot-plate drawing apparatus (SSM-Giudici srl, Galbiate-LC, Italy). Maintaining as a constant velocity of release roll and increasing the velocity of collecting roll it was possible to obtain fibers with different draw ratio used for thermo-mechanical characterization. In Figure 3.7. the collecting process of as-spun material and in Figure 3.8. the hot plate drawing apparatus were depicted and the process parameters were summarized in Table 3.6. and 3.7. The draw ratio is defined as the ratio between the velocity at break (V_2) and initial velocity (V_1), the section of the undrawn (A_u) and drawn fibers (A_d), and initial (D_i) and final (D_f) diameter according to eq. 3.1

$$DR = \frac{V_2}{V_1} = \frac{A_u}{A_d} = \left(\frac{D_i}{D_f}\right)^2 \quad (3.1)$$

3.3. Experimental activities

3.3.1. Microstructural characterization

3.3.1.1. Density measurements

Density measurements were performed by using a Micrometrics Accupyc 1330 helium pycnometer at 23.0°C. A testing chamber of 3.5 cm^3 was used, and 30 measurements were replicated for each specimen. Standard deviation on each measurement was ±0.001g/cm^3.

3.3.1.2. Melt Flow Index (MFI)

Melt Flow Index measurements were performed by a Dynisco LMI 400 plastometer according to ASTM D1238-10. About 3 grams of material were preheated at 190ºC for PE and 230°C for PP for 5 min following procedure A and then extruded with an applied load of 2.16 kg.

3.3.1.3. Microscopy techniques

Environmental Scanning Electron Microscopy (ESEM) and Transmission Electron Microscopy (TEM) techniques were used in order to evaluate the dimension and distribution of the fillers inside the polymer matrix.

Scanning electron micrographs (SEM) were obtained by using a Philips XL30 Environmental Scanning Electron Microscopy, at an acceleration voltage between 20 and 25 kV. Samples were immersed in liquid nitrogen and fractured.

TEM analysis has been performed on the ultramicrotomed cross section of as-spun and drawn nanocomposite fibers in order to get information about nanofiller distribution and their orientation when a strain was applied. The observations were performed by using FEI Tecnai 10 transition electron microscope (TEM), operated at cryogenic temperature (lower than -70°C).

3.3.1.4. X-Ray Diffraction (XRD) annalysis

In order to evaluate the influence of the nanofiller on the crystalline structure of the material, X-Ray diffraction analysis were conducted on nanocomposites plates and fibers. X-rays diffraction (XRD) were collected by using a Rigaku III D-Max diffractometer, in a θ-2θ Bragg-Brentano geometry with a graphite monochromator in the diffracted beam (monochromatic radiation CuKα line with λ = 1.54056 Å). Fibers were fitted on aluminum sample holder (approximate 0.5 cm x 2 cm) orthogonal to the incident beam, and the following parameters: scan range: 1.8 – 40°; sampling interval: 0.05°; counting time: 5 s.

3.3.1.5. Thermo Gravimetrical Analysis (TGA)

Thermal degradation was studied in the range 50-600 °C by using thermobalance Mettler TG 50 on sample of about 15 mg at a heating rate of 10 °C/min with an air flow of 100 ml/min. The results represent the average of three tests.

3.3.1.6. Differential Scanning Calorymetry (DSC)

Different Scanning Calorymetry (DSC) was utilized in order to detect the influence of the fillers on the melting and crystallization behavior of the nanocomposites.
Differential scanning calorimetry (DSC) analysis was performed on samples of about 15 mg in 160 μl aluminum crucibles by using a Mettler DSC30 calorimeter, in the range 0-200 °C for HDPE and 0-250°C for PP with a heating-cooling-heating cycle at ±10 °C/min flushing nitrogen at 100 ml/min. The crystallinity percentage of the matrix was calculated according to Equation (3.2)

$$X_{matrix} = 100\frac{\Delta H_i}{\Delta H_{matrix}\times(1-f)} \qquad (3.2)$$

where ΔH_i is the melting enthalpy, ΔH_{matrix} is the reference enthalpy of a full crystalline matrix in our case polyethylene or polypropylene depends on the composition, taken as 293 J·g^{-1} or 207J g^{-1} for PP [78], and *f* is the weight fraction of nanofiller.

3.3.1.7. Vicat Softenning Point (VSP)

Vicat softening temperature (VST) was measured by a HDT-VICAT instrument from ATS-Faar S.p.A (Milano-Italy) following ASTM D1525-09. Three specimens of 3 mm thickness were used in each test (heating rate of 50°C/h; applied load of 10 N).

3.3.1.8. Shore Hardness test

Shore D hardness was evaluated according to ASTM D2240-05 at 25 °C on 3mm thick rectangular specimen by using an ATS-Faar S.p.A (Milano-Italy) durometer as average of 5 measurements in different positions under an indentation time of 5 sec.

3.3.2. Viscoelastic behaviour

3.3.2.1. Dynamical Mechanical Thermal Analysis

Dynamic mechanical thermal analyses were performed in order to evaluate the tensile behavior of the prepared nanocomposites at different temperatures.
The tests were performed with a DMA Q800 testing machine (TA Instruments). The experiments were carried out in tensile mode by using single cantilever clamp on samples by applying a sinusoidal strain with a frequency of 1 Hz and amplitude of 64. In order to prevent buckling of the fibers a pre-stress of 0.01 N was applied. A heating rate of 3 °C/min, from -130 to 145 °C, was selected for all tests.
For the plates 12 x 5 x 1.0 mm samples and for the fibers cylindrical specimens with a gauge length of 10 mm and different diameter (0.50 - 0.10 mm diameter) were selected.
Moreover, in order to evaluate the viscoelastic behavior of the material as a function of the frequency for selected draw ratio multi-frequency test were conducted at 0.3, 1, 3, 5 and 10Hz, in a temperature range from -40 to 60°C at heating rate 0.5°C/min. According to the frequency-temperature superposition principle [79], storage modulus master curves at the reference temperature of 30 °C were generated.

3.3.2.2. Creep test

Creep test were performed in order to evaluate the deformation behavior of the material under a constant load. The tests were performed at room temperature by using a dynamic mechanical analyzer DMA Q800 (TA Instruments®). Both unfilled and selected nanocomposites were tested at a constant stress (σ_0) of 3 MPa for 3600 s. The chosen creep stress corresponds to about 10% of the stress at yield. Cylindrical samples 15 mm long and 0.50-0.10 mm thick were used, adopting a gage length of 10 mm. In this way the creep compliance D(t), determined as a ratio between the deformation and the applied constant stress, was obtained.

3.3.3. Fracture behaviour

3.3.3.1. Quasi-static tensile test

In order to evaluate the role of the nanofiller on the tensile properties as stress at yield (σ_y), stress at break (σ_b) and strain at break (ε_b) quasi-static tensile test were performed. Mechanical properties of plates and fibers were performed at room temperature by using a dynamometer Instron 4502, equipped with a load cell of 1 kN and 100 N respectively. Rectangular specimens (80 mm long, 5 mm wide and 1,5 mm thick) and fiber specimens (diameter from 500 up to 100 micron; gauge length 30 mm) were tested at a cross-head speed of 50 mm min^{-1}. According to ISO 527 standard, the elastic modulus was determined as secant value between deformation levels of 0.05% and 0.25%. The results represent the average of at least three specimens

RESULTS AND DISCUSSION

Chapter IV

Part of this chapter has been published in:

Izabela Dabrowska, Luca Fambri, Alessandro Pegoretti, Giuseppe Ferrara
Organically modified hydrotalcite for compounding and spinning of polyethylene nanocomposites.
eXPRESS Polymer Letter, No. 7 (2013) 936-949.

Luca Fambri, Izabela Dabrowska, Alessandro Pegoretti, Ricardo Ceccato
Melt spinning and drawing of polyethylene nanocomposite fibers with organically modified hydrotalcite.
Journal of Applied Polymer Science, in press.

4.1. HDPE-LDH nanocomposite plates and fibres

4.1.1. Compounding and morphology

As reported in Table 4.1. the investigated formulations are a combination of polyethylene with the nanofiller LDH and the compatibilizer. It should be noted the higher MFI of the masterbatch, and consequently the MFI values increased with the percentage of hydrotalcite in the polymer matrix, with an almost linear dependence on the HDPE-LDH composition (Table 4.1.). On the other hand, an unexpected deviation and lower melt flow of LDH-HDPE fiber, and in particular composition at 0.5 and 1% of LDH exhibited the higher difference with respect to the plate of analogous

composition. The effect could be attributed to the better dispersion of LDH in the twin-screw compounding and extrusion for composition up to 3% of LDH.

Sample designation	HDPE [%]	Compatibilizer HDPE-g-MA [%]	LDH [%]	MFI plates [dg/min]	MFI fibers [dg/min]	Shore D [Hs]	VST [°C]
HDPE	100	0	0	0.90±0.03	0.52±0.05	62.2±0.6	136.6±0.3
Masterbach	76	12	12	1.59±0.02	-	62.0±0.5	127.8±1.5
LDH-0.5	99.5	0.5	0.5	0.91±0.03	0.54±0.02	62.5±0.5	135.9±0.4
LDH-1	99	1	1	1.03±0.02	0.82±0.01	64.5±0.6	135.8±0.6
LDH-2	98	2	2	1.12±0.02	1.0±0.001	64.3±0.6	135.4±0.5
LDH-3	97	3	3	-	1.12±0.01	-	-
LDH-5	95	5	5	1.26±0.03	-	63.5±0.4	134.0±0.4

Table 4.1. Designation and formulation of HDPE nanocomposites (in percentage by wt.). Dependence of melt flow (230°C, 2.16 Kg), hardness Shore D and Vicat Softening Temperature (VST) on the composition.

The effect of compounding and the quality of hydrotalcite dispersion into HDPE matrix was evaluated from ESEM analysis of cryo-fractured surfaces of HDPE-LDH nanocomposites. Figure 4.1a evidences the presence of various agglomerates with dimension in the range between 5 and 15 microns in the masterbatch containing 12% wt. of hydrotalcite. These agglomerates need to be properly disaggregated and dispersed in HDPE compounds during processing otherwise these defects and stress concentration points could prevent the drawability in fiber spinning [80]. ESEM analysis evidenced the progressive dispersion of LDH in polyethylene matrix. An almost satisfactory result was obtained in compounding through internal mixer for various compositions, as evidenced from the particle dimension at the fracture surface in comparison with that of the masterbatch (Figure 4.1a). For instance LDH particles of 0.25-0.40 microns and other aggregates of about 0.8 micron were observed in plates at 5% of LDH (Figure 4.1c). The dimension of both aggregates and particles were found to reduce with the masterbatch content. Figure 4.1d shows the fracture surface of LDH-1 plate, for which particles of about 0.20-0.35 micron and aggregates up to 0.6 micron were evidenced.

SEM micrographs of the fracture surface of the fibers are reported in Fig. 4.1 d-i. In the case of LDH fiber, some lower size particles were revealed, indicating that twin-screw processing allowed a submicron level of dispersion especially at low

hydrotalcite content, as in the case of LDH 0.5 fiber, for which particles 0.15-0.24 micron were shown in Figure 4.1d. It could be seen that for LDH-1 (Fig.4.1e and f) and LDH-2 (Fig. 4.1.g and h) the dispersion of hydrotalcite was uniform. Mainly LDH particles clusters of about 0.25 μm are visible, however, single larger clusters in the range of 1.2-1.5μm are also observed. At a higher magnification, the particles of nanofiller seem to be slightly aligned, probably in relation to the orientation during the melt-spinning process. Similar planar shape of LDH particles was already observed in the case of PP-LDH fibers [81]. On the other hand, the fracture surfaces of undrawn LDH-3 fiber reveal many clusters of aggregates hydrotalcite particles with a mean size around 1,5-2 μm (Fig. 2i). It is known that for a low organoclay content a good dispersion of small size particles can be achieved, frequently at nanoscale level, whereas higher loadings result in large size domains and less uniform distribution. Similar behavior was already observed by D'Amato et al. in the case of the HDPE-nanosilica composite fibers [82].

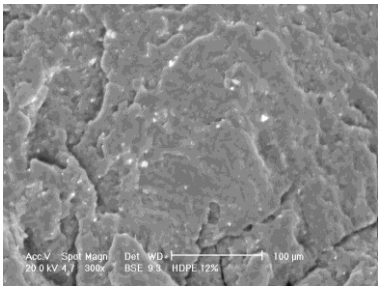

Fig. 4.1.a ESEM micrograph of masterbatch.

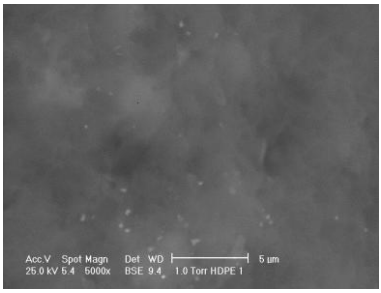

Fig.4.1.b ESEM micrograph of LDH-1 plate.

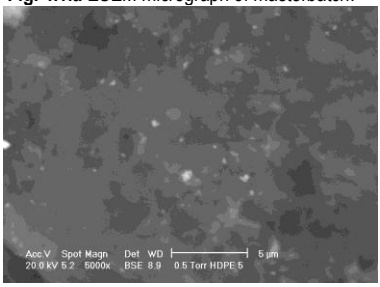

Fig. 4.1.c ESEM micrograph of LDH-5 plate.

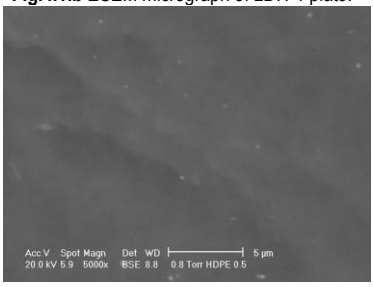

Fig. 4.1.d ESEM micrograph of LDH-0.5 fiber.

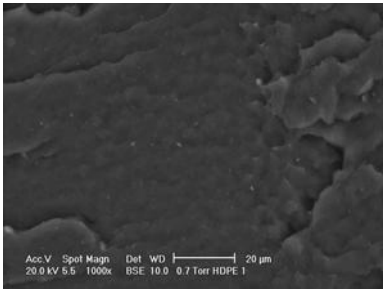

Fig. 4.1.e ESEM micrograph of LDH-1 fiber.

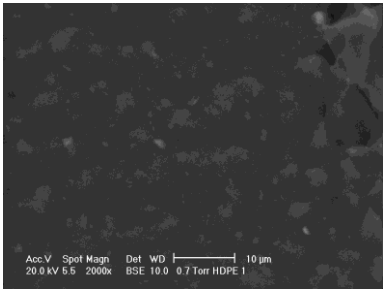

Fig. 4.1.f ESEM micrograph of LDH-1 fiber.

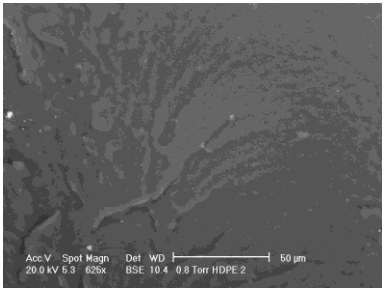

Fig. 4.1.g ESEM micrograph of LDH-2 fiber.

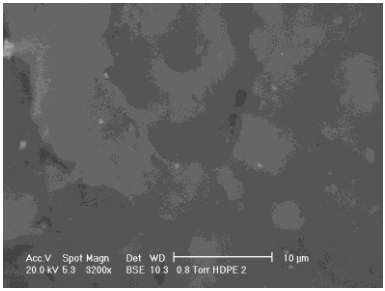

Fig. 4.1.h ESEM micrograph of LDH-2 fiber.

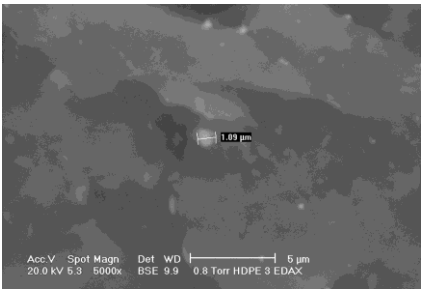

Fig. 4.1.i ESEM micrograph of LDH-3 fiber.

The XRD analysis is a very useful method to describe the extent of intercalation and exfoliation of the nanofiller having layered structure. The XRD analysis for HDPE-LDH plates and fibers are reported in Figure 4.2.a and 4.2.b respectively. The XRD pattern was interpreted with respect to the position of the basal peak (003), which depends on the distance between two adjacent metal hydroxide sheets in the LDH crystal lattice. The higher order peaks indicate the presence of repeating crystal

planes and symmetry in a specific crystallographic direction [48]. A more intense and sharp peak indicates a more ordered intercalated structure, while less intense and broader peak testify the existence of a disordered intercalated structure [83]. XRD spectrum of LDH-5 plate evidences the two characteristic Bragg reflections of LDH presence at about 4.9º (003) and 11.2º (006), in agreement to the ICPDS Powder Diffraction File (LDH number 41-1428). According to some authors [48] the third peak at 8.4º is attributed to LDH, while it is not included in the ICPDS standard for Al-Mg LDH; however it might be related to the phase derived from primary clay, like Dypingite, $Mg_5(CO_3)_4(OH)_2 \cdot 5H_2O$. For the compositions LDH-2 and LDH-1 with lower nanofiller content only the main peak at 11.2º is well detectable, whereas the two others appear weak and broad. Moreover, XRD spectrum of LDH-5 suggests the presence of another and very intensive reflection at about 1.9º (001), even if not completely visible in Figure 4.2.a, that could be attributed to the presence of bulk LDH nanoplatelets [84].

XRD spectra of HDPE-LDH fibers containing 1 and 2% of hydrotalcite reported in Figure 4.2.b show the characteristic reflections attributed to LDH particles, the very weak peaks and the shift to lower 2θ (4.4º, 8.1º and 11º). It is known that a complete degree of exfoliation of layered crystalline fillers in polymer matrix determines the disappearance of corresponding peaks in the XRD spectra of the composites. However, the absence of the peak could be also related to the very low concentration of the filler [49]. Some of these results might suggest a possible intercalation with partial exfoliation, as reported by other researchers [48, 84-87]. Moreover, after comparison of Figures 4.2.a and 4.2.b, the lower intense reflections of fibers with respect to those of plates, at the same (1 and 2% by wt.) nanofiller content, could suggest that the layer of LDH were better intercalated and partially exfoliated in the polymer during melt compounding/spinning in twin-screw extrusion.

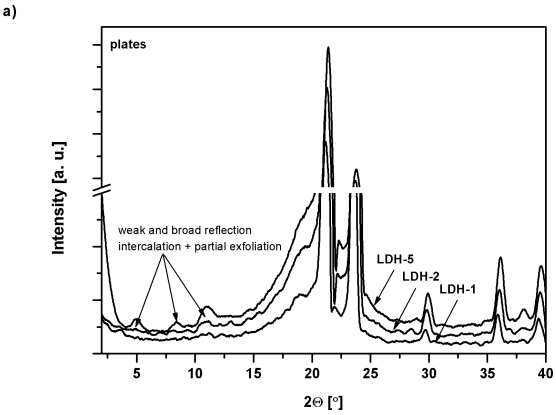

Figure 4.2.a. XRD patterns of HDPE-LDH nanocomposites plates with different nanofiller content

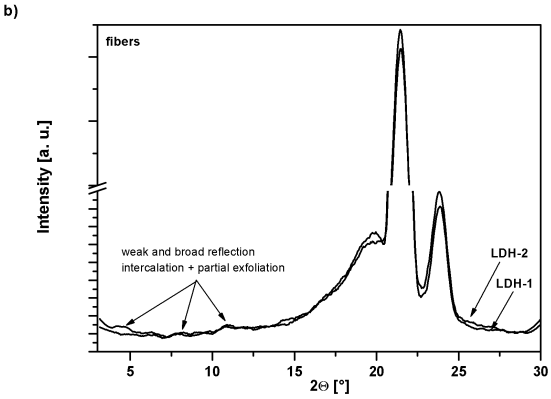

Figure 4.2.b. XRD patterns of HDPE-LDH nanocomposites fibers with different nanofiller content.

Figure 4.3 shows the infrared spectrum of LDH-5 compound in comparison with neat HDPE and HDPE masterbatch containing 12% wt. of organically modified LDH, evidencing the peaks of carbonated hydrotalcite, as reported in the literature [88]. The most intensive peaks at 790 and 680 cm^{-1}, attributed to the metal hydroxide deformation; the region between 1200 and 1800 cm^{-1} is characterized by the bending mode of interlayer water around 1560 cm^{-1} and two modes at 1370 and 1400 cm^{-1}

associated with the interlayer carbonate, whereas the two bands around 1100-1055 cm^{-1} can be assigned to deformation modes of hydroxyl group [89]. In the same time, peak at about 1740 cm^{-1} is related to the C=O stretching of maleate coupling agent in the masterbatch.

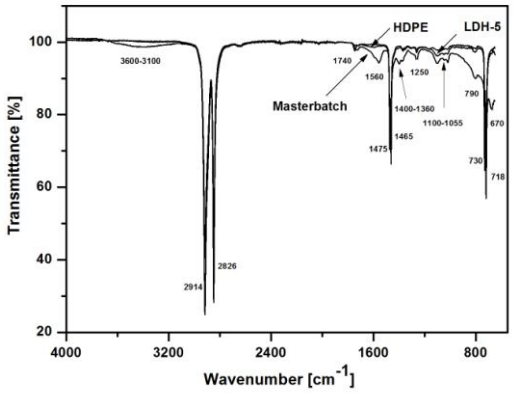

Figure 4.3. FTIR spectra of neat HDPE and HDPE composites, i.e. LDH-5 and masterbatch containing 12%wt of hydrotalcite.

4.1.2. Compression molded plates (Shore D, Vicat and DMTA).

Shore hardness (Hs) and Vicat softening temperature (VST) are interesting data for the initial comparison of nanocomposite compression molded plates, being related to the tip penetration at room temperature and during heating, respectively. Higher Shore D values of polymer nanocomposites (about 63-64 Hs) with respect to 62.2 Hs for polyethylene evidence the effect of nanofiller, as reported in Table 4.1. The highest hardness value was obtained for LDH-1 (64.5 Hs), while at higher LDH content the reinforcement action is progressively counterbalanced by the presence of various agglomerates (lower interfacial interaction), reaching for LDH-5 value equal to 63.5 Hs.

Vicat Softening Temperature (VST) gives a useful indication of the relative rigidity at high temperature (Table 4.1.). VST value progressively decreased with the

percentage of hydrotalcite in the polymer matrix, in particular from 136.6°C, for neat HDPE, to about 135-136°C LDH content in the range 0.5- 2%, and to 134.0°C for LDH-5 respectively.

The results of dynamic mechanical analysis of neat HDPE and nanofilled HDPE plates are reported in Figures 4.4. Storage modulus increased with percentage of the organically modified LDH, particularly at lower temperatures, i.e. from -120ºC to -20ºC, and the highest values were obtained for LDH-5 and LDH-1, as shown in Figure 4.4. These results could be tentatively attributed to the combined effects of both the filler content and the polymer microstructure (note that hardness values present a maximum for LDH-1). On the other hand at higher temperature above 0ºC, both neat HDPE and HDPE-LDH nanocomposites exhibited a similar storage modulus, with some minor differences. In the range 0-50ºC the highest storage modulus was found for LDH-1. A similar behavior in the case of LDPE/silica composite was explained from Kontou and Niaounakis by considering the coexistence in the matrix of composite two parts, i.e. the bulk free part and the interphase formed by the physical/chemical interaction of polyethylene molecules and/or crystallization on the filler's surface [90]. Loss modulus evidences in Figure 4.4. the three main relaxations of polyethylene α, β and γ at about 50°C, -40°C and -120°C respectively, according to literature [91, 92]. The β relaxation, related to the movement of the chain units in the interfacial region [91, 93], typically dependent on branching, is practically absent in the case of neat HDPE, as previously shown for HDPE with melt flow 1.15 dg/min [94] After addition of 0.5 % LDH, the β-peak appears in the zone -50 and 0°C, and it becomes more intense for higher percentage of hydrotalcite [95], as a combined effect of the higher amount of fatty acid, the organo-modifier agent, and the higher interfacial region due to the higher percentage of nanofiller. The position of loss modulus α-peak moved to lower temperature after addition of hydrotalcite masterbatch, i.e. from 59ºC of the neat HDPE to 52ºC in the case of LDH-5. Moreover, the intensity of the α–peak in loss modulus curves of LDH-composites is higher than that of neat HDPE, in direct dependence on the crystallinity of the polymer matrix.

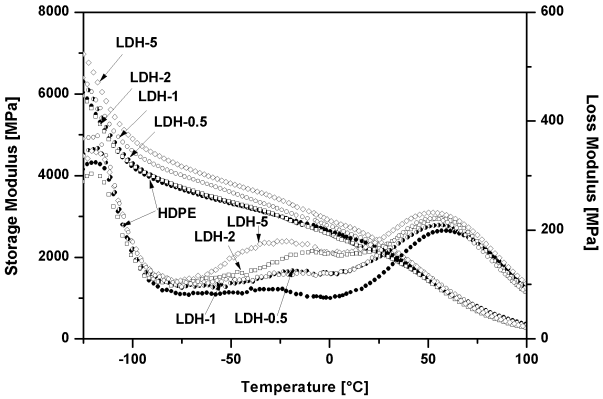

Figure 4.4. Storage modulus and loss modulus of neat HDPE plates (●) and nanocomposites HDPE plates containing 0.5% (◑), 1% (○), 2% (□) and 5% (◊) of LDH, respectively.

4.1.3. Thermal properties of plates and fibres

Following the initial characterization of HDPE-LDH plates up to 5% of hydrotalcite, various compositions with a maximum 3% of LDH were also compounded and extruded for fiber production. In particular, this paragraph will describe and compare thermogravimetry results, density and calorimetric data of both plates and fibers with LDH.

Representative TGA curves of plates and fibers are reported in Figure 4.5.a and b, evidencing the beneficial effect of organically modified hydrotalcite on the thermal degradation resistance not only for the masterbatch, but also for all the nanocomposites at 0.5-5% LDH, with respect to the neat HDPE. Similar results were observed in the case of fibers, where the curves of nanofilled HDPE appeared shifted at higher temperature (Fig. 4.5.b).

The comparison of thermal stability was carried out in terms of selected decomposition temperatures, in particular the initial degradation at 10% ($T_{0.1}$), and the temperatures $T_{0.5}$ and $T_{0.8}$ at which occurred 50% and 80% of mass loss, respectively. The decomposition temperatures ($T_{0.1}$, $T_{0.5}$, $T_{0.8}$) of HDPE-LDH plates

and fiber, summarized in Table 4.2. were found to be higher than those of neat HDPE, even at low hydrotalcite content with a stabilizing effect of nanofiller particles under oxidizing conditions. Following Gilman suggestion [27], this behavior is due to the hindered thermal motion of the polymer molecular chain. At the same time the selected decomposition temperatures tend to increase with LDH content. However some discrepancies from linearity could be attributed to the parallel contribute of the nanofiller dispersion, particularly at higher mass loss. For instance in the case of fiber and plates containing 1% of LDH, it is worth noting that $T_{0.8}$ was found at higher temperature than that of masterbatch at 12% of LDH content, 460°C vs. 458°C, respectively. The slightly lower degradation temperature of HDPE nanocomposite fibers with respect to plates could be attributed to the higher surface of fiber in oxidizing atmosphere.

Residual mass at 600°C is directly dependent on the nanofiller content, ranging between 0.4% for composition LDH-0.5 up to about 1.8% for LDH-3 fiber and LDH-5 plate. HDPE masterbatch (12% wt of LDH content) plate exhibited a relevant mass loss of about 3% weight in the range 230-280°C, and a final residue of 4% at 600°C.

Hence, these LDH nanocomposites showed in TGA test a charring process with formation of a charred layer, which enhances the material thermal stability, in conformity to literature results [96, 97]. In fact, the incorporation of clay into a polyolefin matrix enhances its thermal stability by acting as a superior insulator and mass transport barrier to the volatile products generated during decomposition, making the diffusion path of the oxygen more tortuous, and thus retarding the thermo-oxidative process [98], [46, 99].

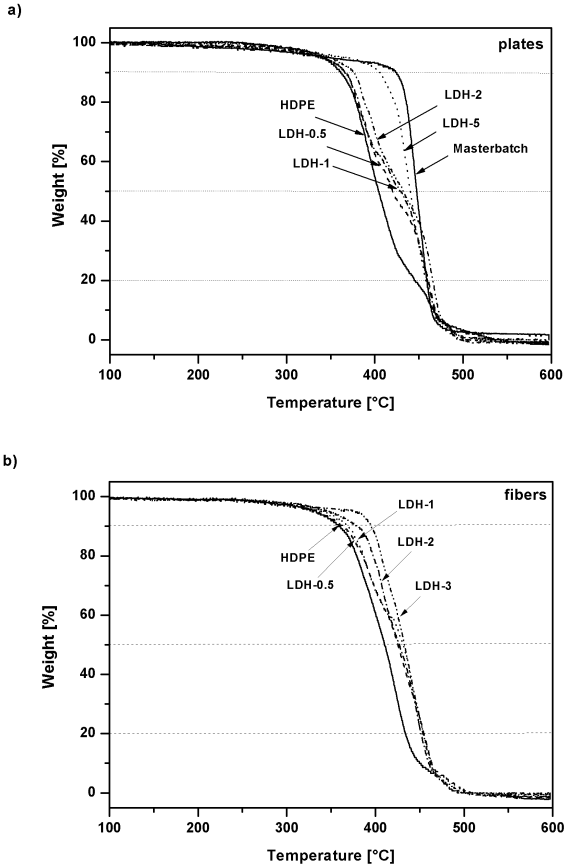

Figure 4.5. TGA thermograms of neat HDPE and HDPE nanocomposites (a) plates and (b) fibers with different LDH content (from 0.5% up to 12% by wt.)

Composition	Temperature of 10% Mass loss – $T_{0.1}$ [°C]		Temperature of 50% Mass loss – $T_{0.5}$ [°C]		Temperature of 80% Mass loss – $T_{0.8}$ [°C]		Residual mass at 600°C [%]	
	plates	fibers	plates	fibers	plates	fibers	plates	fibers
HDPE	356±2	358±2	403±1	412±3	444±6	444±0	0.0±0.2	0.0±.4
Masterbach	424	-	447	-	458	-	4.0	-
LDH-0.5	364±5	362±1	420±5	428±5	460±4	454±3	0.4±0.4	0.4±0.4
LDH-1	365±8	368±1	428±2	422±8	460±2	460±6	1.3±0.1	1.0±0.3
LDH-2	371±4	375±5	433±3	425±3	465±6	454±4	1.4±0.3	1.5±0.1
LDH-3	-	389±6	-	433±3	-	452±4	-	1.8±1.0
LDH-5	405±4	-	441±1	-	455±1	-	1.8±0.2	-

Table 4.2. Selected TGA results of neat HDPE and nanofilled HDPE plates and fibers.

Bulk properties of plates and fibers were compared in term of density, as shown in Table 4.3. The results evidenced a direct dependence not only on the composition, but also on the different processing. The higher the LDH content, the higher the density, in between the density 0.957 g/cm^3 of neat polyethylene and the density of the masterbatch, 0.985 g/cm^3. It should be noted that the density of fiber containing 1-3% of LDH is higher not only than HDPE fiber, but it is also higher than the correspondent LDH nanocomposite plates. This evidence reveals that density could be influenced from various other factors than LDH content, for instance from the orientation and from the crystallinity.

For such reason, an investigation of plates and fibers was performed through DSC analysis as shown in Figure 4.6 where the heating-cooling cycles of HDPE and selected LDH composites were compared. In Table 4.3, the relative crystallinity values of polyethylene matrix and the temperatures of melting and crystallization during the heating and the cooling were presented. The melting temperature and particularly the level of crystallinity of fiber samples were lower than the correspondent of plate samples, in this latter case about 50% vs 70%, confirming a peculiar dependence on the thermal history in the processing [46]. Fast cooling in fiber spinning (about -20°C/sec) caused not only a quenched crystallization process with the formation of less perfect crystal (and almost constant melting temperature of about 133°C), but also a lower crystallizability. On the other hand, the slow cooling applied for plates (about -20°C/min) determined a slow crystallization rate and hence the formation of more perfect crystals at higher melting temperature, from about 135°C (HDPE) up to 137°C (LDH nanocomposite).

Literature data reported various effects of nanofiller on crystallization temperature and crystallinity content of polyethylene matrix, showing negligible [100, 101], or significant [95, 102] or small differences [103], in dependence on both processing and composition. In our case, the crystallinity of nanofilled polymer was found almost the same in the case of compression molded plates, whereas the final crystallinity of fiber slightly increased with LDH content, in direct conformity to the density measurements.

From the DSC cooling stage, it is noticeable that crystallization temperature of nanocomposites plates and fibers is higher than neat HDPE, i.e. up to 115°C versus

110°C, suggesting a mild effect of LDH as nucleating agent. Moreover it should also be consider that the higher crystallization temperature of plates with respect to fibers could be attributed to the higher initial crystallinity of plates, particularly associated to the heterogeneous nucleation attributed to hydrotalcite [27, 85].

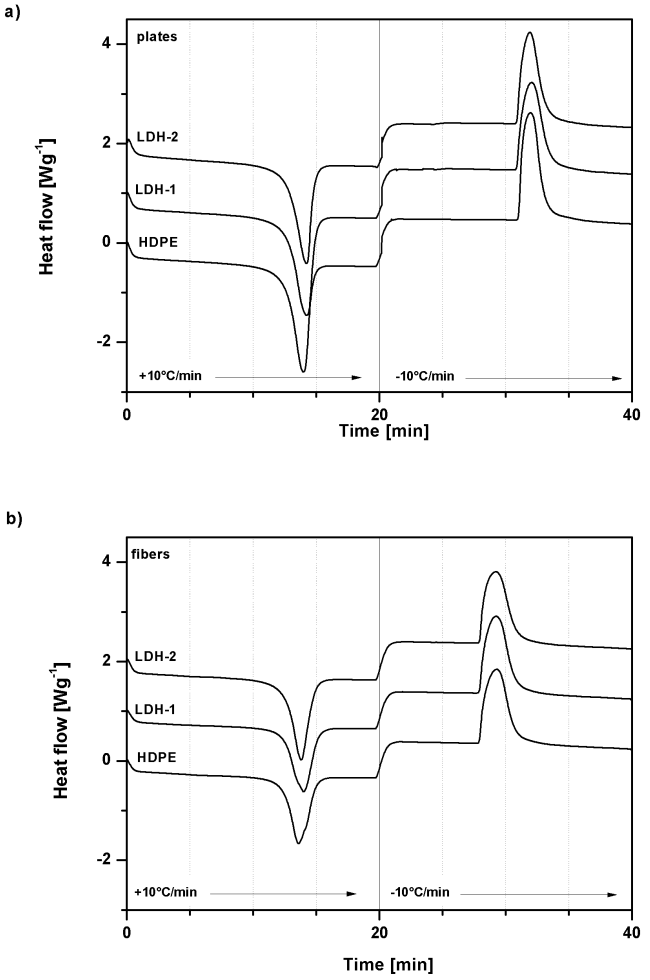

Figure 4.6. DSC thermograms (heating at +10°C/min and cooling at –10°C/min) of neat HDPE and nanocomposites plates (a) and fibers (b) with different nanofiller content.

Composition	Density [g/cm³]		Melting temperature Tm [°C]		Crystallinity Content X_c [%]		Crystallization temperature Tc [°C]	
	plates	fibers	plates	fibers	plates	fibers	plates	fibers
HDPE	0.957	0.954	134.6	133.4	70.8	50.5	110.0	110.8
Masterbach	0.985	-	136.9	-	62.5	-	109.4	-
LDH-0.5	0.958	0.945	136.7	133.0	70.0	51.7	113.5	111.8
LDH-1	0.963	0.960	137.4	133.4	71.8	53.0	114.0	112.5
LDH-2	0.964	0.976	137.5	132.0	71.0	54.5	115.3	112.8
LDH-3	-	0.982	-	133.0	-	53.3	-	115.0
LDH-5	0.971	-	135.0		70.4		115.3	-

Table 4.3. Density, melting, crystallization temperature and crystallinity content for neat HDPE and nanofilled HDPE plates and fibers.

4.1.4. Mechanical properties of plates and fibres

An enhancement of elastic modulus and tensile strength, and a reduction of tensile ductility compared to neat matrix could be expected after a good dispersion of nanofiller [85, 104, 105]. Therefore, mechanical tests were performed on both plates and fibers of various LDH content.

Representative stress-strain curves for plates and fibers are presented in Figures 4.7 whereas all the results are summarized in Table 4.4 and in Table 4.5 respectively. As first evidence, the formulation at 0.5% of organically modified LDH showed the highest ultimate properties of both stress at break and strain at break (about 1900%), either in the case of plates (Figure 4.7a) or in the case of fibers (Figure 4.7b). However at the same time, a slightly lower tensile modulus with respect to HDPE was obtained, 0.95GPa vs 0.96GPa after compression molding (plates), and 0.53 GPa vs 0.55 GPa after spinning (fibers).

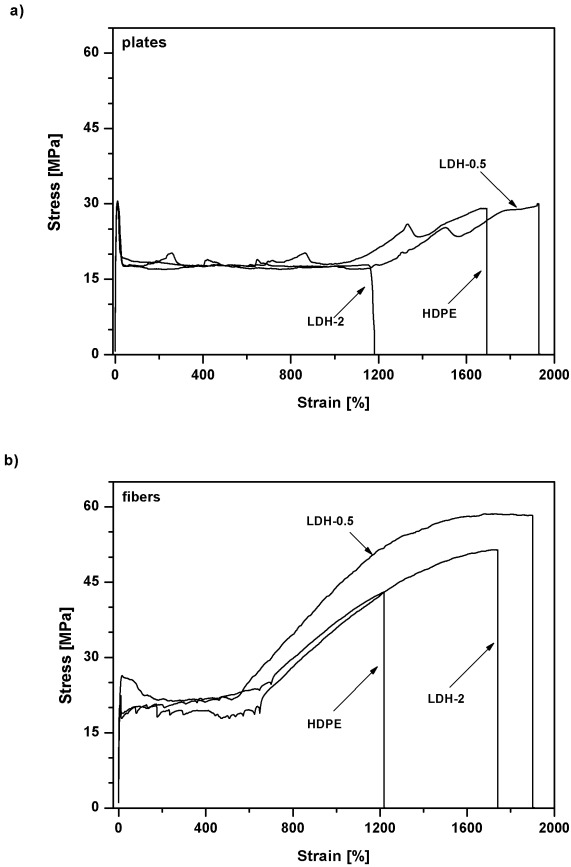

Figure 4.7. Stress-strain curve of (a) compression molded plates and (b) as-spun fibers of neat HDPE and selected HDPE nanocomposites containing 0.5 and 2% of LDH.

Composition	Tensile modulus [GPa]	Yield stress [MPa]	Strain at yield [%]	Stress at break [MPa	Elongation at break [%]
HDPE	0.96±0.01	31±1	11±1	26±4	1766±166
LDH-0.5	0.95±0.02	31±1	11±1	29±1	1933±30
LDH-1	1.01±0.03	31±1	11±1	25±1	1590±63
LDH-2	1.03±0.02	31±1	11±1	21±3	1205±144
LDH-5	1.04±0.04	30±1	14±1	17±1	378±60

Table 4.4. Tensile mechanical properties of neat HDPE and nanofilled HDPE plates.

Samples	Tensile modulus [GPa]	Yield stress [MPa]	Strain at break [%]	Stress at break [MPa]	Strain at break [%]	Mechanical draw ratio	Calculated maximum strength** [MPa]	Linear density* [tex]	Tenacity* [cN/tex]
HDPE	0.55±0.02	22±2	8±2	42±1	1206±20	13.1	549	187	4.4±0.1
LDH0.5	0.53±0.01	25±1	16±1	56±4	1860±60	19.6	1098	185	5.9±0.4
LDH-1	0.60±0.08	22±1	11±4	52±6	1360±60	14.6	759	188	5.4±0.6
LDH-2	0.62±0.02	22±1	11±1	53±1	1770±42	18.7	991	192	5.4±0.1
LDH-3	0.66±0.02	23±1	12±1	43±1	1470±70	15.7	675	193	4.4±0.1

** for definition of linear density and tenacity see ASTM [125] and Eg. (4.4). ** calculated according to Eq.(4.3)*

Table 4.5. Tensile mechanical properties of neat HDPE and nanofilled HDPE fibers (diameter 500 micron).

At higher LDH content, a progressive stiffening of both plates and fibers was achieved as expected. The elastic modulus increased up to 1.04 GPa for LDH-5 plates, and up to 0.66GPa for LDH-3 fibers. It is well known that mechanical properties of a nanocomposites depend upon these two factors, crystallinity of the matrix and reinforcement of the filler [96]. For such considerations, if the elastic modulus of polyethylene and LDH-composite will be compared as a function of the crystallinity a good correlation between the two groups of plates and fibers data can be observed. The main difference of modulus values can be directly attributed to the different processing conditions, because they affected the crystallinity content.

A similar dependence on the crystalline content, was also found in the case of yield stress, resulting about 30 MPa for all the plates (with 70-73% of crystallinity) and about 22 MPa for the fibers (with 50-55% of crystallinity).

Moreover the effect of the nanofiller content on the tensile modulus can be specifically clarified after the comparison of the relative stiffness of plates and fibers. In particular the relative elastic modulus (*REM*) was calculated as the ratio between the composite modulus ($E_{HDPE-LDH}$) and the matrix modulus (E_{HDPE}) according to equation (4.1)

$$REM = \frac{E_{HDPE-LDH}}{E_{HDPE}} \qquad (4.1)$$

and it was depicted in Figure 4.8. It is quite evident that the initial reduction for composition at 0.5% of LDH, is followed by a slight increase in the case of plate up to about 7% for LDH-5, and a much higher increment for the fibers (about 20% for LDH-3). This latter effect of stiffening is particularly related to the spinning process,

for which the twin screw extrusion at higher temperature determined a better distribution of the filler and the following interaction with the oriented polymer chains.

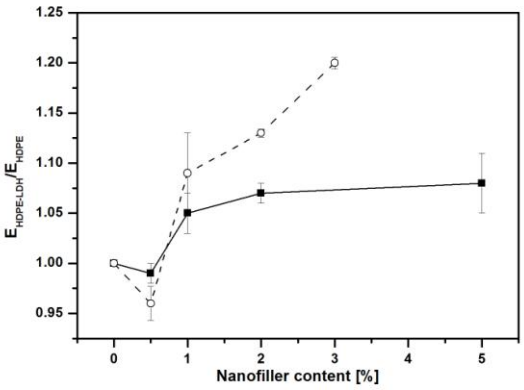

Figure 4.8. Comparison of relative elastic modulus of plates (■) and fibers (○) as function of nanofiller content.

The comparison of ultimate properties evidenced the higher strength of fibers (Table 4.5) with respect to plates (Table 4.4), as result of polymer orientation during the spinning process. Moreover, in the case of fiber a good improvement of stress at break was obtained with hydrotalcite, from 42-46 MPa for neat HDPE, up to 52-56 MPa for nanocomposite at LDH content in the range 0.5-2 %. These results could be related to the better filler dispersion and the smaller dimension of hydrotalcite aggregates.

On the other hand, as expected, at higher LDH content, the stiffening effect was also counterbalanced by a consistent and progressive reduction of tensile properties at break, in conformity to other literature data [104, 106, 107]. For instance the strain at break of plates decreased from about 1700% for HDPE plates to 380 % for LDH-5. The decrease in both tensile strength and strain at break at high nanofiller content, particularly in LDH-5 plates and LDH-3 fibers, has been attributed to the presence of hydrotalcite aggregates, that may behaves as defects, and could also reduce the interfacial adhesion between the matrix and the filler [29, 108].

Some other indications on the fiber drawing can be evaluated from the mechanical draw ratio λ_{MEC}, or the maximum drawability that is defined according to Equation (4.2):

$$\lambda_{MEC} = 1 + \frac{\varepsilon_b}{100} \quad (4.2)$$

where ε_b is the strain at break expressed in percentage [103, 109].

In the same time, the maximum attainable strength σ_{MAX}, is computable from the stress at break, $\sigma_b$multiplied by the mechanical draw ratio, following Equation (4.3):

$$\sigma_{MAX} = \sigma_b \cdot \lambda_{MEC} = \sigma_b(1 + \frac{\varepsilon_b}{100}) \quad (4.3).$$

Perhaps, the most important properties of the physical properties of fibers is tensile strength, because this parameter is basic to its utilization as textile fibers and can be reported in several strength units. Tenacity as a strength unit is defined as the breaking load in grams divided by linear density and is defined by Equation 4.4:

$$Tenacity\ [N/tex] = \frac{\sigma_b}{\rho} \cdot 10^{-3} \quad (4.4)$$

where σ_b is the stress at break expressed in MPa and ρ is density of the fiber in g/cm^3. Linear density, the mass or weight of a unit length of fiber, may be given as micrograms per inch or centimeter, but more commonly as grams per 1000, designed as tex [60].

These data are compared in Table 4.5. Mechanical draw ratio of nanocomposite fiber ranged in between 15-20, and correspondingly the calculated maximum strength was between 670 MPa and 1100 MPa, with respect to the values of 13 and about 550 MPa of HDPE fibers, respectively. The highest mechanical draw ratio and the maximum strength were obtained for composition at 0.5% of LDH.

The linear density [110] of spun monofilament slightly increased with the LDH content, from 187 tex of neat HDPE fiber up to 193 tex of LDH-3 fiber. At the same time, the tenacity of nanocomposite fibers containing 0.5-2% of LDH was found in the range of 5.4-5.9 cN/tex, much higher than neat HDPE fiber (4.4 cN/tex) indicating the positive effect of LDH dispersion. On the other hand, at higher LDH content, both the stress at break and tenacity decreased as a possible consequence of nonhomogeneous nanofiller dispersion.

4.1.5. Summary HDPE-LDH composite processing

HDPE composites with organically modified hydrotalcite were prepared following two different compounding routes, i.e. internal mixing and compression molding, or twin-screw extrusion and spinning. The effect of filler on the thermo-mechanical properties of high density polyethylene was investigated on compression molded plates and as-spun fibers. In both cases, the dispersion of nanoparticles in the range of 0.5-5% significantly improved the thermal stability and the elastic modulus of HDPE. The stiffening effect of nanofiller was also confirmed by the proportional increase of Shore D hardness values.

Depending on the lower cooling rate after compression molding, HDPE plates showed a higher crystallinity with respect to the fibers. However, nanocomposites fibers showed a higher improvement of the relative elastic modulus with respect to the nanocomposites plates containing the same percentage of nanofiller. This behavior could be a consequence of the different orientation and morphology related to the crystallinity developed in the spinning. These results confirmed that polyethylene containing organically modified hydrotalcite could be easily spinned into nanofilled fiber.

4.2. HDPE-LDH nanocomposite drawn fibres

As spun fibres were drawn in a hot-plate drawing apparatus 1.4 m length (SSM-Giudici srl, Galbiate, LC, Italy). Three different temperatures 100°C, 125°C and 140°C, a constant feeding rate of 1.2 m/min and various collecting rates were selected. Drawn fibers were distinguished in dependence on the draw ratio (DR) that is defined as the ratio between the cross section of the initial (S_i) and final fiber (S_f) according to Eq.3.1. The diameter of the fiber was measured by using an optical microscope connected to image processing software (ImageJ®).

4.2.1. Non isothermal crystallization kinetics

In order to collect complementary information on the effect of crystallization temperature during drawing, a deeper investigation on the crystallization kinetics of HDPE nanocomposites analysis was performed. DSC results of the non-isothermal crystallization at different cooling rate between -0.3°C/min and -40°C/min are summarized in Table 4.6. Higher crystallization temperatures of the LDH nanocomposites seem to confirm a nucleating effect of hydrotalcite [85, 111].

The experimental data in three selected temperature intervals were fitted with straight lines whose slopes express the activation energy determined by using the Kissinger approach:

$$lnC = lnC_0 - \left(\frac{E_{act}}{R}\right) 1/T_c \qquad (4.5)$$

where C_0 is a pre-exponential factor, T_c is the peak temperature and R is the universal gas constant [112].

Materials	T_c [°C]							
	0.3 [°C/min]	0.5 [°C/min]	1 [°C/min]	2 [°C/min]	5 [°C/min]	10 [°C/min]	20 [°C/min]	40 [°C/min]
HDPE	124.3	123.8	122.6	120.7	117.6	111.3	107.5	99.8
LDH-0.5	124.3	123.6	122.2	119.7	115.8	112.2	102.5	91.1
LDH-1	124.2	123.6	122.7	121.3	118.6	112.4	110.0	101.3
LDH-2	123.9	123.3	122.3	121.3	118.7	113.0	110.0	101.2
LDH-3	123.9	123.5	122.6	121.1	118.4	115.1	110.0	103.7

Table 4.6. Crystallization temperature (T_c) of neat HDPE and HDPE nanocomposites obtained for different cooling rate for as-spun fibers.

Figure 4.9 evidences the case of HDPE and LDH-2 for which the three straight lines could be related to the different mechanisms of the crystallization regimes I, II and III of the Hoffman theory, and their intersection is related to the transition temperature between different regimes. For linear polyethylene, transition temperatures of 127°C and 119°C for regime I/II and regime II/III, respectively, were reported [113]. In our case, both transition temperatures and the activation energies of the regimes are summarized in Table 4.7. The transition temperatures for the neat HDPE ($T_{I/II}$ =123.8°C and $T_{II/III}$ =117.5°C) are slightly lower in comparison to literature data. In the case of HDPE/LDH nanocomposites $T_{I/II} \approx 122$°C, whereas the temperature transition between regime II and III was found at 119.0°C for LDH-1 and LDH-2. Moreover, the neat HDPE activation energies of 894, 410 and 140 kJ/mol for regime I, II and III were calculated, respectively; whereas the calculated activation energies of regime I (about 1050 kJ/mol) and regime II (about 500 kJ/mol) of nanocomposites with 1-3% of LDH are higher than those of the neat HDPE. Such higher activation energy could be related to lower molecular mobility in the LDH nanocomposites, while a higher crystallization temperature could be attributed to the heterogeneous nucleation of hydrotalcite particles. Similar results were previously observed for the HDPE/$BaSO_4$ nanocomposites [114]. Thus, two different roles could be attributed to the LDH nanoparticles: first, they acted as nucleating agents and promoted the crystallization process of HDPE; second, they simultaneously acted as physical hindrances, thus retarding crystal growth of HDPE [114].

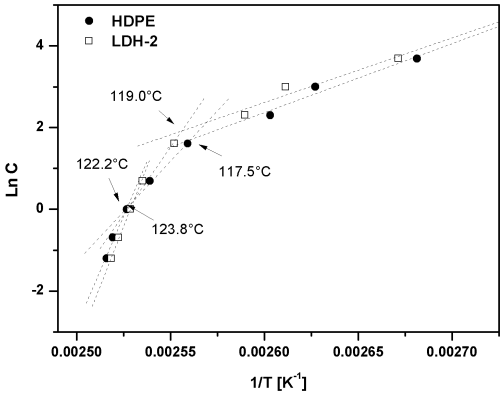

Figure 4.9. Plot of cooling rate C (-K/min) versus crystallization temperature ($1/T_c$) for neat HDPE and LDH-2 nanocomposites fibers. Dot lines represent the best fitting lines; the intersection of the lines corresponds to the transition temperature between Regime I/II and Regime II/III.

Materials	$T_{I/II}$ [°C]	$T_{II/III}$ [°C]	$E_{act\ I}$ [kJ/mol]	$E_{act\ II}$ [kJ/mol]	$E_{act\ III}$ [kJ/mol]
HDPE	123.8	117.5	894±123	410±25	140±31
LDH-0.5	122.2	114.4	734±77	320±16	77±5
LDH-1	122.7	119.0	1046±30	496±20	137±25
LDH-2	122.2	119.0	974±56	551±30	131±35
LDH-3	122.7	117.5	1175±156	486±42	149±8

Table 4.7. Transition temperature ($T_{I/II}$ and $T_{II/III}$) and activation energy of crystallization (E_{act}) following regime I, II and III for neat HDPE and HDPE-LDH composites.

4.2.2. Drawing process

After the melt spinning process nanocomposite materials were hot-drawn. In order to select the best processing condition the drawing process was conducted in air at three different temperatures. A deeper study on three drawing temperatures is presented in this paragraph; in particular all the fibers compositions were drawn at three different temperatures; 100°C which is the temperature of regime III crystallization, and at two higher temperatures, 125 °C and 140 °C, in the regime of crystallization type II and I.

For the neat HDPE and LDH-2 both elastic modulus and stress at break of fibers drawn at various temperatures are compared in Figure 4.10 and in Figure 4.11.

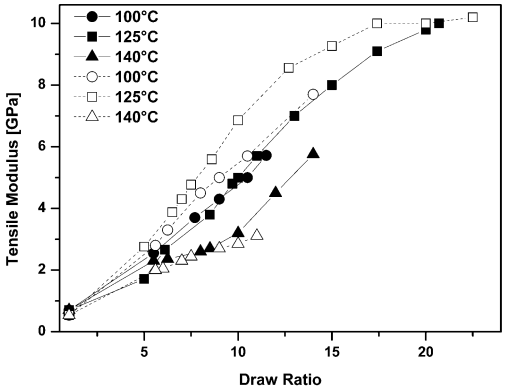

Figure 4.10. Elastic modulus of neat HDPE (full symbol) and LDH-2 (empty symbol) fibers for different drawing temperature (○– 100°C, □– 125°C and Δ – 140°C) as a function of draw ratio.

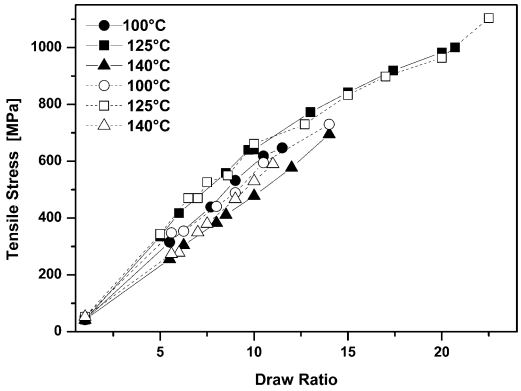

Figure 4.11. Stress at break of neat HDPE (full symbol) and LDH-2 (empty symbol) fibers for different drawing temperature (○– 100°C, □ – 125°C and Δ– 140°C) as a function of draw ratio.

The elastic modulus of the neat HDPE fibers with DR=10 was found 3.0 GPa and 5.0 GPa after drawing at 140 °C and at 100 °C, respectively, whereas a value of 5.2 GPa was reached for drawing temperature of 125 °C (Fig. 4.10.). In the case of

LDH-2 fiber the same tendency was observed, with elastic modulus of 3.1 GPa after drawing ten times at 140 °C, 5.8 GPa at 100 °C and 6.9 GPa at 125 °C.

Figure 4.11 shows similar trends for stress at break. For DR=10, the neat HDPE fibers show the highest stress at break (640 MPa) for drawing temperature of 125 °C; slightly lower values were found at 100 °C (590 MPa) and 140 °C (480 MPa). The trends observed for the LDH nanofilled fibers are quite analogous, (660, 470, 530 MPa, respectively).

The dependence of fiber mechanical properties on drawing temperature could be interpreted in term of crystallization-induced-orientation, and also taking into consideration the different crystallization forms and regimes, as briefly summarized by the description of Hoffman and coworkers [113]. In regime I, secondary nucleation rate is slow allowing for completion of the nucleated layer before the next event of the secondary nucleation; in the regime II, their rates are comparable to allow multiple nucleation, finally during III regime surface spreading is lower than the nucleation rate. Hence, fibers drawn at the lower temperature (100 °C) could develop further crystallization according to crystallization regime III, where the nucleation rate is slow, and thus accounting for lower crystallinity content. Moreover, in regime III zone similar activation energy $E_{act\ III}$ of about 135 kJ/mol was found for both HDPE and LDH-2. The highest mechanical properties (Figures 4.10. and 4.11.) were obtained for HDPE and LDH-2 fibers drawn at 125 °C, where HDPE crystallized according to regime II and I, so that both nucleation and growth rates are comparable. At 140 °C, crystallization proceeds owing mainly to the intense nucleation because the nucleation rate is higher than surface spreading, and hence lower mechanical properties were achieved. These results, even those of LDH-2, are in agreement with data of HDPE fibers reported by Ward, where the highest elastic modulus and the draw ratio were achieved for drawing temperature close to 120°C [7].

4.2.3. Characterization of fibres drawn at 125°C

Following our previous findings, 125°C was selected as drawing temperature for both HDPE and all other LDH nanocomposites, and an extensive study is reported in

the next paragraphs, where XRD analysis and thermal and mechanical characterization are described.

4.2.4. TEM analysis

TEM images of the ultramicrotomed cross section of nanofilled HDPE fibers at DR=1 (as-spun material), DR=5 and DR=20 are reported in Figure 4.12.a-d, 4.12.e-g and 4.12.h-k respectively.

As we could expect undrawn fibers are characterized by the presence of uniformly dispersed hydrotalcite forming clusters of aggregated with size of the primary nanoparticles lower than 250nm (Fig. 4.12.a). What is more we can see that aggregates are relatively small and well dispersed in the matrix. Similar microstructural results were observed by SEM analysis (see chapter 4.1.1). From the images with higher magnification (Fig. 4.12.b-d) it can be observed that the LDH slightly intercalated polymer matrix. This means that melt spinning process does not have a significant impact on the microstructural behavior of the prepared materials, because chain alignment along the flow direction is not followed by a deformation and rupture of LDH aggregates. This is an explanation of very similar tensile properties of as-spun unfilled and nanofilled fibers. Similar observations were already reported in case of HDPE fumed nanosilica fibers [82].

In the Figure 4.12.e-g and 4.12.h-k TEM observations for drawn material are reported. For both draw ratios good LDH distribution was obtained. In case of material drawn with DR=5 LDH size are in the range from 200nm up to 500nm (Fig.4.12.e-g). However, for DR=20 also lower size of the filler around 100nm were found (Figure 4.12.h-k.). We can conclude that LDH microstructures are smaller for drawn material. Drawing process induces the rupture of hydrotalcite aggregates and alignment along the strain direction. The intercalation and exfoliated of polymer matrix occurred what results an improvement of elastic, storage modulus and strength observed for nanofilled drawn fibers.

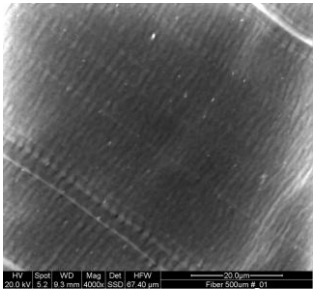

Fig. 4.12.a TEM micrograph of LDH-0.5.

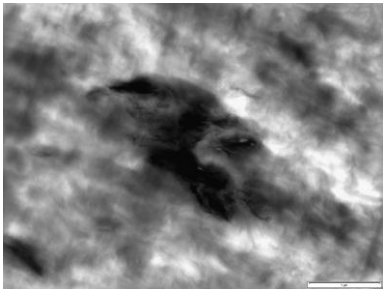

Fig. 4.12.b TEM micrograph of LDH-0.5.

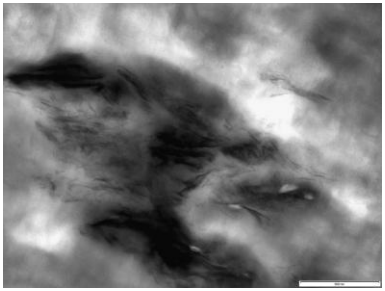

Fig. 4.12.c TEM micrograph of LDH-0.5 DR=1.

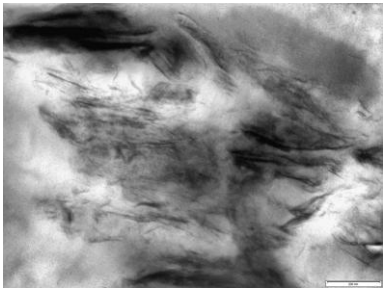

Fig. 4.12.d TEM micrograph of LDH-0.5 DR=1.

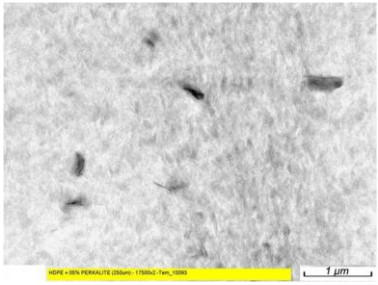

Fig. 4.12.e TEM micrograph of LDH-0.5 DR=5.

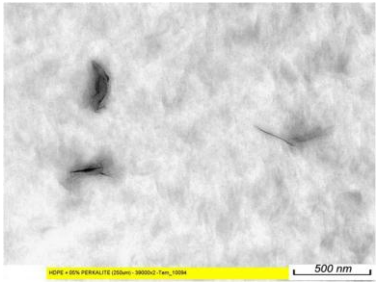

Fig. 4.12.f TEM micrograph of LDH-0.5 DR=5.

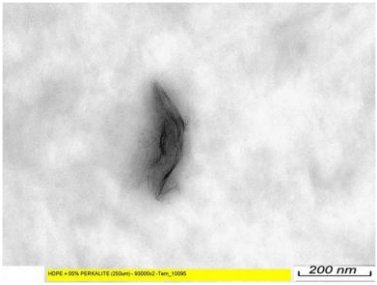

Fig. 4.12.g TEM micrograph of LDH-0.5 DR=5.

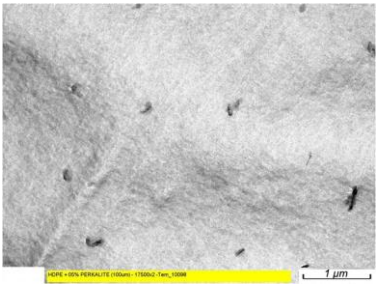

Fig. 4.12.f TEM micrograph of LDH-0.5 DR=20.

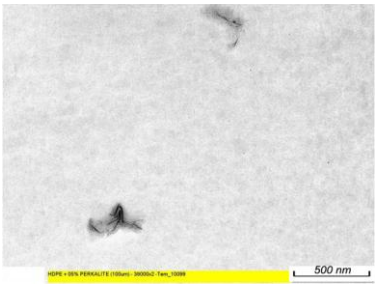

Fig. 4.12.i TEM micrograph of LDH-0.5 DR=20.

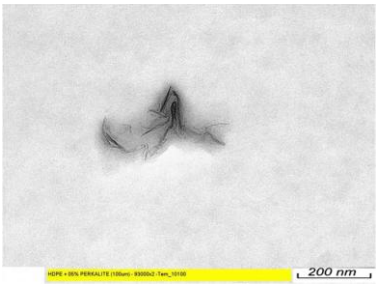

Fig. 4.12.j TEM micrograph of LDH-0.5 DR=20.

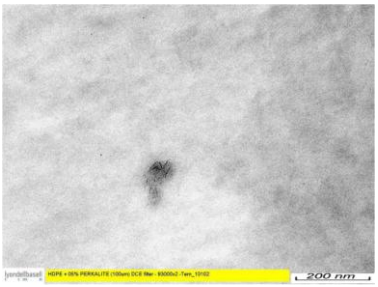

Fig. 4.12.k TEM micrograph of LDH-0.5 DR=20.

Figure 4.12. TEM images of ultra-microtomed cross-section of (a-d) undrawn nanocomposite fibers and drawn with (e-g) DR=5 and (h-k) DR=20 with different magnification.

4.2.5. XRD analysis

The XRD analyses of the HDPE/LDH as-spun and selected drawn fibers are shown in Figures 4.13.a-c, in order to evaluate the extent of intercalation and exfoliation of the nanofiller.

a)

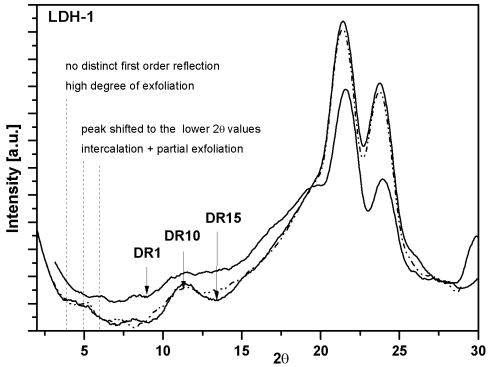

b)

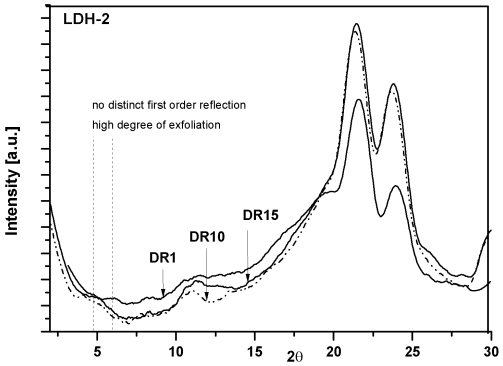

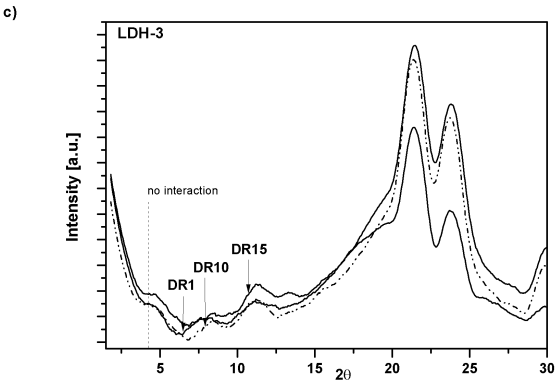

Figure 4.13. XRD patterns of HDPE-LDH nanocomposites fibers with selected draw ration (DR) and different nanofiller content (a) LDH-1, (b) LDH-2 and (c) LDH-3.

The XRD pattern were interpreted with respect to the position of the basal peak (003) of the hydrotalcite phase ($Mg_6Al_2(CO_3)(OH)_{16}\cdot 4H_2O$, PDF card n. 41-1428), which depends on the distance between two adjacent metal hydroxide sheet in the LDH crystal lattice. The higher order peak of the same hkl series (006, 009) was also reported and both peaks indicate the presence of repeating crystal planes and symmetry in a specific crystallographic direction [48]. On the XRD spectra of LDH-1 nanocomposites, three characteristic Bragg reflections at about 6° (003), 8.1° (006) and 11.5° (009) of LDH presence can be observed (Fig.4.13.a). The first and the third can be univocally attributed to (003) and (006) reflexes of the reported reference phase, set at 5.48° and 11.27°, respectively. The second peak can be tentatively assigned to a minor Dypingite phase (ICPDS Powder Diffraction File card n. 23-1218), present in the starting mineral raw material. After the drawing process (DR=10) the XRD patterns show change in the position of the basal reflection of the HDPE/LDH nanocomposites. For LDH-1 the peaks were shifted respectively from 6° up to 5.2° and 8.1° till 7.2° (Fig 4.13.a). As reported by other researchers, these results might suggest possible intercalation along with partial exfoliation [48, 86, 87]. In the case of LDH-2 the first basal reflections become very broad and the maximum of the bands, from 8.2° and 11.5°, shifts to lower 2θ, 7.8° and 11.0° respectively, as

compared to as-spun fiber (Fig. 4.13.b). Moreover, in order to check the change in LDH intercalation/exfoliation process during drawing, XRD analyses for DR=15 samples were also performed. In this case the first basal peak cannot be observed for both compositions LDH-1 and LDH-2, while the position of the other two peaks remains unchanged in comparison to DR10. This suggests that with further drawing the exfoliation process is more effective. On the other hand, the results of LDH-3 were reported in Fig. 4.13.c, and no change in the position of the three peaks was observed, even at high draw ratio. These findings suggested that nanoparticles in LDH-3 were not well dispersed and the formation of aggregates prevented the intercalation process [86]. Moreover, it is worth noting the increase of intensity of the peaks related to the polyethylene (21.4° and 23.7°) after drawing for all LDH composition. High enhancement of crystallinity content was obtained up to DR=10, whereas after higher drawing (DR=15) only minor variations were observed, in agreement with DSC analysis (see next paragraph). The overall XRD results confirmed that LDH layers were partially/fully separated with the formation of an intercalated/exfoliated [115]. It can be concluded that XRD analysis of HDPE nanocomposites fibers shows significant change in the position of the basal peak after drawing process. Moreover the disappearance of the (003) peak for LDH-1 and LDH-2 at DR=15, suggested that LDH particles undergo more and more fragmentation during drawing process and lose their order structures to a great extent [86].

4.2.6. Differential Scanning Calorimetry

DSC thermograms of the first heating scan for neat HDPE and LDH-2 nanocomposite fibers with different draw ratios are compared in Figure 4.14., while all results of the heating-cooling-heating cycle are summarized in Table 4.8.

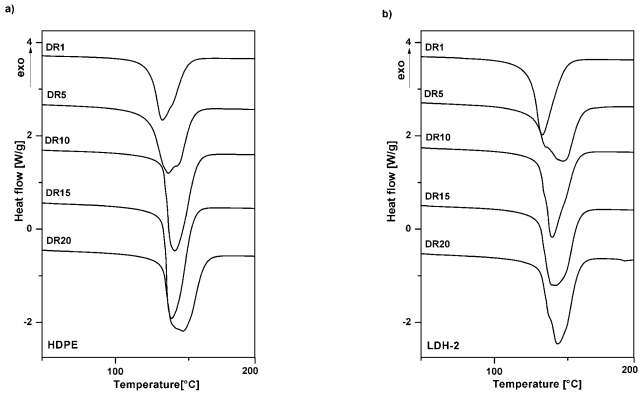

Figure 4.14. First heating DSC thermograms (a) neat HDPE and (b) LDH-2 for different draw ratio (DR).

Material	Draw ratio	Heating		Cooling		Heating	
		Crystallinity Content Xc [%]	Melting Temperature T_m [°C]	Crystallinity Content Xc [%]	Crystallization Temperature T_c [°C]	Crystallinity Content Xc [%]	Melting Temperature T_m [°C]
HDPE	1	50	133	65	111	65	143
	5	65	136	70	113	70	141
	10	70	140	68	114	68	138
	15	75	138	71	114	71	136
	20	74	146	71	111	71	140
LDH-0.5	1	52	133	70	112	70	142
	5	69	142	70	112	70	144
	10	70	142	70	113	70	141
	15	76	138	72	116	72	136
	20	75	140	71	109	71	137
LDH-1	1	53	133	68	112	68	142
	5	66	142	69	113	69	141
	10	69	141	66	114	65	140
	15	78	139	72	114	72	139
	20	77	140	74	112	74	140
LDH-2	1	54	132	66	113	66	141
	5	60	146	66	114	66	140
	10	66	144	66	114	66	140
	15	74	142	71	112	71	139
	20	74	143	71	114	71	139
LDH-3	1	53	133	69	115	69	137
	5	62	144	63	114	63	139
	10	68	143	65	116	65	139
	15	73	137	73	116	73	138
	20	74	140	73	116	73	138

Table 4.8. Results of the DSC analysis: crystallinity content (X_c), melting temperature (T_m), and crystallization temperature (T_c) for neat HDPE and HDPE nanocomposite fibers.

Melting temperature of the as-spun HDPE and LDH nanocomposite fibers was found at 133°C, (Table 4.8.), whereas a higher crystallinity content was detected for LDH fiber (52-54% vs 50% of neat HDPE), in conformity to literature data of polyolefin/clay nanocomposites [100, 116, 117]. The increase in fiber orientation upon solid - state drawing determined not only an increase in the melting temperature up to 140-146°C, but also in the degree of crystallinity from about 50 % up to 74 - 78 %. The highest crystallinity content was found for LDH-1 (78% at DR15). The multiple melting peaks observed for fibers with DR = 5 (Fig. 4.14.), are related to the difference of crystal forms or the degree of their perfection obtained during drawing. The substantial increase of crystallinity of LDH composite fibers in comparison to neat HDPE was obtained for draw ratio between 5 and 10, reaching an almost plateau value for drawing 15-20. The degree of crystallinity of oriented samples follows a trend similar to that of the melting temperature, i.e. both quantities increase with orientation and level off at higher degrees of molecular chain alignment [118]. In particular the orientation-induced crystallization, and typical folded - chain lamellar structure of flexible polymers convert into the extended–chain structure [119]. In the cooling step, the crystallization temperature of the as-spun LDH composite was found 1–4 °C higher than that of the neat HDPE, confirming the role of hydrotalcite as nucleating agent, in conformity to other literature data [85, 106]. It can be concluded that during drawing at 125°C, the higher the draw ratio, the higher polymer chains orientation, and the higher crystallinity, particularly effective in the case of LDH-1 fiber.

4.2.7. Mechanical Properties

Representative stress-strain curves of the neat HDPE and nanofilled polyethylene fibers at different draw ratio are reported in Figure 4.15, while the most relevant mechanical parameters are summarized in Table 4.9.

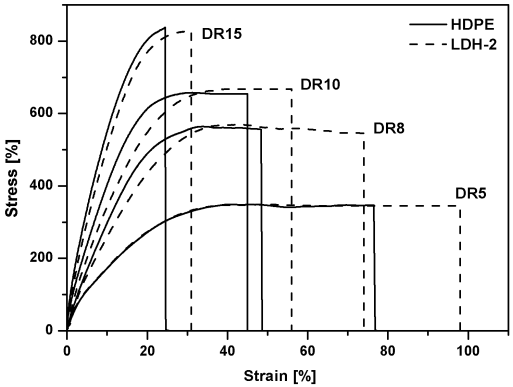

Figure 4.15. Representative stress-strain curves for neat HDPE and LDH-2 from quasi-static tensile tests for different draw ratio (DR).

Material	DR	Linear density[a] [tex]	Elastic modulus [GPa]	Stress at break [MPa]	Strain at break [%]	Tenacity[a] [cN/tex]	Calculated max. strength[b] σ_{MAX} [MPa]	Mechanical draw ratio λ_{MEC}	Total draw ratio λ_{TOT}	Relative stiffening factor[c]
HDPE	1	182.0	0.55±0.02	42±1	1206±20	4.5	549	13.1	142.2	1.0
	5	37.7	1.71±0.23	335±15	70±10	36.8	570	1.70	91.4	3.1
	10	16.9	5.04±0.25	642±18	47±4	67.5	963	1.47	177.8	9.1
	15	12.7	8.02±0.55	842±45	20±4	87.2	1010	1.20	193.2	14.5
	20	9.1	9.80±0.25	983±40	16±3	102.6	1179	1.16	261.0	17.8
LDH-0.5	1	182.5	0.53±0.01	56±4	1860±60	6.0	1098	19.6	213.4	1.0
	5	38.0	1.94±0.15	274±17	105±5	29.0	548	2.05	110.3	3.7
	10	16.9	5.45±0.30	586±25	43±4	61.6	820	1.43	173.0	10.3
	15	12.8	8.86±0.51	742±15	27±5	75.0	964	1.27	204.5	16.7
	20	9.2	10.0±0.6	865±13	17±3	81.2	1040	1.17	263.2	18.8
LDH-1	1	183.0	0.60±0.04	52±6	1360±60	5.7	759	14.6	158.9	1.0
	5	37.8	2.85±0.13	340±12	66±12	36.7	578	1.66	89.3	4.8
	10	16.8	6.51±0.45	680±50	26±7	71.0	884	1.26	152.5	10.8
	15	12.8	9.02±0.31	786±35	17±6	79.4	943	1.17	188.4	15.0
	20	9.2	10.3±0.5	865±27	15±2	80.0	951	1.15	158.7	16.3
LDH-2	1	183.1	0.62±0.02	53±1	1770±42	5.6	991	18.7	203.6	1.0
	5	37.4	2.76±0.15	344±27	98±17	38.0	688	1.98	106.5	4.45
	10	16.8	6.86±0.51	661±18	56±14	70.2	1057	1.56	188.7	11.1
	15	12.7	9.27±0.45	833±52	27±7	86.5	1083	1.27	204.5	15.0
	20	9.1	10.0±0.5	964±25	14±3	95.6	1060	1.14	256.5	16.1
LDH-3	1	182.8	0.66±0.02	43±1	1470±70	4.6	675	15.7	171.0	1.0
	5	37.5	2.31±0.13	246±20	98±15	37.2	492	1.98	106.5	3.5
	10	16.8	6.04±0.38	600±14	52±9	62.6	900	1.52	184.0	9.1
	15	12.7	8.51±0.55	753±18	21±5	79.0	904	1.21	200.8	12.8
	20	9.1	10.3±0.3	888±15	20±3	92.2	1065	1.20	270.0	15.6

[a] for definition of linear density and tenacity see ASTM [110] and Eq. (4.4). [b] calculated according to Eq.(4.3). [c] calculated as ratio modulus between drawn fiber and as-span fiber.

Table 4.9. Selected mechanical properties of neat HDPE and nanofilled HDPE fibers at various draw ratio (DR).

It can be seen that fibers do not manifest a clear yield point at lower strains as usually observed for as-spun products. In fact, the drawing process produces a strong orientation of the macromolecules along the draw direction and the strain-induced crystallization of the amorphous regions, with a consequent increase in the fiber stiffness and the disappearance of yielding phenomena. These results are in conformity to previous researches, where a good dispersion enhanced the elastic modulus and the strength, and reduced the tensile ductility in comparison to neat matrix [85, 93, 120].

Tensile modulus values at different draw ratios are reported in Figure 4.16. It is worth noting that the stiffness of the nanofilled fibers notably increased with only a few weight percent of hydrotalcite. The highest improvement was obtained for LDH-1 and LDH-2 samples, whose tensile modulus at DR = 15 reached 9.0 GPa and 9.3 GPa respectively, in comparison to 8.0 GPa of the neat HDPE.

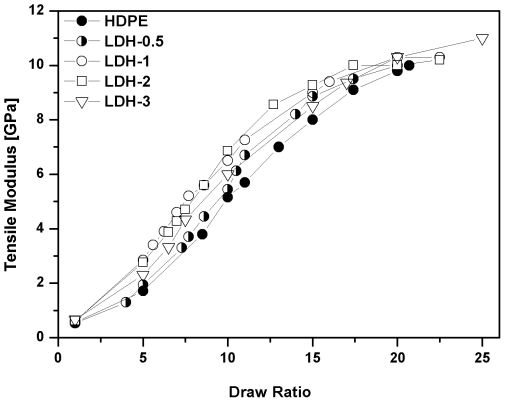

Figure 4.16. Effect of draw ratio (DR) on elastic modulus of neat and nanofilled HDPE fibers with different amount of hydrotalcite after drawing at 125°C.

The positive effect of the nanofiller on the tensile modulus can be explained by the percolation theory described by He and Jiang [107]. According to these authors, the matrix zone around each particle is affected by the stress concentration. If the distance between particles is small enough, these zones join together and form a percolation network which increases the modulus. For constant filler loadings, if the

particles are fine and well dispersed, the total volume will be high, and the distance between the particles will be small. Therefore, the percolation network develops more easily and the modulus increases. The uniform nanofiller dispersion in case of compositions with 1 and 2 %wt of LDH was observed by SEM analysis (see Figure 4.1.).

The stiffening effect provided by LDH nanoparticles at various draw ratios is well documented by the relative tensile modulus *REM* (Figure 4.17.) calculated according to the equation 4.1. From obtained data summarized in Table 4.9 it was found that relative modulus increase with the nanofiller content reaching a relative maximum for LDH-1 and LDH-2, particularly significant at DR5 and DR10. Moreover, at the highest concentration of hydrotalcite (3% wt.), a lower stiffening effect (Figure 4.17.) and modest increase of stress at break (Table 4.9.) are especially visible for higher draw ratio (DR > 10). These effects can be explained in terms of filler dispersion, as reported by Costa et al. in the case of polyethylene/Mg-Al LDH nanocomposites, describing a critical concentration range of 2.5 - 5% wt. above which the LDH particles do not show strong interfacial adhesion with the matrix [48]. The existence of an optimal amount of the nanofiller was already observed by several authors [121-123]. In this paper, the critical concentration of LDH in HDPE for fiber spinning was found at 2% wt. Above this concentration, hydrotalcite cannot be easily dispersed; clay will agglomerate in micrometric clusters acting as defects and stress concentration points that decrease drawability and polymer alignment.

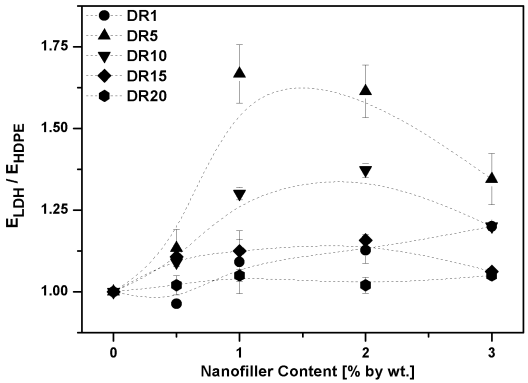

Figure 4.17. Relative elastic modulus of HDPE-LDH nanocomposites with different amount of hydrotalcite after drawing at 125°C.

It is well known that the mechanical properties of polymer fibers can be remarkably affected by the degree of crystallinity [121, 124]. In Figure 4.18 tensile modulus at various DR and LDH content versus crystallinity content was plotted. It can be noted a proportional relationship between crystallinity content and tensile modulus. Drawn fiber of LDH-2 sample at high draw ratio reached the higher modulus values at relatively low crystallinity content, with respect to other fibers. This behaviour suggests that the improvement in mechanical properties is related to various factors, such as the nanofiller content, orientation and crystallinity that could play a synergistic role.

Stress at break values of the neat and nanofilled HDPE fibers were plotted versus draw ratio in Fig. 4.19. Scientific literature showed various dependency of stress at break on nanofiller content, either increasing values after addition of 0.5-5 wt% of nanofiller, or unchanged, or even decreasing results, as in the case of nanofilled polypropylene fibers [82, 125-127]. In the present case, stress at break for LDH-1 and LDH-2 remained practically unchanged in comparison to that of neat HDPE fibers (Figure 4.19.) up to DR15. Slightly lower values were found for the fibers with 0.5 % wt. and 3 % wt. of LDH.

Figure 4.20 shows the decreasing of strain at break values at the increase of draw ratio. All the compositions of as-spun HDPE-LDH fibers evidence higher strain at break than that of the neat HDPE fiber. With the higher draw ratio, strain at break decreases from about 1200% for as-spun HDPE and 1860% for LDH-0.5 up to 16% and 17% respectively for the fibers with DR=20. As interpreted by E. Bilotti *et al.*, the drawability of melt-crystallized flexible chain polymers achieved by drawing is limited by the presence of molecular entanglements [128].

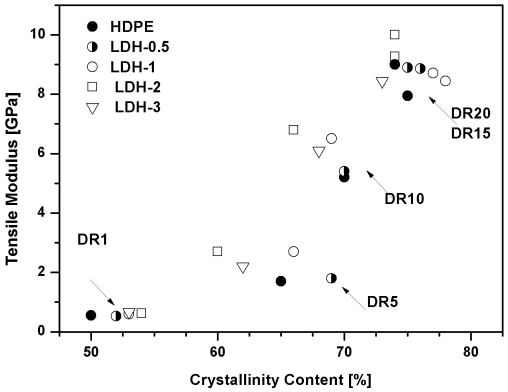

Figure 4.18. Elastic modulus of neat and nanocomposite HDPE fibers as a function of the degree of polymer crystallinity.

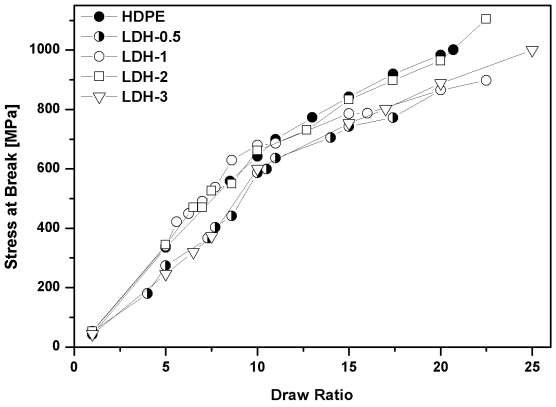

Figure 4.19. Stress at break of neat and nanocomposite HDPE fibers with different amount of hydrotalcite as a function of draw ratio (DR) after drawing at 125°C.

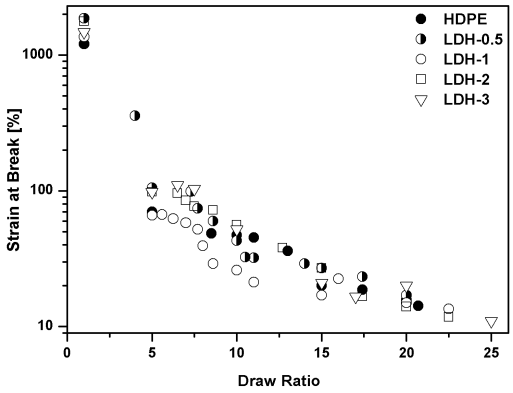

Figure 4.20. Strain at break of neat and nanocomposite HDPE fibers with different amount of hydrotalcite as a function of draw ratio (DR) after drawing at 125°C.

Some more information about spinnability and drawability could be obtained considering the mechanical draw ratio (λ_{MEC}) Eq.4.2, the true strength (σ^*_{MAX}) Eq.4.3 the processing draw ratio (λ_{PRO}), and the total draw ratio (λ_{TOT}) of selected fibers, as described in the followings and compared in Table 4.9.

The processing draw ratio (λ_{PRO}) is defined as the ratio between the section of the die S_d and the section of the fiber S_f according to Eq. 4.6:

$$\lambda_{PRO} = \frac{S_d}{S_f} \tag{4.6}$$

And the total draw ratio (λ_{TOT}) has been calculated from Eq. 4.7:

$$\lambda_{TOT} = \lambda_{PRO} + \lambda_{MEC} \tag{4.7}$$

which depends on both processing and mechanical drawing [129].

For the as-spun fibers, higher true strength values were obtained for all the composites with hydrotalcite. For example, the true strength of LDH as-spun fibers is between σ_{MAX}=675-1098 MPa and their total draw ratio from λ_{TOT}=159-213, whereas the correspondent values of the neat HDPE as-spun fibers are 549 MPa and 142, respectively. In the case of drawn fibers, true strength and mechanical draw ratio are very similar for both neat and nanofilled HDPE fibers. Also the total draw ratio indicates that LDH fiber could be spun and drawn at the same levels of HDPE fiber, confirming the good processability of hydrotalcite composites.

Moreover, a quantitative evaluation of the fiber properties and drawability of each composition could be remarked considering the draw-stiffening factor, calculated as the ratio between modulus of drawn fiber and modulus of as spun fiber, also reported in Table 4.9. These values are directly dependent on the draw ratio, and it is well evident the higher draw-stiffening factor of the LDH fiber containing 0.5-2% of hydrotalcite, with respect to the neat HDPE fiber up to DR15. Once again similar or lower values for LDH-3 were observed.

A complementary evaluation of the maximum attainable property P_∞ (either modulus or stress at break) could be calculated by the linear fitting of all experimental data P versus 1/DR according to the equation:

$$P = P_\infty - k_p 1/DR \tag{4.8}$$

where k_p is a proportionality constant taken into account the sensitivity of the property to the drawing [130]. Following this approach, predicted attainable strength of the compositions with 2 and 3% wt of the filler (1218 ± 56MPa for LDH-2, and 1205 ± 31MPa for LDH-3) were slightly higher than 1180 ± 50MPa of neat HDPE fiber, as presented in Table 4.10. Similar tendency was also observed in the case of the maximum attainable tensile modulus, i.e. 12.9 GPa for LDH-2 and 13.2 GPa for LDH-3, with respect to 11.8 GPa of neat HDPE.

Material	E^a_{MAX} [GPa]	$\sigma^a_{b\,MAX}$ [MPa]
HDPE	11.8±0.9	1180±50
LDH-0.5	11.1±0.8	1117±26
LDH-1	11.8±0.4	1029±18
LDH-2	12.9±0.2	1218±56
LDH-3	13.2±0.4	1205±31

Table 4.10. Maximum attainable theoretical values of elastic modulus and stress at break of neat HDPE and LDH nanocomposite fibers.

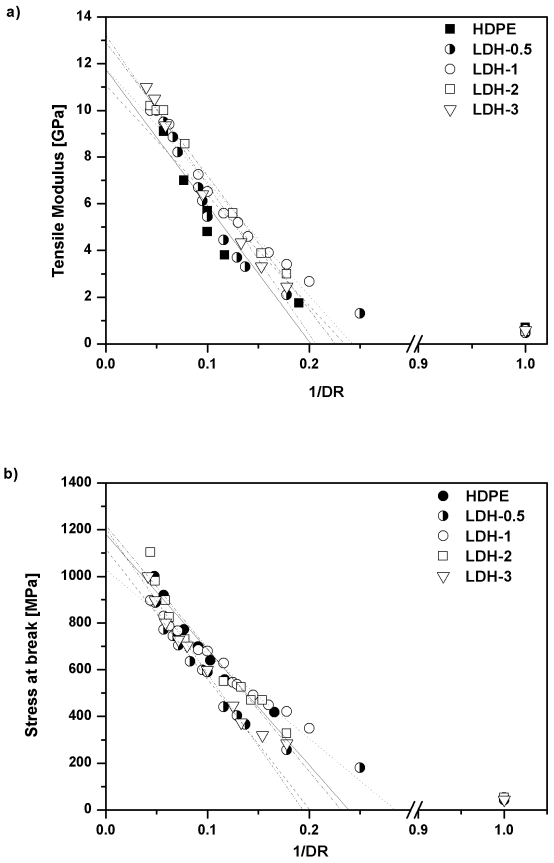

Figure 4.21. Attainable (a) elastic modulus and (b) stress at break for neat and nanofilled HDPE nanocomposite fibers.

4.2.8. DMTA analysis

DMTA analysis was performed for neat HDPE and nanocomposites fibers to obtain further information on mechanical properties and molecular motions. The dynamic mechanical properties as storage modulus and loss modulus were presented in Figure 4.22 a-d.

a)

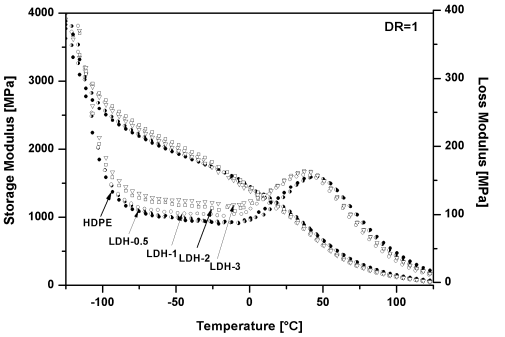
DR=1
Storage Modulus [MPa]
Loss Modulus [MPa]
Temperature [°C]
HDPE
LDH-0.5
LDH-1
LDH-2
LDH-3

b)

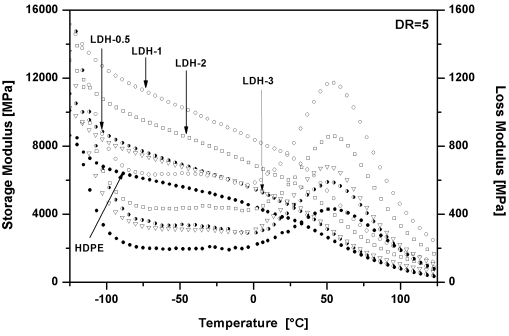
DR=5
Storage Modulus [MPa]
Loss Modulus [MPa]
Temperature [°C]
LDH-0.5
LDH-1
LDH-2
LDH-3
HDPE

c)

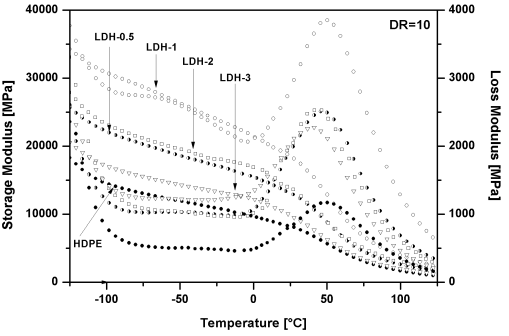
DR=10
Storage Modulus [MPa]
Loss Modulus [MPa]
Temperature [°C]
LDH-0.5
LDH-1
LDH-2
LDH-3
HDPE

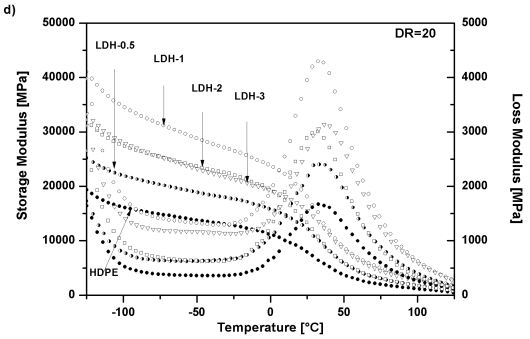

Figure 4.22. Effect of the composition of neat HDPE (●) and HDPE with different amount of hydrotalcite (◑- 0.5%, ○– 1%, □-2% and ▽– 3%) nanocomposites on the temperature dependence of the storage modulus and loss modulus for different draw ratio (a) DR=1, (b) DR=5, (c) DR=10 and (d) DR=20.

Storage modulus

As shown in Figure 4.22 a-d, the higher the drawing the higher the storage modulus in all ranges of tested temperatures. The expected increase in storage modulus (*E'*) was clearly observed when hydrotalcite was added. For as-spun fibers at low temperature range (from -100 °C up to 0 °C) slightly higher values of storage modulus were obtained for LDH-2 and LDH-3. It can be observed also that for the temperatures higher than 0°C the storage modulus was almost the same for all of the compositions. As it was expected, the molecular orientation induced by stretching results in a significant increase of storage modulus (E') values over the whole range of investigated temperatures. This phenomenon was well visible for higher draw ratio; the highest value was obtained for the LDH-1 and the lowest for neat HDPE. This was in agreement with mechanical properties of the corresponding samples where a maximum values in tensile as well as impact strength were also observed. Further increase of LDH content results in a decrease in storage modulus for sample containing 3 % wt. LDH. The behavior could be attributed to not homogenous dispersion and tendency to form agglomerates which affects weak physical interaction between the polymer molecules and LDH [95]. Moreover, XRD analysis reported previously confirmed that exfoliation did not occur in case of

composition with 3% wt. of the filler. In Fig. 4.23 variation of storage modulus of neat and nanofilled HDPE fibers with different draw ratios are reported.

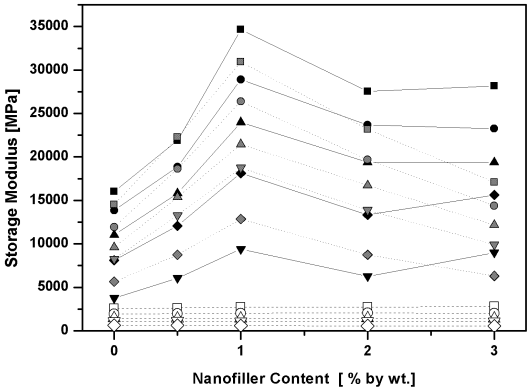

Figure 4.23. Variation of storage modulus of neat and nanofilled HDPE fibers at temperature-100°C, -50°C, 0°C, 25°C and 50°C with different draw ratio DR=1 – open symbol, DR=10 – grey symbol and DR=20 – black symbol.

It is evident from the plot that as the draw ratio increases the storage modulus increases. The incorporation of LDH into the HDPE matrix results in a remarkable increase in storage modulus over the entire investigated temperature range. It can be seen that modulus continued to increase at LDH content up to 1% wt. and then the modulus enhancement become dawdling for higher LDH content. Similar tendency in case of LDH were already observed and reported by other authors [95, 115]. Kontou and Niaounakis explain enhancement of modulus by considering consistence in the matrix of composite two parts; free part and interphase formed by the physical or chemical adsorption of the polyethylene molecules and/or crystallization on the filler's surface [90]. According to this assumption the increase in the hydrotalcite amount enlarges the interfacial area and results an increase in the volume of interphase.

In order to study the effect of the filler of composites, the intensity of the transition (S*) was calculated according to the equation 4.9 and reported in Table 4.11,

$$S^* = (E'_g - E'_r)/E'_r \quad (4.9)$$

where E'_g and E'_r are storage modulus in the glassy and in the rubbery state at -30°C and 90°C respectively [131].

Material	DR=1			DR=5			DR=10			DR=20		
	E'_g [MPa]	E'_r [MPa]	S*	E'_g [MPa	E'_r [MPa]	S*	E'_g [MPa]	E'_r [MPa]	S*	E'_g [MPa]	E'_r [MPa]	S*
HDPE	1769	200	7.8	5239	990	4.3	11129	2071	4.4	13231	1549	7.5
LDH-0.5	1784	200	7.9	6403	1058	5.1	17519	3136	4.6	18042	2176	7.3
LDH-1	1846	173	9.7	9621	2290	3.2	24517	4657	4.3	27246	3850	6.1
LDH-2	1882	173	9.9	8046	1811	3.4	18279	3440	4.3	22435	2176	9.3
LDH-3	1793	164	9.9	6403	1263	4.1	13563	2375	4.7	21808	3222	5.7

Table 4.11. Storage modulus at 1Hz and effect of LDH filler on the content of amorphous phase of HDPE-LDH fibers for different DR.

It is known that higher intensity of transition (*S**) refers to the higher mobility and content of amorphous phase. In case of as-spun material *S** values were increasing with nanofiller content, from 7.8 for neat HDPE up to 9.9 for LDH-3. It was related to the nucleation effect of LDH that leads to faster crystallization and the amorphous phase results with a bigger mobility. For the drawn fibers especially with DR=5 and 10 values were lower in comparison to as-spun material, while for DR=20 the *S** values again increased and reached values similar as for as-spun fibers. Moreover, in most of the cases values were lower than for neat HDPE. Only for LDH-0.5 for DR=5 and DR=10 and for LDH-2 for DR=10 and 20 values were higher. The addition of rigid phase cuts down the mobility of the polymer chain, which results in a lower value of the transition intensity especially observed for material with DR=5 and 10 [91]. Lower values obtained for drawn in comparison to as-spun material are related to limited mobility of the polymer chains after drawing process. During spinning the strong orientation of macromolecular chains occurs which causes orientation along the strain direction and enhancement of the crystallinity content. However, unexpected was fact that *S** factor decreased for DR=5 and after with further drawing starts to increased reaching similar values for DR=20 as for as-spun material. The explanation of this behavior might be the fact that drawing up to maximum (DR around 20) leads to fast crystallization, while the crystallinity content did not increase significantly in comparison to the compositions with DR=10 and DR=15 (described in the 4.2.6 paragraphs). This can be signal of an existence of an

amorphous phase that during drawing was oriented along the strain direction and has a higher molecular mobility. However, to better understand this behavior some more experiments has to be performed.

Loss modulus

The relaxation behaviour of polymer is strongly influenced by crystalline-amorphous state, such as crystallinity, lamellar thickness, and amorphous layer thickness [132]. The observed relaxations are identified as α, β and γ in order of decreasing temperature [91]. The α-relaxation is observed in the range between room and melting temperature, the β is appearing between 220 K and 300 K and the γ is in the range 130-180 K. The α relaxation has been interpreted as related to the molecular motion of the crystalline phase and was observed only for compositions with crystallinity content more that 55% [133]. On the α relaxation the parameters as HDPE content, crystallinity, crystalline perfection, and macro- and micro-structure of the crystalline phase have to be taken into account [134]. In Figure 4.22.a-d loss moduli versus temperature for different draw ratio are reported.

In the loss modulus curve for neat HDPE only the α-transition located at around 40ºC was observed. For DR = 1 peak of α-relaxation has the highest intensity for LDH-2 and LDH-3. As it is already proved by other researchers, higher crystallinity of the sample results in a higher α - peak respectively [91, 135]. It can be also observed that with the nanofiller amount α- peak was shifted to the lower temperature range. For example for neat HDPE peak occurred at 43 °C while for LDH-3 was located at 38 °C. For drawn material that maximum of α - relaxation are shifted to the higher temperature values in comparison to the as - spun material, for neat as - spun HDPE peak was observed at 43 °C wile for DR = 10 is at 46 °C, and similar as for as - spun material with the nanofiller amount the temperature was shifted to the slightly lower values. This behavior could be related to the fact that presence of LDH nanoparticles caused heterogeneous nucleation and this affected formation of less perfect crystals. The intensity of the peak also increased with the nanofiller presence, the highest intensity was obtained for the compositions LDH-1 and LDH-2. These results are due to the sufficient LDH layer exfoliation rate in the

HDPE matrix when the nanofiller content was optimal. Higher intensity observed for drawn material was related to the formation of crystalline phase induced during drawing. Moreover, after drawing LDH exhibited a strong interfacial interaction with the matrix, thereby limiting the molecular freedom of movement [95].

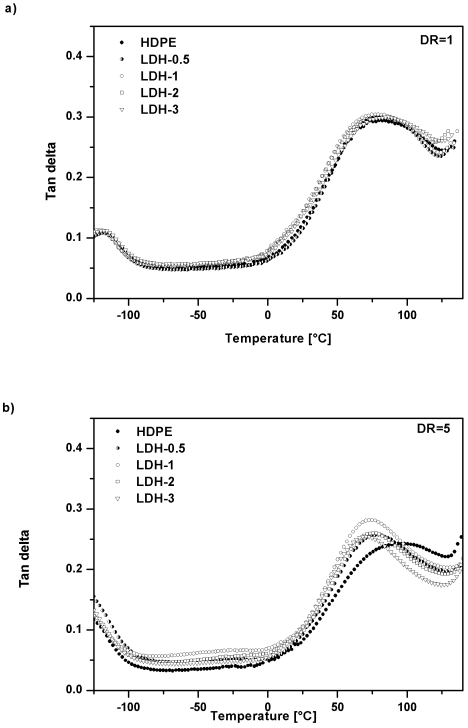

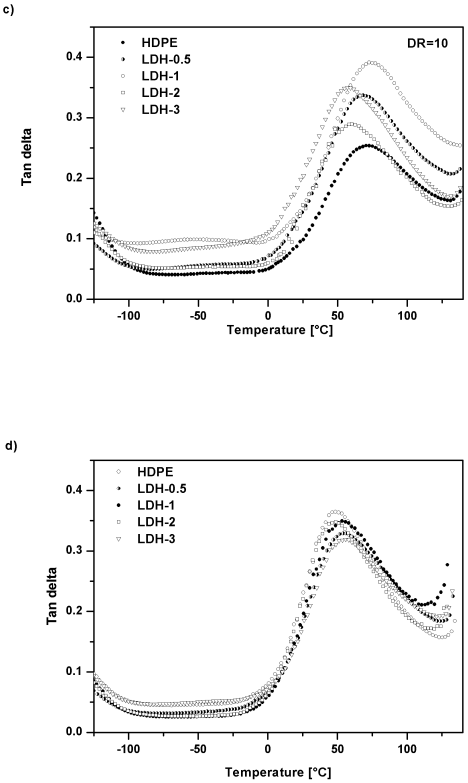

Figure 4.24. Effect of the composition of neat HDPE (●) and HDPE with different amount of hydrotalcite (◑- 0.5%, ○– 1%, □-2% and ▽– 3%) nanocomposites on the temperature dependence of the tan delta for different draw ratio (a) DR=1, (b) DR=5, (c) DR=10 and (d) DR=20.

Tan delta

The viscoelastic behavior of HDPE in the temperature range of the T_g is mainly related to the amorphous phase. Therefore, factors as amount of HDPE, amorphous phase content, and mobility of the polymer chains in both phases strongly affects the Tan δ value [134]. Results of tan delta values were depicted in Figure 4.24a-d). In case of our material T_g was absent in as – spun fibers while for DR = 5 and 10 the β - relaxation appeared between -80 °C and 0 °C as a shoulder of LDH-1. However,

for DR=20 peak related to β-transition was again not visible. Some authors relate the β relaxation to the movement of the chain units in the interfacial region [91, 135], others with relaxation of short chain branches or the amorphous phase [136]. The enhancement of β-relaxation in our case can be attributed to the restricted segmental motions at the organic-inorganic interface in the neighborhood of intercalated compositions [34]. The fact that peak was very broad according to the Diez-Gutiérreza et al. [137] can be due to inhomogeneity of the amorphous phase. The nucleation effect of LDH which accelerates the crystallization of HDPE composites more intensive during drawing process is creating a more inhomogeneous amorphous phase. However, the appearance of β-transition for LDH-1 is an indication of the good interfacial adhesion between matrix and nanofiller [138].

Sumita et al. [139] utilized the energy dissipation in dynamic mechanical analysis measurements to identify the effective volume fraction of the dispersed phase, φe, which is composed of the volume of filler plus that of the "immobilized matrix" associated with the interface. A parameter *B* is used to describe the relative value of the effective volume per single particle, as shown in the following equation:

$$\frac{E_C''}{E_M''} = (1-\varphi_e)^{-1} = \left(1-\varphi_f B\right)^{-1} \quad (4.10)$$

where E_C'' and E_M'' represent the loss moduli of the composites and the neat polymer matrix.

To characterize the interphase thickness, the effective particle volume fraction (φ_e) and effective volume per single particle (*B*-parameters) were calculated and reported in Table 4.12. and results were depicted in Fig 4.25.a and b.

Material	E'' peak [MPa]	E''_C/E''_M	φ_f [vol]	φ_f [vol]	B
DR=1					
HDPE	154.6	1.00	-	-	-
LDH-0.5	154.8	1.00	0.004	0.001	0.36
LDH-1	160.0	1.03	0.007	0.034	4.73
LDH-2	164.1	1.06	0.014	0.058	4.05
LDH-3	164.1	1.06	0.022	0.058	2.70
DR=5					
HDPE	432.5	1.00	-	-	-
LDH-0.5	584.7	1.35	0.004	0.260	73.10
LDH-1	1174.9	2.72	0.007	0.632	88.60
LDH-2	858.5	1.98	0.014	0.496	34.70
LDH-3	682.0	1.58	0.022	0.366	17.00
DR=10					
HDPE	1166.0	1.00	-	-	-
LDH-0.5	2539.5	2.17	0.004	0.541	151.90
LDH-1	3847.8	3.30	0.007	0.697	97.73
LDH-2	2565.2	2.20	0.014	0.545	38.13
LDH-3	2285.8	1.96	0.022	0.489	22.76
DR=20					
HDPE	1676	1.00	-	-	-
LDH-0.5	2400	1.43	0.004	0.301	84.72
LDH-1	4300	2.56	0.007	0.610	85.56
LDH-2	3004	1.79	0.014	0.442	30.90
LDH-3	3121	1.86	0.022	0.463	21.51

Table 4.12. DMTA data for the β-relaxation peak of neat and nanofilled HDPE fibers according to the model proposed by Sumita et al. [139].

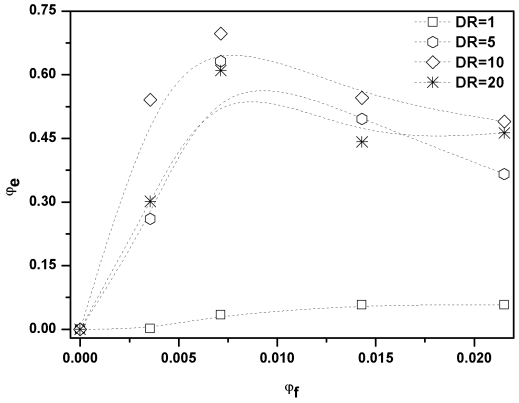

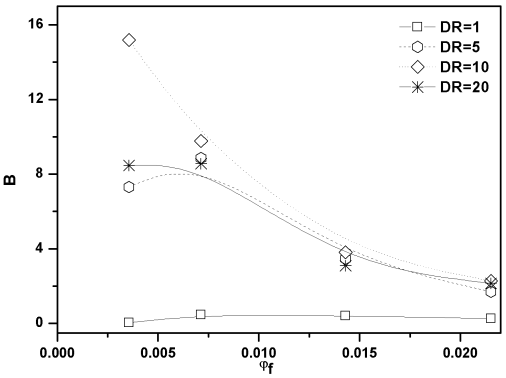

Figure 4.25. Effective particulate volume fraction (φ_f) and effective particulate volume per single particle (B) of HDPE-LDH nanocomposites as a function of LDH volume fraction.

It can be observed that for DR=1, φ_e values did not change with volume fraction of the filler, while for drawn material increased with the filler content up to about 0.7% vol, and then with further addition of LDH particles dramatically decreased. Similar behavior was observed in case of B parameter. According to Sumita [139], unchanged φ_e values with the increasing amount of the filler, means that the thickness of the physically absorbed matrix layer on the surface of the nanofiller is limited due to the agglomeration of the nanoparticles. In addition, decreasing B-parameters suggest that the extent of the agglomeration of the particles also increases with the filler content. It should be also noted that the increase of DR of the fibers results in an increase in both φ_e and B-parameters for the φ_f up to 0.7% vol, what is related to the increase in interphase thickness. It can be concluded that lower filler contents are preferable due to the better dispersion of the nanocomposites.

4.2.9. Multi Frequency DMTA analysis

In order to valuate dynamic behaviour over an extended frequency range, multi-frequency DMTA tests were performed on high dawn neat and nanofiller fibers (DR = 20). The Fig. 4.26 shows the storage modulus and loss modulus with indications of

α-transition as a function of temperature at five different frequencies for neat and nanofilled HDPE fibers.

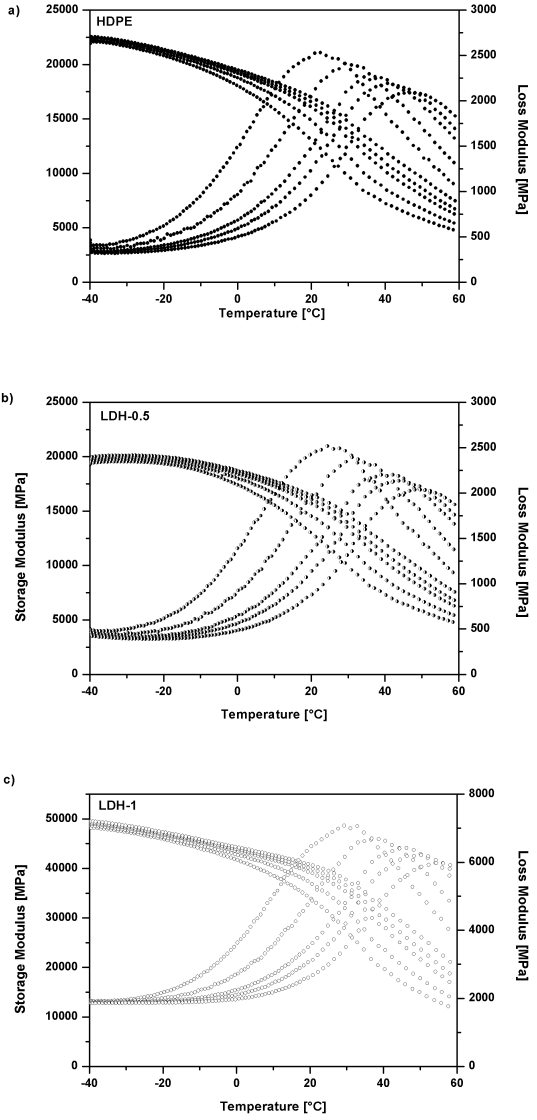

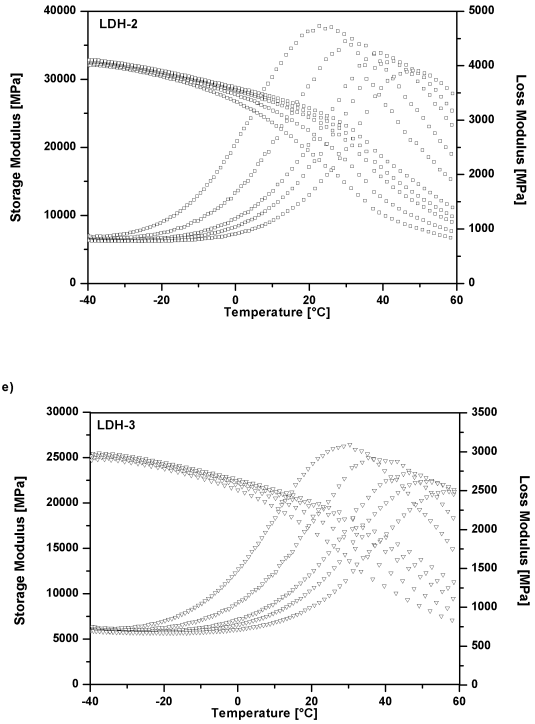

Figure 4.26. Selected storage modulus and loss modulus from DMTA multifrequency curves of neat and HDPE nanocomposite with different nanofiller amount (a) HDPE, (b) LDH-0.5, (c) LDH-1, (d) LDH-2 and (e) LDH-3.

Generally, in DMTA curves if frequency increases, decrease of the slope of the storage modulus curve in the region of the transition can be observed [140]. A distinct maximum in loss modulus was observed, which shifted to higher temperatures with increasing frequency. The different maximum values of the loss modulus at the peak temperature are due to the decrease of the complex modulus in that temperature range [133].

The activation energies of the α-relaxation were determined from the maximum of loss modulus (E'') at constant frequency (Tab. 4.13.).

Material	HDPE		LDH-0.5		LDH-1		LDH-2		LDH-3	
	Maximum of loss modulus		Maximum of loss modulus		Maximum of loss modulus		Maximum of loss modulus		Maximum of loss modulus	
	[MPa]	[°C]	[MPa]	[°C]	[MPa]	[°C]	[MPa]	[°C]	[MPa]	[°C]
0.3 Hz	2535	22.4	2511	24.6	7100	31.1	4740	24.2	3099	30.3
1 Hz	2418	29.1	2389	30.9	6674	37.7	4489	31.7	2921	38.4
3 Hz	2273	35.2	2198	38.9	6412	44.4	4242	37.5	2722	46.4
5 Hz	2189	40.0	2131	43.4	6233	50.3	1090	41.5	2625	51.2
10 Hz	2092	45.6	2033	48.6	5971	54.6	3923	47.1	2487	58.5

Table 4.13. The effect of LDH on the α- transition temperature measured at the maximum of the α-peak at various frequencies of HDPE and its nanocomposite at DR=20.

In the Figure 4.27 Arrhenius plot of α-relaxation was reported, and obtained energies values were summarized in Table 4.14. The apparent activation energy was calculated using the Arrhenius equation:

$$\frac{\partial \ln f}{\partial\left(\frac{1}{T}\right)} = \frac{-E_a}{R} \tag{4.11}$$

by taking integration of Eq. 4.12:

$$\ln f = lnf_0 - \left(\frac{E_a}{RT}\right) \tag{4.12}$$

where *f* is the frequency, *T* is α-relaxation temperature measured in the peak-top of the loss modulus curve, *R* is the gas constant and E_a is the activation energy [141].

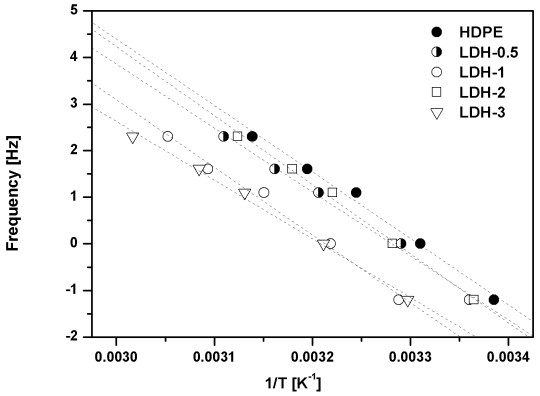

Figure 4.27. Arrhenius plot of α-relaxation of the maximum frequency in loss modulus of neat and nanofilled HDPE at DR=20.

Material	Ln f_0 [Hz]	E_a (α) [kJ/mol]	E_a [kJ/mol]
HDPE	47.2±2.4	118.7±6.2	84.0±1.4
LDH-0.5	45.1±2.0	114.2±4.7	70.3±0.3
LDH-1	46.7±2.6	120.8±6.9	70.7±0.6
LDH-2	48.7±2.0	123.3±4.6	73.3±0.2
LDH-3	40.4±1.6	104.8±4.3	83.5±0.3

Table 4.14. Activation energies of α-relaxation of HDPE and its nanocomposites with LDH at DR=20.

The obtained values of α-relaxation activation energy are in the range 104-123 kJ/mol and they are similar to the one obtained by other authors. For example Nitta and Tanaka [142] determined the activation energy for linear and SCB-polyethylenes between 100 and 120 kJ/mol. Stadler found activation energies for slowly cooled HDPE products in the range 110-120 kJ/mol, while the quenched ones reached a bit higher values 120-130 kJ/mol [133]. In case of our material interesting was fact that higher values in comparison to neat HDPE were obtained for the compositions with 1 and 2% wt. of filler, while for 0.5 and 3% wt. of LDH activation energies were lower. Stadler in case of slowly cooled and quenched material found the most possible reason of higher activation energies values in the lamellae organization [133]. In our case all material was quenched, however as it was observed during SEM (TEM) analysis in case of low nanofiller content better distribution of the filler was obtained. Better distribution will affect higher crystallinity content (X_c for LDH-1 equal 77% in comparison to 74% for neat HDPE) and this perhaps higher energy barrier, while in case of low filler distribution less perfect crystals are obtained what affects lower crystallinity content and lower energy barrier.

In the Fig. 4.28 the resulting master curves obtained on the basis of a frequency - temperature superposition principle at a temperature of 30 °C were reported. Storage modulus values for nanofilled fibers were higher than those of unfilled fibers, and the best properties were obtained for LDH-1. From the correspondent plot of the shift factors as a function of temperature reported on the Fig. 4.29 an Arrhenius equation can be used in order to obtain activation energy values (E_a) (Table 4.14.). It was found that activation energy for HDPE fibers with LDH nanoparticles, for LDH-0.5 E_a=70.3±0.3 kJ·mol^{-1}, LDH-1 E_a = 70.7±0.6 kJ·mol^{-1}, LDH-2 E_a=73.3±0.2

kJ·mol^{-1}, were lower than that for neat HDPE (E_a = 84.0±1.4 kJ·mol^{-1}). Only for composition with 3% wt. of nanofiller activation energy values was equal E_a=83.5±0.3 kJ·mol^{-1} and was very similar to neat HDPE fibers. According to the Hoffman theory, lower activation energy for the HDPE nanocomposites than neat HDPE is related to the heterogeneous nucleation of LDH particles. However, when the LDH loading was higher (≥3% wt.) energies values were very similar to the one obtained for neat HDPE. Similar behaviour was also observed for HDPE/$BaSO_4$ nanocomposites [114]. This behavior can be related with the fact that the effect of the addition of $BaSO_4$ nanoparticles into HDPE matrix would increase with the increase of aspect ratio or decrease of particle size because of increased surface area. In this case even stronger interfacial interaction between the nanoparticles and matrix, resulting in more limitation on the mobility of polymer chains or segments imposed from nanoparticle.

In DMTA analysis an increase in storage modulus indicates improved interfacial adhesion which hinders further molecular motion, leading to a stiffer and tougher material, in our case the best results in these measurements were obtained for the composition with 1% wt. of the filler.

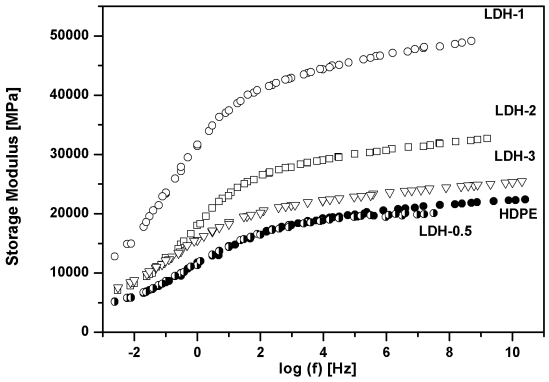

Figure 4.28. Storage modulus (*E'*) master curves of neat and nanofilled HDPE fibers with DR=20 from DMTA multi-frequency tests (T_0=30°C)

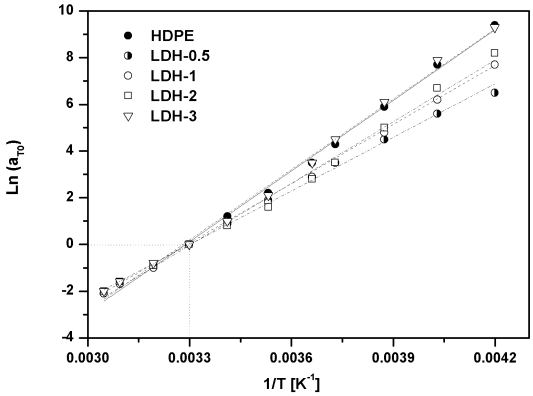

Figure 4.29. Shift factor for the construction of the E' master curves with the linear fitting in according to Arrhenius equation of neat and nanofilled HDPE fibers with DR=20 from DMTA multi-frequency tests (T_0=30°C)

4.2.10 Creep tests

Creep modeling and analysis is important from a fundamental and application perspective, especially where the polymer material must sustain loads for long time [79]. There have been several attempts to enhance the creep resistance of HDPE via crosslinking, copolymerization, and the use of additives and fillers. Several mechanical models, representing response of a viscoelastic material under creep condition have been developed. Among various models, power law equation and Burgers models were applied for our results.

Burgers model derives from the combination in series of two units Maxwell and Kelvin, as described by the constitutive law reported in Equation 4.13 and Figure 4.30,

$$D(t) = \frac{1}{E_M} + \frac{t}{\eta_M} + \frac{1}{E_K}\left(1 - e^{\frac{E_K t}{\eta_K}}\right) \qquad (4.13)$$

where E_M, η_M are elastic and viscous component of Maxwell model and E_K, η_K are elastic and viscous component of Kelvin model [79].

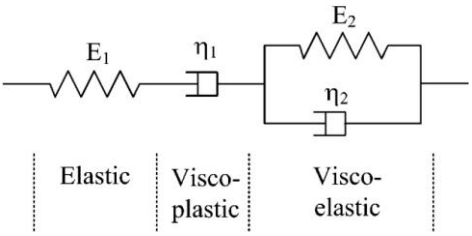

Figure 4.30 Schematic diagram of Burger model.

Besides Burgers model, an empirical model called Findley power law model is also frequently used to describe the creep behaviour of viscoelastic materials, and can be expressed by the equation:

$$D(t) = D_E + D_{VE}t^m \quad (4.14)$$

where D_E is elastic and D_{VE} viscous component of model [143]. Comparing with Burger model, Findley power law is more effective in predicting the creep behaviour of such a kind of materials, which has no significant transition from unstable to stable creep stag, and the creep rate at sufficient long time scale reaches asymptotically zero [144]. The creep tests were carried out in order to determine the deformation behavior of the material under a constant load. In this experiment a constant stress σ_0=3MPa was applied to a sample and the strain was monitored as a function of time. In Figure 4.31 creep compliance curves of HDPE and LDH nanocomposites at different draw ratio are compared and the fitted data according to the Burgers and Findley model are summarized in Table 4.15 and 4.16.

a)

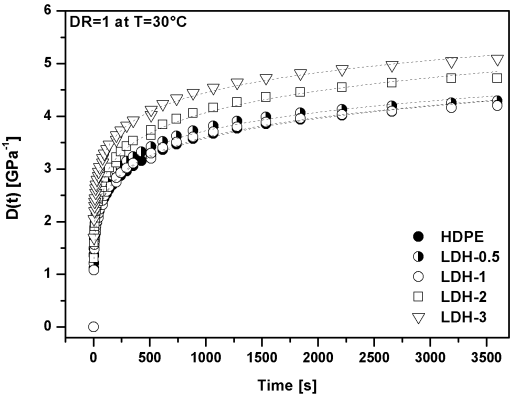
DR=1 at T=30°C
D(t) [GPa^{-1}]
Time [s]
HDPE
LDH-0.5
LDH-1
LDH-2
LDH-3

b)

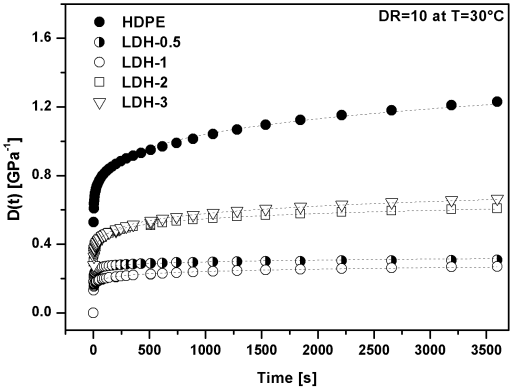
DR=10 at T=30°C
D(t) [GPa^{-1}]
Time [s]
HDPE
LDH-0.5
LDH-1
LDH-2
LDH-3

c)

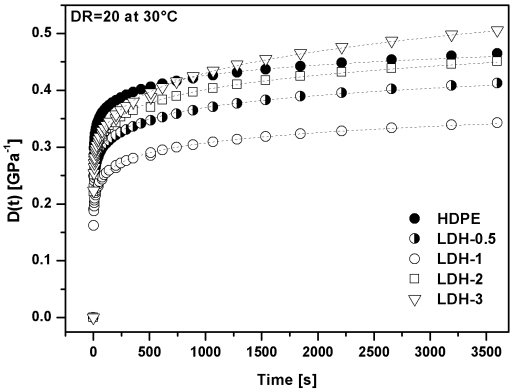

Figure 4.31. Creep compliance curves of neat and nanofilled HDPE fibers (at σ_0=3MPa at 30°C) (a) DR=1, (b) DR=10 and (c) DR=20.

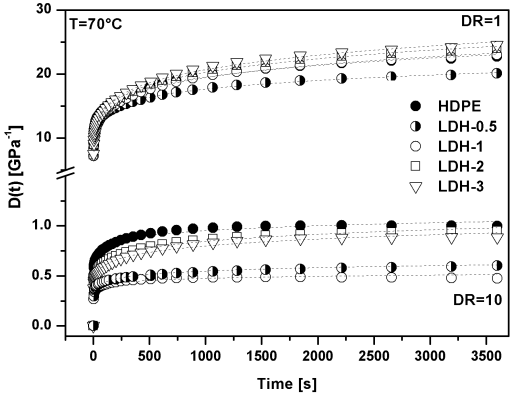

Figure 4.32. Creep compliance curves of neat and nanofilled HDPE fibers (at σ_0=3MPa at 70°C) for DR=1 and DR=10.

Material	E_M [MPa]	η_M [GPa·s]	E_K [MPa]	η_K [GPa·s]	R^2
DR=1 at 30°C					
HDPE	0.86±0.03	2.42±0.61	0.54±0.07	0.36±0.030	0.928
LDH-0.5	0.82±0.23	2.51±0.65	0.52±0.06	0.29±0.061	0.920
LDH-1	0.88±0.28	2.52±0.64	0.52±0.07	0.35±0.063	0.930
LDH-2	0.58±0.11	2.77±0.41	0.55±0.10	0.65±0.052	0.978
LDH-3	0.46±0.19	2.77±0.42	0.55±0.10	0.60±0.110	0.973
DR=10 at 30°C					
HDPE	1.60±0.40	6.66±1.24	7.04±1.20	4.70±0.73	0.910
LDH-0.5	16.6±0.04	50.0±5.82	72.2±11.2	3.82±0.80	0.930
LDH-1	14.1±0.02	33.3±7.61	78.3±10.0	4.50±0.65	0.920
LDH-2	2.88±1.10	33.3±3.93	67.1±11.5	5.05±1.00	0.961
LDH-3	2.97±0.46	20.0±4.76	57.8±9.10	4.97±1.50	0.966
DR=20 at 30°C					
HDPE	3.90±1.41	16.4±1.22	7.04±1.20	7.00±1.50	0.930
LDH-0.5	4.40±0.90	38.4±2.61	72.2±11.2	6.23±1.80	0.960
LDH-1	5.26±1.11	50.0±2.27	78.3±10.0	9.30±2.30	0.970
LDH-2	3.94±0.83	37.0±2.92	67.1±11.5	8.42±0.45	0.970
LDH-3	3.77±0.73	26.3±3.43	57.8±9.10	10.0±1.50	0.973

Material	E_M [MPa]	η_M [GPa·s]	E_K [MPa]	η_K [GPa·s]	R^2
DR=1 at 70°C					
HDPE	0.68±0.02	0.33±0.03	0.077±0.01	0.33±0.06	0.875
LDH-0.5	0.73±0.03	0.42±0.04	0.082±0.02	0.34±0.06	0.888
LDH-1	0.64±0.02	0.39±0.03	0.110±0.07	0.38±0.05	0.898
LDH-2	0.60±0.03	0.39±0.02	0.105±0.05	0.51±0.02	0.899
LDH-3	0.58±0.04	0.40±0.02	0.103±0.06	0.67±0.07	0.887
DR=10 at 70°C					
HDPE	1.28±0.17	10.64±2.45	1.45±0.80	6.34±0.11	0.825
LDH-0.5	10.5±1.80	9.10±3.20	18.4.±0.20	9.23±4.20	0.840
LDH-1	10.2±2.15	12.20±4.10	34.5±3.80	18.3±3.50	0.830
LDH-2	1.05±0.14	11.10±2.30	18.4±4.50	9.61±3.20	0.840
LDH-3	1.39±0.16	16.95±4.15	28.5±2.40	12.2±5.10	0.840

Table 4.15 Fitting of the creep data of Figure 4.31 and 4.32 according to the Burgers model

Material	D_E [GPa^{-1}]	D_{VE} [GPa^{-1}]	m	R^2
DR=1 at 30°C				
HDPE	1.78±0.31	0.94±0.03	0.098±0.01	0.998
LDH-0.5	3.65±0.70	0.98±0.06	0.067±0.01	0.998
LDH-1	2.81±0.66	0.85±0.06	0.081±0.01	0.997
LDH-2	2.66±0.61	1.05±0.05	0.086±0.01	0.997
LDH-3	3.43±0.85	1.49±0.10	0.068±0.01	0.997
DR=10 at 30°C				
HDPE	0.63±0.04	0.37±0.03	0.170±0.01	0.994
LDH-0.5	0.21±0.02	0.04±0.01	0.002±0.04	0.950
LDH-1	0.18±0.06	0.02±0.06	0.065±0.02	0.992
LDH-2	0.37±0.02	0.10±0.01	0.048±0.01	0.995
LDH-3	0.43±0.05	0.12±0.05	0.107±0.01	0995
DR=20 at 30°C				
HDPE	0.37±0.12	0.12±0.05	0.003±0.001	0.994
LDH-0.5	0.32±0.19	0.03±0.18	0.037±0.01	0.997
LDH-1	0.15±0.08	0.07±0.08	0.052±0.01	0.996
LDH-2	0.20±0.04	0.18±0.04	0.092±0.01	0.996
LDH-3	0.25±0.01	0.15±0.01	0.187±0.01	0.996

Material	D_E [GPa^{-1}]	D_{VE} [GPa^{-1}]	m	R^2
DR=1 at 70°C				
HDPE	4.60±0.75	4.77±0.61	0.16±0.01	0.996
LDH-0.5	1.40±0.13	7.20±1.21	0.11±0.01	0.996
LDH-1	0.89±0.10	8.00±0.90	0.13±0.01	0.998
LDH-2	1.30±0.70	8.40±0.94	0.13±0.01	0.997
LDH-3	0.84±0.15	7.96±0.90	0.14±0.01	0.997
DR=10 at 70°C				
HDPE	3.5±0.37	3.55±3.70	0.02±0.002	0.986
LDH-0.5	8.71±0.13	8.40±0.13	0.22±0.04	0.975
LDH-1	9.91±1.20	9.94±1.20	0.29±0.02	0.957
LDH-2	5.25±1.50	3.15±0.63	0.12±0.01	0.992
LDH-3	7.41±1.80	3.72±1.04	0.12±0.02	0987

Table 4.16 Fitting of the creep data of Figure 4.31 and 4.32 according to the Findlay power law equation.

For DR=1 the creep compliance for compositions with low amount of nanofiller (0.5-1 % wt.) was practically equal to that of the neat HDPE, while for compositions with 2 and 3 % wt. of LDH the creep compliance was higher. Interesting creep behavior was observed in case of drawn material. It is immediately evident that the incorporation of hydrotalcite leads to a reduction of the total creep compliance. Better creep stability was observed for the compositions with low nanofiller amount (0.5 and 1 % wt.) in comparison to fibers with 2 and 3 % wt. of LDH. It has been proven by other authors [145-147] that an introduction of layered silicates reduces the creep compliance, however the level of intercalation and/or exfoliation is a critical parameter determining the creep behaviour of the nanocomposites [143]. Analogous effects on the creep behaviour of polymeric nanocomposites observed earlier were attributed to a restriction of the chain mobility due to the dispersion of the nanofiller at the nanoscale [133, 148]. As already reported in quasi-static tensile tests, the reinforcing effect due to the presence of the nanoparticles can be explained considering the polymer-filler surface physical interaction due to the presence of hydrogen bonds at the interface. In case of our material drawing process caused better dispersion and orientation of the nanofiller. In case of low nanofiller content (0.5 and 1% wt.) good dispersion after drawing process, while in case of high nanofiller content some aggregates were observed. This behaviour will cause the reduction in case of nanocomposition with low and enhancement in case of high nanofiller content fibers of creep compliance. Moreover, it can be seen that with further drawing (DR=20) the reduction of creep compliance is less intensive. This

may be related to the fact that the maximum surface physical interaction was already obtained and further drawing process will not cause any significant improvement.

The temperature dependence of the tensile creep response of HDPE based nanocomposite fibers will be now considered. In Figure 4.32 creep compliance of HDPE-LDH nanocomposites fibers at temperature 70°C, under an applied stress of 3MPa during 60 min were reported. It can be noted that the deformation behavior of the materials is strongly dependent on the temperature. Moreover, as before for 30°C, at 70°C the introduction of hydrotalcite leads to lowering of the creep compliance, especially at DR=10. As it was already observed before, the best creep stability was obtained for the compositions with low nanofiller content (0.5-1% wt.). If the data obtained in both temperatures condition will be compared we can see that for DR=1 much higher creep compliance at 70°C was observed. However for DR=10 the values were very similar for both testing temperatures, and only slightly higher creep compliance was obtained at 70°C.

Creep behavior at different temperatures of HDPE and hydrotalcite nanocomposites can be analyzed considering viscoelastic mechanical models available for thermoplastic materials. Among all of them, the most well-known are Burger (or four parameter) viscoelastic model [149] and Findley power law [150], both were used in this study to evaluate the static and dynamic creep behaviors of neat HDPE and HDPE-LDH composite fibers. As it was already mentioned before in Figure 4.31 and Figure 4.32 creep compliance curves of nanocomposite fibers at different temperatures were compared with the fitted data according to the Burgers model (represented by dash line), and in Table 4.15 parameters derived from the fitting are summarized. As it could be easily predicted, the increase in the draw ratio produces an increase in elastic (E_K, E_M) and viscous components (η_K η_M). Comparing fitting parameter of the neat and nanofilled HDPE fibers, the conclusion is that all the parameters elastic and viscous for drawn material are higher than obtained for neat HDPE, in particular much higher values were observed for viscous component of Maxwell element. Similar behavior already reported in case of polyamide fibers was explained considering fact that η_M parameter rules the deformation behaviour of the material for long creep time what gives more effective stabilizing effect provide by

hydrotalcite at long testing time [151]. With the temperature, as reported in Table 4.15 the viscous (η_K, η_M) and elastic (E_K, E_M) parameters of Burgers model decreases, but the most important conclusion is that the enhancement of the creep resistance of the material can be related to a substantial increase of the elastic (especially E_K) and viscous components (both η_K and η_M) of the model. The effectiveness of the viscoelastic models in interpreting creep data of nanofilled samples, adopting the parameters analysis to interpret the structure-property relationship were recently reported also by Wang and Zhao [144].

In Table 4.16 both the elastic and viscoelastic components obtained from the fitting according to the Findlay equation were summarized. It can be observed that for as-spun material both components were higher in comparison to neat HDPE while after drawing process when good dispersion and better filler-matrix interphase was obtained the lower values were observed in comparison to the one obtained for neat HDPE.

It can be conclude that creep stability can be significantly improved by the addition of hydrotalcite nanoparticles. Conducted experiments evidences that small well-dispersed amount of the filler have positive reinforcing effects. However, the effect was not directly proportional to the filler content. The existence of optimal filler concentration was observed (0.5-1% wt.) while after a certain amount, nanofillers tends to form aggregates in the matrix that would causes a deterioration of the properties like for example creep.

4.2.11 Summary HDPE-LDH fibers

High density polyethylene (HDPE) and its composites with 0.5 - 3 % wt. of organically modified hydrotalcite (LDH) were compounded and spun by combining melt-extrusion and hot-drawing at temperature between 100°C and 140°C. The most suitable drawing temperature was found to be 125°C for both the neat HDPE and nanocomposites. Fibers could be easily drawn at high draw ratios (up to 20) reaching linear density up of 9 tex and tensile modulus of about 10 GPa. In general, spinnability and drawability of the nanofilled polyethylene were found analogous to those of the neat HDPE.

The incorporation of LDH increased the thermal stability of composite fibers in comparison with HDPE. Moreover, crystallization kinetics indicates a nucleation effect of LDH on the HDPE matrix and evidences slightly enhanced temperature of the transition between Regimes II/III at 119°C for the composites containing 1-2 % by wt of LDH. Morphology and XRD analysis revealed a high degree of exfoliation of LDH in fibers containing 1-2 % by wt. of nanoclay, which was particularly evident after drawing. Consequently, tensile modulus of nanofilled fibers rose with the LDH content and drawing ratio. Tensile stress at break and strain at break of composite fibers approximately corresponded to those of the neat HDPE. Using the experimental data, a maximum value of elastic modulus of about 12.9-13.2 GPa was obtained through stiffness extrapolation of the nanofilled fibers containing 2-3% of LDH (with respect to 11.8 GPa found for the neat HDPE). These beneficial effects can be attributed to a good dispersion and alignment of hydrotalcite particles, which promote molecular orientation and crystallization in the HDPE matrix and also act as thermal barriers. DMTA tests evidenced stiffening effect observed as higher storage modulus for the all compositions with hydrotalcite particles especially at higher draw ratio. The nucleating effect of the LDH leads to faster crystallization and the higher mobility of amorphous phase. The decrease of α-relaxation activation energy in HDPE composites fibers with respect to neat HDPE supports this interpretation. A future confirmation comes from the fact that the intensity of transition (S^*) also increases with LDH content, what is related to the higher mobility of amorphous phase. Higher master curve of storage modulus at 30°C in the range of frequency 0.3 – 1 – 5 - 10 Hz was obtained. The decrease of activation energy in the HDPE-LDH nanocomposites in comparison to neat HDPE is related to the heterogeneous nucleation process caused by hydrotalcite nanoparticles.

Creep tests evidenced a certain reduction of the creep compliance with respect to the neat HDPE fibers over the whole range of investigated draw ratio and temperatures. Based on the studies it can be concluded that LDH nanoparticles at higher draw ration effectively reinforce HDPE.

Considering the thermo-mechanical characterization of the several prepared HDPE-LDH nanocomposites fibers, the nanocomposite of HDPE with 1% wt. of LDH showed the best balanced properties.

Chapter V

5.1. PP-fumed silica nanocomposite plates

Polypropylene (Moplen HP500, melt flow rate 1.8g/10min at 230 °C and 2.16, density at 23 °C=0.9g/cm^3) was used in the form of pellets. Fumed silica (FS) nanoparticles Aerosil®AR974 and AR®805 were kindly supplied by Evonik (Essen, Germany). Both type of nanosilica are hydrophobic and are different for surface area and for the surface treatment. Aerosil®AR974 has a surface treated with dimethyldichlorosilane and specific surface area 170m^2·g^{-1}, while Aerosil®AR805 was treated with octylsilane and has specific surface area equal 150m^2·g^{-1}. Before the processing, fumed nanosilica powders were dried for 24h at 80°C in a vacuum oven. The volume fraction of loading was varied between 0.25 - 2% vol. The filler volume percentage was determined by the weight fraction through Equation 5.1:

$$V_p = \frac{W_p \frac{\rho_m}{\rho_p}}{W_m + W_p \frac{\rho_m}{\rho_p}} \quad (5.1)$$

where V_p is the filler volume fraction, W_m and W_p are respectively the matrix and the filler weight fraction, ρ_m and ρ_p represent the densities of the matrix and of the filler. Nanocomposites were designated as silica abbreviation (AR974 and AR805) and the filler content. As an example, AR974-2 indicates a nanocomposite sample filled with 2 % vol. of fumed silica Aerosili®AR974, while AR805-1 is an abbreviation of nanocomposite sample filled with 1% vol. of silica Aerosil®AR805. To evaluate the influence of compatibilizer on the mechanical properties, compositions with 0.5 and 1% vol. of Fusabond F613 (designed as PPgMA) with and without 0.5% vol. of fumed nanosilica AR974 were performed and tested. Neat polypropylene will be designed as PP.

5.1.1. Morphology

As reported in Table 5.1, the investigated formulations are a combination of polypropylene with the two fumed nanosilica types AR974 and AR805.

Sample	PP [%]	AR974/AR805 [%]	MFI [dg/10min]	Shore D [Hs]
PP	100	0.0	2.71±0.16	70.7±0.5
AR974/805-0.5	99.5	0.5	2.90±0.17 / 2.76±0.14	71.5±0.5 / 71.5±0.5
AR974/805-1	99.0	1.0	3.49±0.15 / 3.21±0.02	72.0±1.0 / 72.0±1.0
AR974/805-1.5	98.5	1.5	3.67±0.21 / 3.40±0.14	72.5±1.0 / 72.5±0.5
AR974/805-2	98.0	2.0	4.58±0.31 / 4.47±0.02	73.5±0.5 / 73.0±1.0

Table 5.1. Designation and formulation of PP nanocomposites (in percentage by vol.).Dependence of melt flow (230°C, 2.16 Kg), hardness Shore D on the composition.

It should be noted the MFI values increased with the percentage of silica in the polymer matrix, with an almost linear dependence on the PP-AR974/805 composition (Table 5.1). Similar results were also observed in case of hardness Shore D. The hardness was increasing with nanofiller content and reached the highest values for AR974-2 (73.5 Hs) with respect to 70.7 Hs for polypropylene what evidence the effect of nanofiller, as reported in Table 5.1.

The effect of compounding and the quality of silica dispersion into PP matrix was evaluated of cry-fractured surfaces of PP-AR974/805 nanocomposites by ESEM analysis and results are reported in Figure 5.1a-d.

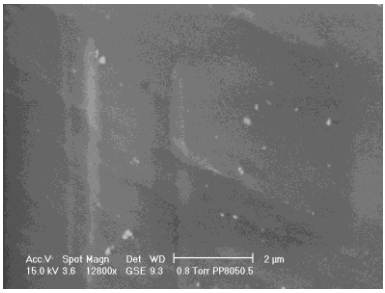

Fig. 5.1.a ESEM micrograph of AR805-0.5.

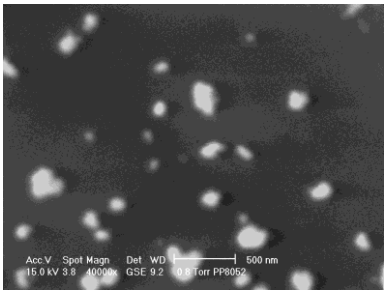

Fig. 5.1.b ESEM micrograph of AR805-2.

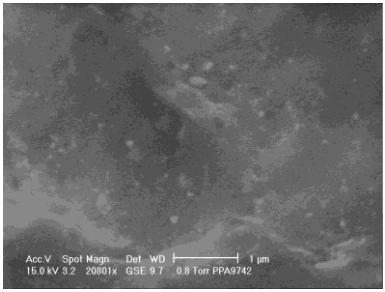

Fig. 5.1.c ESEM micrograph of AR974-2.

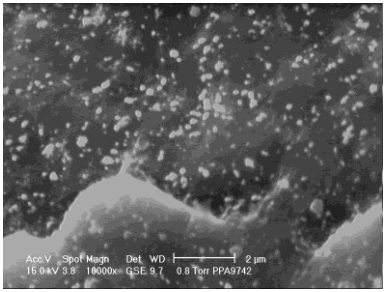

Fig. 5.1.d ESEM micrograph of AR974-2.

Figure 5.1 SEM analyses of PP-fumed silica plates with different nanofiller amount.

From the ESEM figures it is evidenced that fumed silica nanoparticles tends to form agglomerates in the PP matrix, with a mean diameter of less than 300nm. Similar results were already observed in case of HDPE fumed nanosilica composites [103]. This behavior can be attributed to the strong interaction of the surface hydroxyl groups of fumed silica nanoparticles, difficult to overcome even during melt-mixing with high shear rate [32]. In Figure 5.1a (AR805-0.5) low nanosilica amount, proportional to the nanofiller content, uniformly dispersed in the matrix can be observed. The aggregates size of about 250-450nm were distinguish, while also smaller particles with diameter lower than 100nm were visible. Similar results were also obtained for compositions with 2% vol. of the filler. In the Figure 5.1b particle size in the range from 300-75nm were detected. Results for silica type AR974 were reported in Figure 5.1c and d. For the composition containing 2% vol. of the filler (AR974-2) a lot of aggregates with diameter of about 280-140nm can be observed, while also smaller size up to 80nm were visible. We can say that high nanofiller content cause an aggregate formation. It can be concluded that no difference between two silica types were observed. In all the compositions silica aggregates were formed with the average size of about 300nm-150nm while also smaller particles with diameter of about 80-75nm were detected. Increasing the filler amount the mean distance between silica aggregates diminishes and the probability of nanofiller aggregation is therefore enhanced.

5.1.2. Thermal properties

In order to study the influence of nanosilica content on the thermal stability of polypropylene TGA analysis was performed. Representative TGA curves of plates and fibers are reported in Figure 5.2a and b, evidencing the beneficial effect of both type of fumed nanosilica on the thermal degradation resistance for all the nanocomposites with respect to the neat PP.

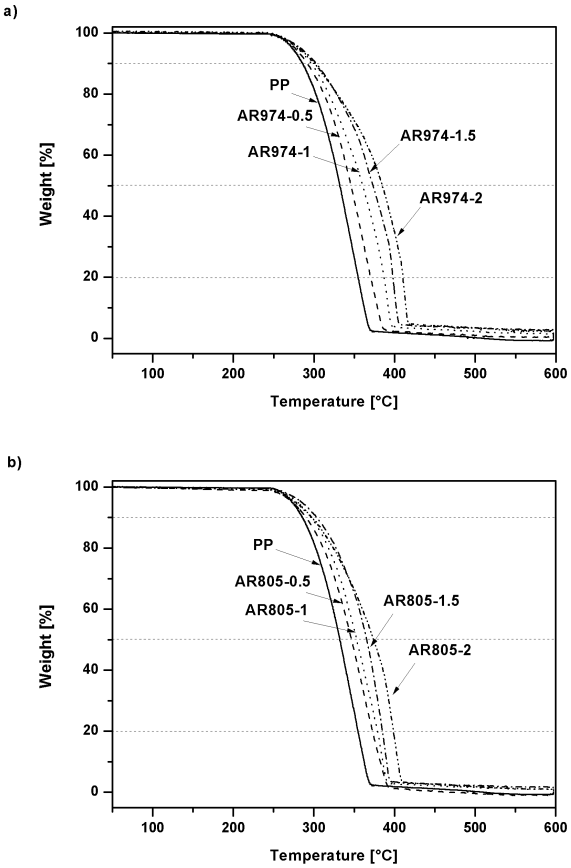

Figure 5.2. TGA curves of neat and nanofilled **(**a) PP-AR974 and (b) PP-AR805 plates performed under air atmosphere.

Sample	Temperature of 10% mass loss – $T_{0.1}$ [°C]	Temperature of 50% mass loss – $T_{0.5}$ [°C]	Temperature of 80% mass loss – $T_{0.8}$ [°C]	Residual mass at 600°C [%]
PP	284.7±0.5	332.2±1.0	354.4±1.5	0.00±0.0
AR974-0.5	289.8±1.0	346.5±0.5	372.5±0.5	0.4±0.1
AR974-1	296.3±0.5	353.0±1.5	378.2±0.7	1.0±0.3
AR974-1.5	302.8±1.5	366.0±0.8	384.8±1.0	1.6±0.2
AR974-2	297.6±0.3	373.7±0.5	398.2±2.0	1.8±0.4
AR805-0.5	291.0±0.2	345.7±1.0	379.3±1.0	0.4±0.1
AR805-1	296.0±1.5	360.0±0.8	386.3±0.8	1.2±0.4
AR805-1.5	299.0±0.5	372.6±0.5	397.3±1.5	1.5±0.6
AR805-2	302.7±0.6	384.1±1.0	410.4±0.5	1.7±0.5

Table 5.2. Results of TGA analysis of neat and nanofilled PP plates performed under air atmosphere.

It can be seen that all the samples showed a single degradation step with the remaining mass at 600°C very close to the theoretical nanosilica percentage. The comparison of thermal stability was carried out in terms of selected decomposition temperatures, in particular the initial degradation at 10% ($T_{0.1}$), and the temperatures $T_{0.5}$ and $T_{0.8}$ at which occurred 50% and 80% of mass loss, respectively. The decomposition temperatures ($T_{0.1}$, $T_{0.5}$, $T_{0.8}$) of PP-AR974/805 plates summarized in Table 5.2 were found to be higher than those of neat PP, even at low silica content. This confirmed stabilizing effect of nanofiller particles under oxidizing conditions. The highest improvement was found for compositions with 2% vol. of the both type of nanosilica, while between them slightly higher values were observed for silica AR805 type. If $T_{0.5}$ will be taken as comparison point, 40°C for AR974-2 and 52°C for AR805-2 higher temperature were observed for nanofiller material. Residual mass at 600°C is directly dependent on the nanofiller content, ranging between 0.4% for composition AR974/805-0.5 up to about 1.8% for AR805/974-2 plate. Analyzing these data from a general point of view, a remarkable stabilizing effect of silica nanoparticles on the thermal stability of PP under oxidation conditions can be detected. The incorporation of clay into a polyolefin matrix enhances its thermal stability by acting as a superior insulator and mass transport barrier to the volatile products generated during decomposition, making the diffusion path of the oxygen more tortuous, and thus retarding the thermo-oxidative process [46, 98, 99].

5.1.3. Differential Scanning Calorimetry

In Figure 5.3.a and b DSC thermograms of neat and nanofilled PP plates with different nanosilica content are respectively reported, while the most important results are summarized in Table 5.3.

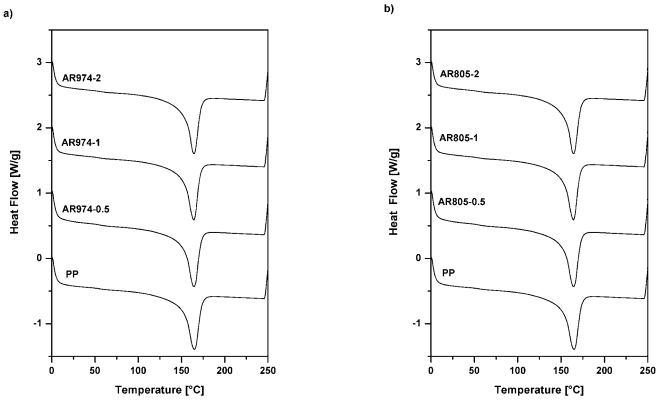

Figure 5.3. DSC thermograms of neat and nanocomposites PP with nanosilica type (a) AR974 and (b) AR805.

Sample	Onset of Melting Temperature T_m onset [°C]	Melting Temperature (I heatnig) T_m [°C]	Crystallinity Content X_c [%]	Onset of Crystallization Temperature Tc onset [°C]	Crystallization Temperature (cooling) T_c [°C]	Crystallinity Content X_c [%]
PP	151.2	165.0	46.6	119.6	116.1	49.7
AR974-0.5	151.3	164.4	46.0	120.2	116.6	50.2
AR974-1	151.0	164.5	45.5	120.6	116.9	49.3
AR974-1.5	152.0	164.4	46.4	122.0	118.0	49.0
AR974-2	153.1	164.4	47.0	124.6	120.2	49.0
AR805-0.5	150.3	164.2	46.8	120.2	116.0	48.4
AR805-1	150.0	164.5	46.1	120.4	116.2	48.1
AR805-1.5	150.0	164.0	45.5	120.6	117.2	48.0
AR805-2	150.0	164.2	45.0	120.8	117.2	48.2

Table 5.3. Results of the DSC analysis: crystallinity content (X_c), melting temperature (T_m), and crystallization temperature (T_c) for neat and nanofilled PP-AR974/805 plates.

If the data of melting temperatures (T_m) will be compared it can be observed that with the nanofiller content the values slightly decreases. However for the onset of T_m for compositions with AR974 silica type slightly higher (+2°C) values were observed,

while for AR805 the T_m did not change with nanofiller content. From the DSC cooling stage, it was noticeable that crystallization temperature of nanocomposites plates were higher than for neat PP, i.e. up to 120°C for AR974-2 and 117.2°C for AR805-2 versus 116°C, suggesting a mild effect of silica particles as nucleating agent. However, in case of crystallinity content no clear influence of fumed silica presence was observed in case of both nanofiller type, only slightly higher value was observed for composition AR974-2.

Literature data reported various effects of nanofiller on crystallization temperature and crystallinity content of polyolefin matrix, showing negligible [100], or significant [95, 102] effect, in dependence on both processing and composition. In our case, the crystallinity of nanofilled polymer was found almost the same in the case of neat material, whereas the crystallization temperature slightly increased with fumed nanosilica content. Comparing these results with the literature references, it is difficult to have clear image of the effect of nanosilica on the crystallization behavior of polypropylene matrix. It can be said that silica nanoparticles plays only a marginal role on the crystallization behavior of the PP matrix and the limited influence on the matrix properties were probably associated to their dispersion state [82].

5.1.4. Mechanical properties

Figure 5.4 a and b shows representative stress-strain curves of neat and nanofilled PP plates with different amount of two different type of fumed nanosilica from quasi-static tensile tests at break, while in Table 5.4 the elastic modulus and the tensile properties at yield (σ_y) and break (σ_b, ε_b) are summarized.

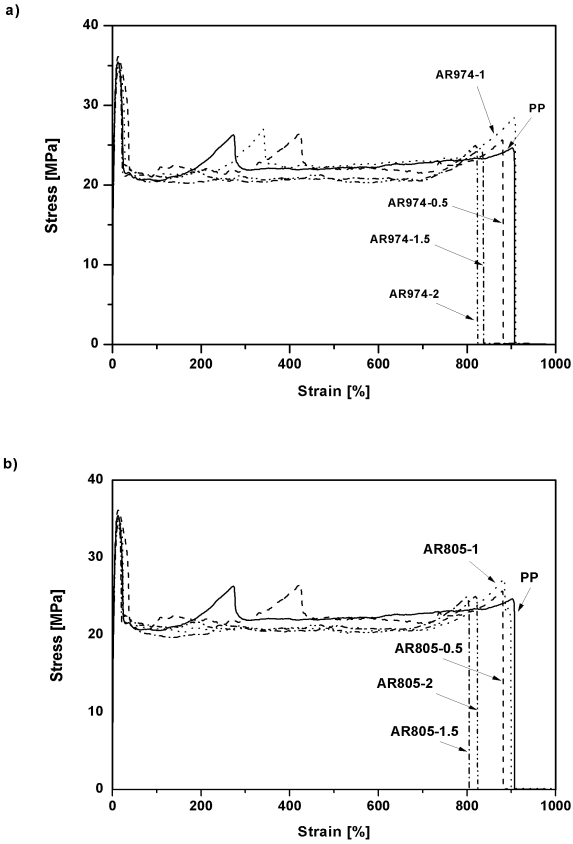

Figure 5.4. Representative tensile stress-strain curves of neat PP and fumed silica (a) AR974 and (b) 805 nanocomposites with different nanofiller content.

Sample	Elastic modulus [GPa]	Stress at yield σ_y [MPa]	Stress at break σ_b [MPa]	Strain at break ε_b [%]
PP	1.40±0.03	34.3±0.3	24.8±3.5	904±120
AR974-0.5	1.44±0.03	35.8±0.2	25.7±1.2	890±27
AR974-1	1.43±0.04	35.8±0.1	27.4±1.0	830±76
AR974-1.5	1.44±0.05	36.2±0.2	25.8±0.5	830±20
AR974-2	1.49±0.04	34.8±0.1	24.4±0.6	860±70
AR805-0.5	1.42±0.04	36.1±1.6	24.2±1.2	777±117
AR805-1	1.43±0.06	34.4±0.3	28.6±2.5	780±82
AR805-1.5	1.43±0.03	34.3±0.3	25.6±2.0	785±105
AR805-2	1.46±0.03	34.2±0.7	26.3±3.0	882±111

Table 5.4. Quasi-static tensile properties of polypropylene-fumed silica nanocomposites with different nanofiller content.

From the Figure 5.4 it can be seen that all the samples exhibit the typical cold-drawing behavior before the final break of the specimen. During this phenomenon tensile strength further increases and the stress whitening, due to the crystallization of aligned macromolecules, takes place [103]. As it commonly happens in polyolefin based nanocomposites, the introduction of fumed nanosilica leads to the improvement of the elastic modulus with respect to the neat PP [147, 152]. In case of our material the highest modulus was obtained for the compositions with 2% vol. of both silica types and enhancement of around 4% for AR805-2 and 6% for AR974-2 was observed. The explanation of this improvement hypothesized by many authors can be the presence of an interphase layer around the nanoparticles, promoting the stress transfer at the interface. The particles can limit the mobility and deformation of the matrix by introducing a mechanical restrains, caused by an effective attraction potential between segments of the chain and the repulsive potential that the polymer is subjected to when it is close to solid particles [103, 153, 154]. From DSC analysis higher crystallization temperature (T_c) were discovered for the nanofilled plates in comparison to neat PP. Therefore, it can be concluded that the stiffening effect observed after introduction of fumed silica can be attributed to the presence of an interphase around the nanoparticles. Moreover, also the tensile stress at yield (σ_y) was positively affected by nanofiller addition; especially compositions containing AR974 silica type, for AR805 the improvement was less significant. It is necessary to underline that an enhancement of the yield strength, even if small, is considered as an indication of a relatively strong filler-matrix interaction [104, 147]. This enhancement was observed together with higher stress at break in case of both fumed silica type. The highest improvement was obtained for the compositions with 1 % vol. of the filler, 10% and 15% higher values were observed for silica type AR974 and AR805 respectively. However, our material showed slightly lower strain at break properties in comparison to the neat PP, while the maximum reduction in strain was around 10-15%. In the major part of the polyolefin nanocomposites, the stiffening effect is accompanied by a heavy embrittlement, with a reduction of the tensile properties at break [104]. In case of our nanocomposites good dispersion of fumed silica aggregates within the matrix may lead to relatively lower stress concentration and cracking nucleation phenomena and consequently it is responsible for an

improvement of strength properties [103]. The stiffening effect provided by fumed silica can be predicted by the theoretical model developed from traditional microcomposites. In particular, elastic modulus can be represented by the modified Kerner equation proposed by Lewis and Nielsen [155] in the following form:

$$\frac{E_c}{E_m} = \frac{1+AB\phi}{1-\psi B\phi} \tag{5.2}$$

where:

$$A = \frac{7-5\upsilon_m}{8-10\upsilon_m},\ B = \frac{\frac{E_p}{E_m}-1}{\frac{E_p}{E_m}+A} \text{ and } \psi = 1+\left(\frac{1-\phi_{max}}{\phi_{max}^2}\right)\phi$$

where ϕ is the filler volume fraction, υ_m is the matrix Poisson ratio (for PP was taken as 0.45), ϕ_{max} represents the maximum packing fraction of the filler (0.632 for randomly close packed non-agglomerated spherical particles [156]), and finally E_p (for amorphous silicon dioxide is 70 GPa [157]) and E_m are the modulus of the nanofiller particles and the matrix. In Fig. 5.5.a the experimental data for nanocomposite plates were compared with theoretical previsions. It can be observed that obtained relative elastic modulus for compositions with silica type AR974 was higher and with silica AR805 was only slightly lower than predicted by Lewis-Nielsen equation. The higher experimental data are probably related to the fact that model did not take into account the filler-matrix interaction. However it can be concluded that this mode represents well the relative modulus of PP nanocomposite with fumed nanosilica.

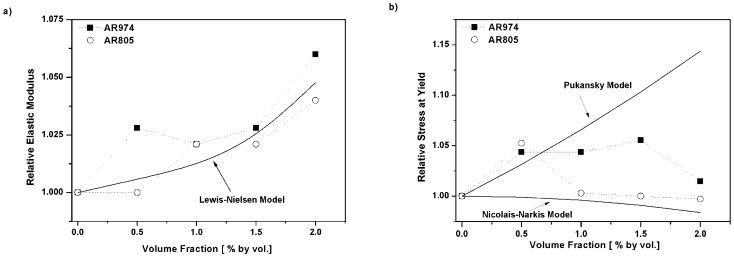

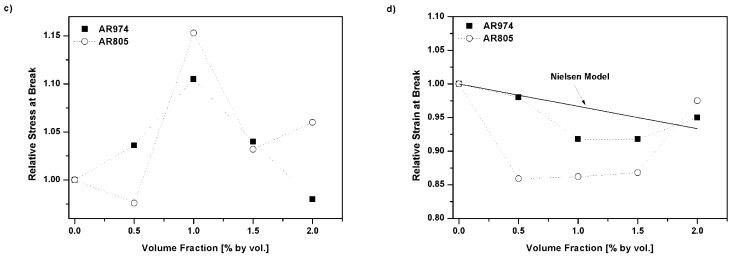

Figure 5.5 Quasi-static tensile properties of PP-AR974/AR805 nanocomposites normalized on the neat matrix values, **a)** elastic modulus with theoretical prediction according to Lewis Nielsen model, **b)** stress at yield with theoretical prediction according to Nicolais-Narkis and Pukansky models, **c)** stress at break and **d)** strain at break with theoretical prediction according to Nielsen model.

To predict stress at yield properties of our materials commonly used Nicolais-Narkis equation was applied. This equation is a two-third power law function with *K* as a parameter for filler-matrix adhesion taken as 1.21 commonly used for poor filler matrix interaction [158]:

$$\frac{\sigma_{yc}}{\sigma_{ym}} = 1 - K(\phi)^{2/3} \quad (5.3)$$

where σ_{yc} and σ_{ym} are respectively the stress at yield of the composite and the matrix. According to this model, adopted for particulate filled microcomposites, the stress at yield would gradually decrease with the filler content. Another equation to describe stress at yield properties was proposed by Pukanszky [159]:

$$\frac{\sigma_{yc}}{\sigma_{ym}} = \left(\frac{1-\phi}{1+2.5\phi}\right) \cdot \exp\left(B\phi\right) \quad (5.4)$$

where *B* is an parameter characterizing interaction between matrix and filler and was chosen by minimizing chi-square values during the fitting procedure. In Figure 5.5.b the relative stress at yield data of PP nanocomposites with two types of fumed silica and with fitting lines according to Pukanszky and Nicolais-Narkis models are reported. It can be observed that our results are located between both lines representing two models. In case of compositions with low nanofiller content (0.5% vol.) Pukanszky model seems to satisfactory fit yield stress data, while with higher nanofiller content is completely unsuitable. In case of Nicolais-Narkis model it fits

quite well for nanofiller content higher than 1% vol. in case of compositions with AR805 silica type, while for PP-AR974 is completely unsuitable.

From Figure 5.5.c relative stress at break was plotted versus nanofiller content. It is evident that the introduction of fumed silica leads to a remarkable improvement of the stress at break with maximum increments close to 15% for AR805-1 sample with respect to the neat PP. The good dispersion of fumed silica leads to relatively lower stress concentration and cracking nucleation phenomena what affect higher stress at break.

For higher nanofiller content larger aggregates, observed also at SEM images causes drop of strain at break properties. In Figure 5.5.d strain at break together with the prediction of Nielsen model [160] originally proposed to model the strain at break of spherical microparticles filled composites with good adhesion between filler, were reported:

$$\varepsilon_{bc} = \varepsilon_{bm} \cdot \left(1 - \phi^{1/3}\right) \quad (5.5)$$

where ε_{bc} and ε_{bm} are respectively the strain at break of the composite and matrix and ϕ is filler volume fraction. As we already mentioned before lower strain at break properties were obtained for the nanofilled plates in comparison to neat PP. However, the drop of the mechanical properties was not dramatic and they were lower at most around 10-15%. As reported in Figure 5.5.d for the compositions containing AR805 silica type and higher nanofiller content of silica type AR974, the obtained values were lower than predicted by Nielsen model, originally developed for microfilled composites. It can be concluded that the trends of the tensile properties at break observed for fumed silica nanocomposites are not explicable on the basis of the models proposed for traditional microcomposites.

It has to be considered that viscoelastic behavior of performed nanocomposites is mainly ruled by the filler surface area and interfacial interaction between the matrix and filler. It is known that polyolefines due to their hydrophobic nature cannot have a good affinity with inorganic fillers. However, good physical polymer-matrix interaction can be obtained also in case of polyolefines because of the presence of carbonylic and hydroxyl groups on the backbone of the matrix macromolecules, observed also by FTIR analysis as a peak at about 1740cm^{-1} associated to the stretching of

carbonylic groups. This situation was depicted in Figure 5.6a and 5.6b. Dorigato hypothesize that only amorphous segments of the polymer chain interact with the silica nanoparticles. The hydrogen bond formatted between hydroxyl group of fumed silica aggregates and carbonyl/hydroxyl groups of thermally oxidized parts of polymer chains may create physical entanglement affecting the mechanical properties of the material [161].

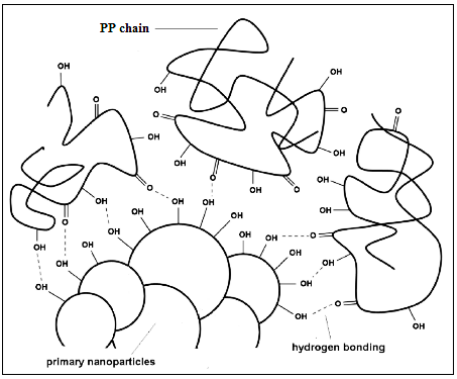

Figure 5.6.a. Schematic representation of the polymer filler interaction in PP – fumed silica nanocomposite [161].

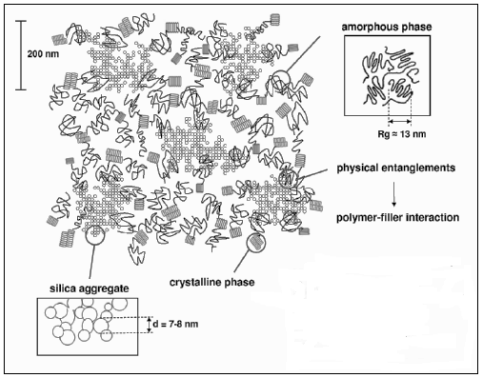

Figure 5.6.b. Proposed schematic of polymer filler interaction in the polymer-fumed silica nanocomposites [161].

5.1.5 Summary PP-FS plates

Two kind of modified fumed nanosilica, were mixed together through the melt compounding process, with PP matrix in order to investigate their influence on the thermal and mechanical properties and select the best compositions for further fiber spinning process. From the microstructural characterization the well distributed nanoparticles aggregations in the polymer matrix were visible, however no differences related to different surface area of silica type were observed. Consequent, both fumed nanosilica positively affected the thermal degradation stability and mechanical properties as elastic modulus and stress at break without heavily affecting strain at break. Based on these results for PP fiber preparation the same nanosilica type with nanofiller content form 0.25% vol. up to 2% vol. were selected.

5.2. PP-fumed silica nanocomposite fibers

After preliminary characterization made on the polypropylene fumed silica plates, the compositions in form of fibers, as reported in Table 5.5 were performed in a two-stage process (melt-extrusion and hot-drawing).

Material	PP [% vol.]	Aerosil [% vol]	Fusabond F613 [% vol]	Screw speed [rpm]	MFI [dg/min]
PP	100	0.0	-	10	1.84±0.08
AR974/AR805-0.25	99.75	0.25	-	10/10	2.04±010 / 2.00±0.07
AR974/AR805-0.5	99.50	0.5	-	9.5/9.5	2.40±0.14 / 2.40±0.08
AR974/AR805-1	99.0	1.0	-	8.5/8.5	2.52±0.08 / 2.50±0.05
AR974/AR805-2	98.0	2.0	-	8/7.5	2.69±0.20 / 2.64±0.15
AR974-0.5/PPgMA-0.5	99.0	0.5	0.5	10	3.20±0.15
AR974-0.5/PPgMA-1	98.50	0.5	1	11	3.62±0.20

Table 5.5. Designation and formulation of PP nanocomposites (in percentage by vol.).

5.2.1. Morphology

It should be noted the MFI values increased with the percentage of silica in the polymer matrix, with an almost linear dependence on the PP-AR974/805 composition. Moreover, if data obtained for plates and fibers will be compared, similar as in case of HDPE-LDH compositions higher MFI values were observed for

plates. As in previous case, this behavior can be explained by the better filler dispersion obtained during melt spinning in comparison to melt compounding process. It is established that filler dispersion and adhesion with the polymer matrix are fundamental for improving the mechanical properties of composites.

Figure 5.7 shows the infrared spectrum of compositions with 1%, 2% and 5% vol. of fumed silica in comparison with neat PP. For the nanofilled compositions higher intensity of two peaks located at 1097cm^{-1} and 1741cm^{-1} in comparison to neat PP can be observed. The peak at 1097 cm^{-1} is related to the stretching of the Si - O - Si groups, which indicates the increasing presence of fumed silica within the material.

The presence of carbonyl groups is evident by the peak at 1740 cm^{-1}, attributable to the stretching of this type of groups [162]. It is important to note that this peak are absent in the spectrum of the neat PP.

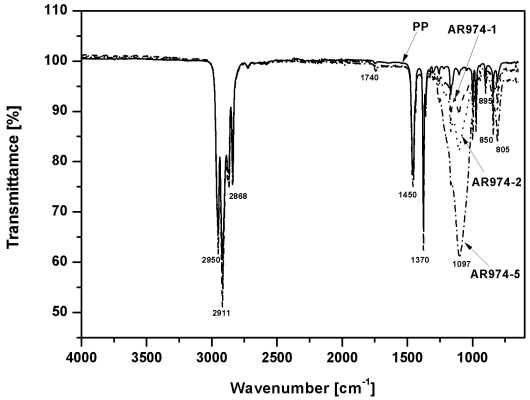

Figure 5.7. FTIR spectra of neat PP and PP composites with 1%, 2% and 5% vol. of fumed silica AR974.

In order to explain the behaviour of prepared PP – fumed nanosilica fibers, the surface of fractured specimens in liquid nitrogen were tested with SEM microscopy. Figure 5.8 shows the SEM images of the fiber morphology of PP-silica filaments. It can be observed in the Fig. 5.8 a and b that the external fibers surface is smooth. If the cross section of the fracture samples will be compared the difference in nanosilica distribution can be observed. For low nanofiller content 0.25% vol. and

0.5% vol. (Fig 5.8c and d), well dispersed silica particles are visible with the average size in range of about 50-100nm. As seen, an increase in volume silica loading leads to an increase silica particle density and agglomerations appears (Figure 5.8.e-f). Moreover, it can be see that similar distribution was observed for both silica type AR974 (Figure 5.8.e-f) and AR805 (Figure 5.8.g-h). For example for compositions with 2% vol. of nanofiller particle size was very diverse, from single parties with size of about 50nm-100nm up to aggregates of about 500nm-800nm. These results are in good agreement with previous research where similar sizes of nanosilica particles were founded [163-165]. Moreover, the aggregated morphology, observed for high SiO_2 content, can be attributed to the strong interaction between the surface hydroxyl groups of the nanoparticles that increases with higher concentration [103].

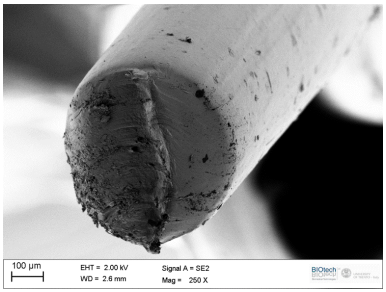

Fig. 5.8.a ESEM micrograph of AR974-0.5.

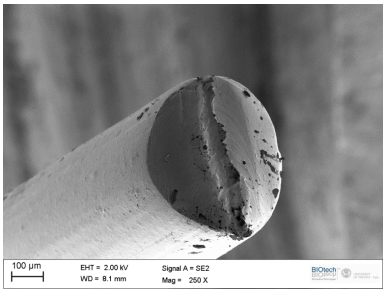

Fig. 5.8.b ESEM micrograph of AR974-1.

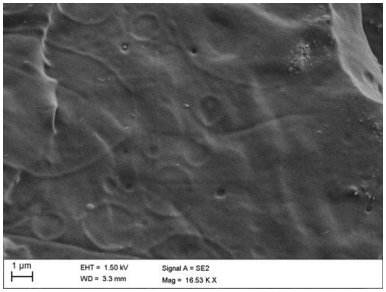

Fig. 5.8.c ESEM micrograph of AR974-0.25.

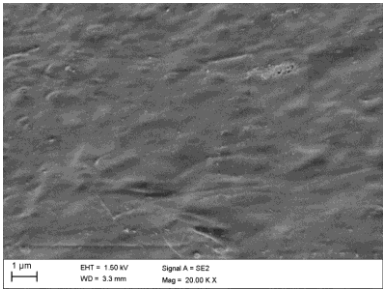

Fig. 5.8.d ESEM micrograph of AR974-0.5.

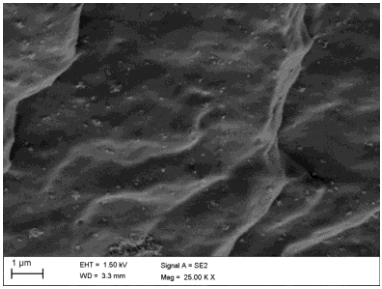

Fig. 5.8.e ESEM micrograph of AR974-2.

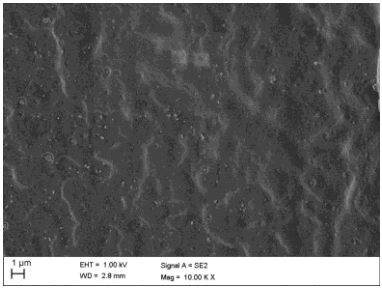

Fig. 5.8.f ESEM micrograph of AR974-2.

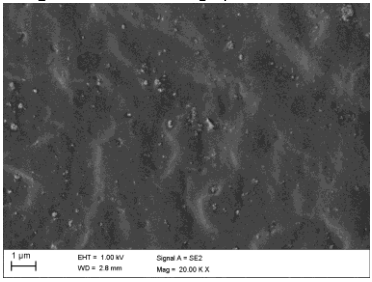

Fig. 5.8.g ESEM micrograph of AR805-2.

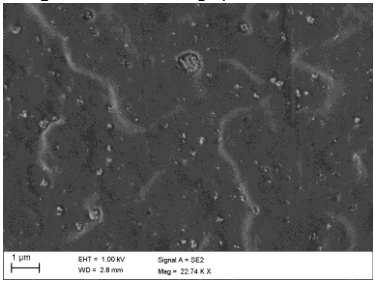

Fig. 5.8.h ESEM micrograph of AR805-2.

Figure 5.8. Cross section view of PP-fumed nanosilica fibers (a) AR974-0.5, (b) AR974-1, (c) AR974-0.25, (d) AR974-0.5, (e) and (f) AR974-2 and (g) and (h) AR805-2.

Dispersion of silica fillers in PP polymer composites fibers was visualized also by transmission electron microscopy (TEM) in Figure 5.9.a-k. Specimens for TEM analysis were prepared by ultramicrotomy by cutting perpendicularly to the fiber length. In all TEM micrographs performed for different draw ratios it was managed to visualize quite homogeneous filler dispersion in the polymer matrix, but the silica particles occurred in small agglomerates. It can be seen that drawing process reduces the size of nanoparticles, from around 600-800nm for DR=5 up to around 100-200nm for DR10 and 15, while there is no significant difference in nanofiller size between draw ratio 10 and 15. Moreover, from the pictures of AR805-2 made for DR=20 (Fig. 5.9i-k) lower nanofiller size, less than 100nm, were observed. It can be concluded that drawing process significantly reduces the nanofiller size and allows the homogeneous dispersion; what will affect the filler-matrix interaction and consequently influenced the thermo mechanical properties of the fibers.

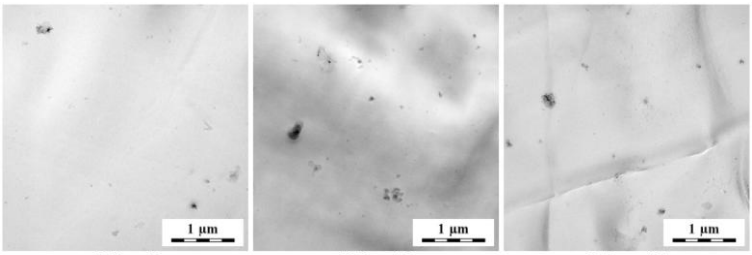

Figure 5.9.a TEM micrographs of PP compounds with 0.25% vol. of AR805 (mag. 23 000).

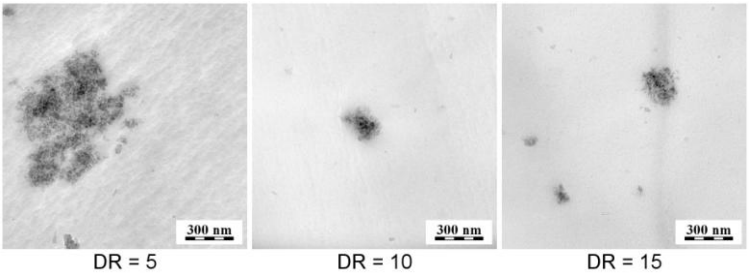

Figure 5.9.b TEM micrographs of PP compounds with 0.25% vol. of AR805 (mag. 59 000).

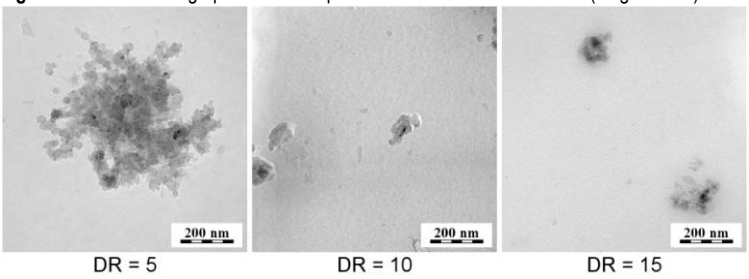

Figure 5.9.c TEM micrographs of PP compounds with 0.25% vol. of AR805 (mag. 97 000).

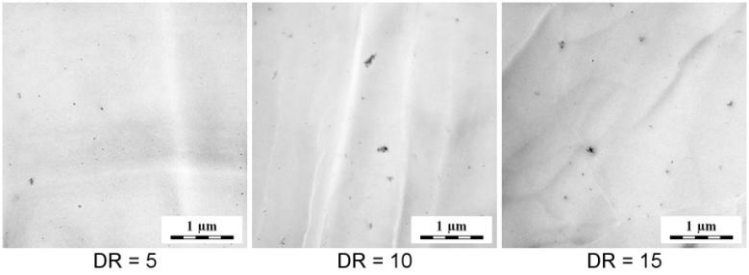

Figure 5.9.d TEM micrographs of PP compounds with 0.5% vol. of AR805 (mag. 23 000).

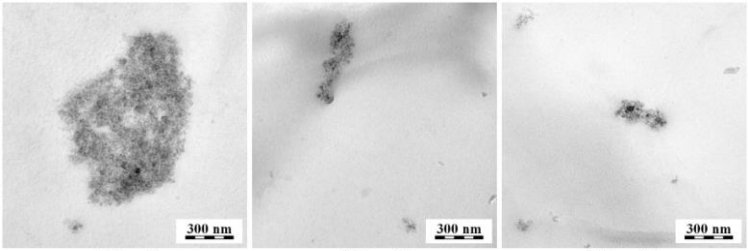

DR = 5 DR = 10 DR = 15

Figure 5.9.e TEM micrographs of PP compounds with 0.5% vol. of AR805 (mag. 59 000).

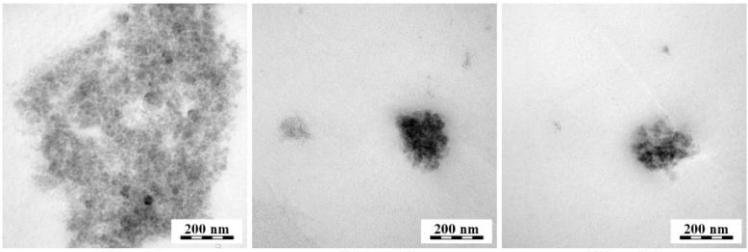

DR = 5 DR = 10 DR = 15

Figure 5.9.f TEM micrographs of PP compounds with 0.5% vol. of AR805 (mag. 97 000).

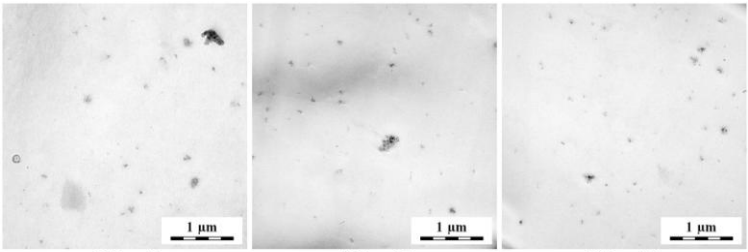

DR = 5 DR = 10 DR = 15

Figure 5.9.f TEM micrographs of PP compounds with 1% vol. of AR805 (mag. 23 000).

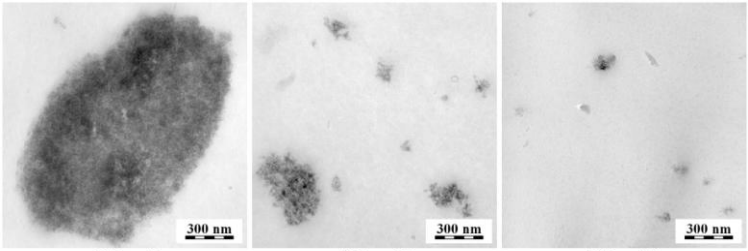

DR = 5 DR = 10 DR = 15

Figure 5.9.gTEM micrographs of PP compounds with 1% vol. of AR805 (mag. 59 000).

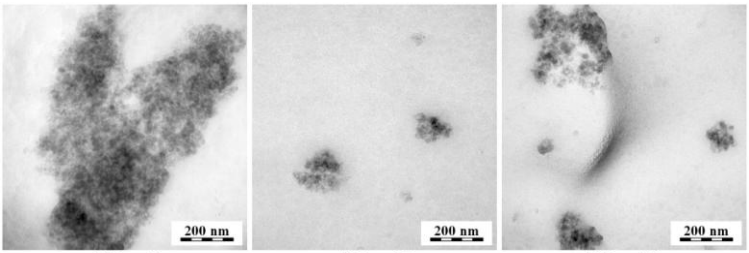

Figure 5.9.h TEM micrographs of PP compounds with 1% vol. of AR805 (mag. 97 000).

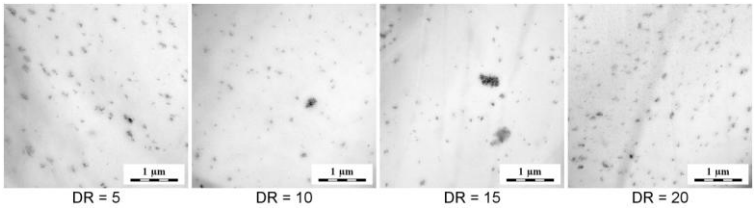

Figure 5.9.i TEM micrographs of PP compounds with 2% vol. of AR805 (mag. 23 000).

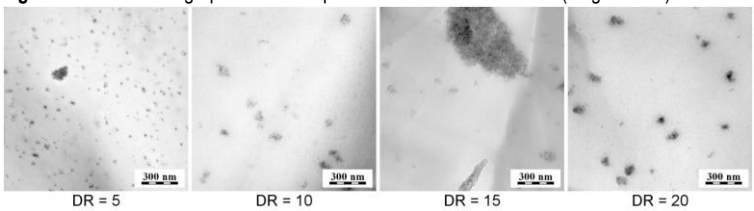

Figure 5.9.j TEM micrographs of PP compounds with 2% vol. of AR805 (mag. 59 000).

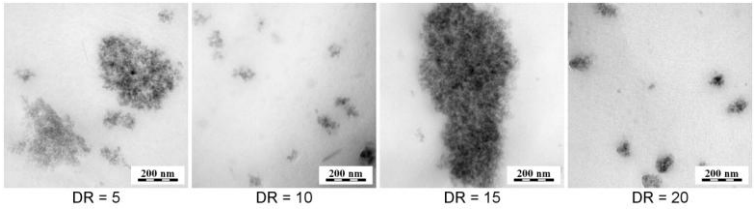

Figure 5.9.kTEM micrographs of PP compounds with 2% vol. of AR805 (mag. 97 000).

Figure 5.9 Cross section view of PP-fumed nanosilica AR805 fibers for different nanofiller content and different draw ratio (DR).

5.2.2. Thermal properties

The TGA analysis was performed to evaluate thermal stability of the fibers as well as particle-matrix interaction. In Fig.5.10.a and b thermogravimetric curves of as-spun

neat and nanocomposites PP fibers with different nanosilica type were reported. The temperature at with 10% (designed as $T_{0.1}$), 50% ($T_{0.5}$) and 80% ($T_{0.8}$) mass loss occurred were summarized in Table 5.6.

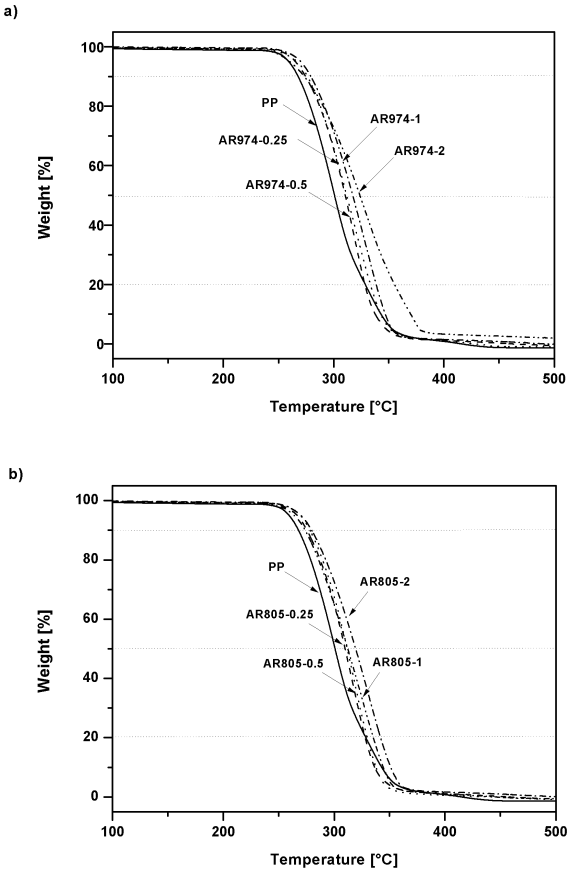

Figure 5.10. TGA thermograms of neat and PP nanocomposites as-spun fibers with different fumed silica (a) AR974 and (b) AR805 content.

Material	Temperature of 10% Mass loss -$T_{0.1}$ [°C]	Temperature of 50% Mass loss - $T_{0.5}$ [°C]	Temperature of 80% Mass loss - $T_{0.8}$ [°C]	Residual mass at 600°C [%]
PP	267±2	301±3	328±2	0.0±0.0
AR974-0.25	274±2	310±3	329±2	0.5±0.1
AR974-0.5	276±3	312±3	333±2	0.8±0.1
AR974-1	280±2	317±3	338±2	1.2±0.3
AR974-2	274±2	324±2	355±3	3.3±0.2
AR974-0.5/PPgMA-0.5	282±2	324±1	346±1	0.5±0.1
AR974-0.5/PPgMA-1	282±2	327±2	347±2	0.5±0.1
AR805-0.25	275±1	310±2	327±2	0.3±0.1
AR805-0.5	278±2	312±2.	330±3	0.8±0.2
AR805-1	279±2	313±2	335±2	1.1±0.3
AR805-2	273±3	319±2	342±3	1.8±0.3

Table 5.6. Results of TGA analysis of neat and nanofilled as-spun PP fibers performed under air atmosphere.

The decomposition temperatures of nanofilled PP fibers were found higher than those of neat PP, even at low fumed silica content. For example $T_{0.1}$ increased from around 8°C for AR974/AR805-0.25 up to 12°C for AR974/AR805-1. In case of temperature at with 50% and 80% weight mass loss occurred improvement was even higher, from around 10°C for 0.25% vol. up to 23/19°C for AR974/805-2. of nanofiller in case of $T_{0.5}$, and from 1°C up to 26/13°C for AR974/805-2 at $T_{0.8}$. Analyzing presented data a remarkable stabilizing effect on thermal properties of silica nanoparticles can be noticed. Similar improvement has been already reported in case of polyethylene – Aerosil®AR974 plates [103] and polypropylene [166] fumed silica nanocomposites fibers. This behavior is related to the fact that silica nanoparticles may act as thermal insulator, making the diffusion path more tortuous and limit the diffusion of oxygen in the polymer matric [34]. Moreover as it was reported by Sinha Ray and Okamoto [32] the nanosilica particles acts as a heat barrier, which enhances the overall thermal stability of the system, as well as assist in the formation of char after thermal decomposition. In the early stages of thermal decomposition, the clay would shift the decomposition to higher temperature. While during progressive thermal degradation silica aggregates tends to agglomerate to the surface of molten polymer creating a barrier that protects from heat the remaining polymer matrix and impedes the volatilization of the combusted products [32, 103]. Other authors explain improvement in degradation temperature as higher energy that has to be applied to break down adhesion force at polymer-silica interface [166]. In case of good interfacial adhesion, particles can restrain the

movement of polymer chain, making the scission of a polymer chain harder at lower temperature and in this way improving the thermal degradation stability. What can be observed in case of our material, for composition containing 2% vol. of AR974/805 temperature improvement in comparison to neat PP at with 10% mass lost (initial degradation temperature) was slightly lower (6°C) in comparison to other PP-silica nanofibers (enhancement from 7°C up to 12°C). As can be seen in SEM images, aggregates of silica particles (around 0.7μm) were observed in case of fibers with 2% vol. of fumed nanosilica. This will affect poor interfacial adhesion to the polymer matrix what will influence lower improvement in thermal stability. In case of higher temperature silica nanoparticles, as it was already mentioned before will create barrier protection for molten polymer, and respectively higher stability for composition with 2% vol. will be obtained in comparison to lower nanofiller content. At the end it is necessary to underline that for silica type AR974 slightly higher thermal stability was obtained what can be related to the higher surface are ($170 m^2 \cdot g^{-1}$) and better filler - matrix adhesion in comparison to Aerosil AR805 ($150 m^2 \cdot g^{-1}$).

5.2.3. DSC analysis

In Figure 5.11a-d DSC thermograms of neat and nanofilled PP fibers at different draw ratios are respectively reported, while the most important results are summarized in Table 5.7 and 5.8.

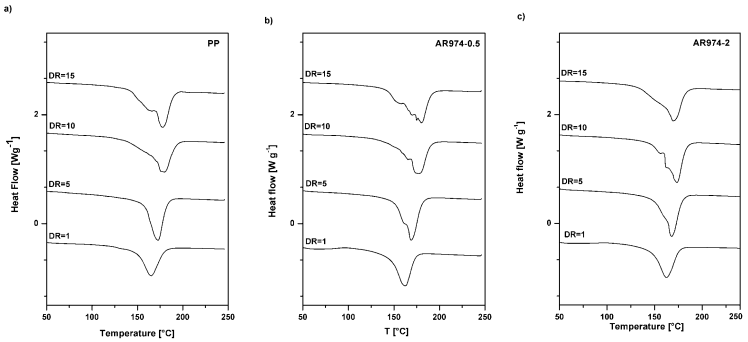

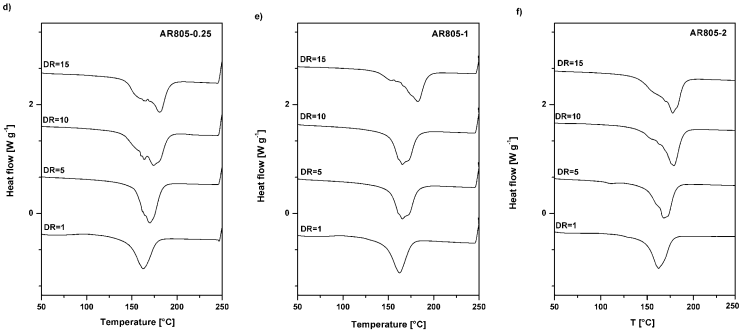

Figure 5.11. DSC thermograms of neat PP (a) and nanofilled PP nanocomposites with different type and nanosilica content (b) AR974-0.5, (c) AR974-2, (d) AR805-0.25, (e) AR805-1 and (f) AR805-2 and at different DR values (first heating stage).

Sample	DR	Onset of Melting Temperature Tm onset [°C]	Melting Temperature T_m [°C]	Crystallinity Content (I heating) X_c [%]	Onset of Crystallization Temperature T_c onset [°C]	Crystallization Temperature T_c [°C]	Crystallinity Content (cooling) X_c [%]
PP	1	148.2	165.1	36.4	116.6	111.5	44.7
	5	157.4	172.5	45.0	120.1	112.8	49.5
	10	160.0	179.7	50.4	121.4	114.1	47.2
	15	166.4	178.0	53.2	118.2	114.6	48.8
AR974-0.25	1	145.5	162.2	40.3	120.0	115.7	46.8
	5	154.5	164.8	45.9	122.0	115.8	47.8
	10	161.4	182.7	49.7	122.4	114.1	47.0
	15	162.0	183.0	51.0	120.0	115.4	47.0
AR974-0.5	1	145.2	162.4	40.6	121.4	116.9	46.8
	5	159.7	168.8	47.1	117.7	111.4	47.1
	10	165.2	176.2	49.2	122.3	114.6	47.2
	15	160.5	180.3	53.4	119.0	115.6	46.7
AR974-0.5 /PPgMA-0.5	1	146.3	161.5	41.0	122.7	117.5	49.5
AR974-0.5 /PPgMA-1	1	146.3	162.5	40.7	122.6	117.7	49.8
AR974-1	1	146.9	163.3	39.2	120.8	115.1	48.2
	5	148.5	164.9	43.7	118.2	114.6	46.7
	10	165.2	176.4	47.6	120.2	114.1	45.0
	15	160.8	178.4	52.3	118.0	112.8	47.5
AR974-2	1	146.5	162.5	38.4	122.8	118.2	47.1
	5	159.4	168.1	44.5	120.3	115.6	47.8
	10	159.3	173.5	47.0	120.0	115.0	47.0
	15	162.0	174.6	50.3	119.4	113.6	47.0

Table 5.7. DSC results of neat and nanofilled PP-AR974 fibers with different draw ratio values.

Sample	DR	Onset of Melting Temperature T_m onset [°C]	Melting Temperature T_m [°C]	Crystallinity Content (I heating) X_c [%]	Onset of Crystallization Temperature T_c onset [°C]	Crystallization Temperature T_c [°C]	Crystallinity Content (cooling) X_c [%]
PP	1	148.2	165.1	36.4	116.6	111.5	44.7
	5	157.4	172.5	45.0	120.1	112.8	49.0
	10	160.0	179.7	50.4	121.4	114.1	47.2
	15	166.4	178.0	53.2	118.2	114.6	48.8
AR805-0.25	1	143.8	161.7	41.5	118.9	114.0	47.6
	5	154.5	170.0	49.6	121.9	115.8	47.8
	10	154.8	174.0	56.2	122.5	115.0	47.5
	15	162.4	180.7	53.0	117.3	112.0	46.4
AR805-0.5	1	144.4	160.7	43.0	119.1	114.3	48.6
	5	152.0	172.0	45.0	116.5	111.5	45.6
	10	160.4	174.1	49.2	117.4	111.1	45.6
	15	162.5	180.0	52.7	120.0	113.0	46.7
AR805-1	1	146.1	162.3	38.4	119.2	114.4	47.0
	5	152.0	165.2	45.7	117.5	112.1	46.2
	10	164.2	175.8	50.5	117.6	109.7	48.0
	15	160.6	182.4	52.0	118.1	112.7	42.0
AR805-2	1	147.5	162.5	41.1	119.6	114.4	49.2
	5	156.8	167.9	43.4	116.2	110.2	46.5
	10	161.1	179.0	51.2	122.5	114.0	47.3
	15	162.4	177.4	53.5	118.4	113.8	46.5

Table 5.8. DSC results of neat and nanofilled PP-AR805 fibers with different draw ratio.

In the thermograms depicted in Fig.5.11 a-f), single and sharp melting peak were observed for DR=1 and 5. However multiple distinct melting peak were seen for fibers with DR=10 and 15. The melting behavior of strained fibers with a draw ratio 10 is related to the difference of crystal forms and degree of perfections obtained during drawing. A broad endotherm peak seems to be composed of two or in some cases even three peaks. The presence of these peaks is most probably related to the melting peak of folded-chain crystals, extended-chain crystals, and crystalline morphology between folded- and extended- chain crystalline. This idea is also supported by the melting behavior of the fibers with a draw ratio 15. This confirms that at a higher draw ratio (DR>10) transformations of folded- to extended- chain structure occur in the fibers and the perfection of the folded-chain structure in the fibers is improved [167].

Comparing the crystallinity degree (X_c), melting (T_m) and crystallization (T_c) temperature of as-spun neat and nanofilled fibers significant differences can be found. Higher T_c (4-7°C) and crystallinity content (2-7%) together with lower T_m values (1-5°C) were observed for PP-FS fibers. Rottstegge observed for

polypropylene silica nanocomposite fibers enhancement in the crystallinity content [168]. Slightly lower T_m results were already reported in case of polyolefins fibers [82, 145, 169] while in contrast to our material lower crystallinity content and T_c were also observed. On the other hand there are reports were improvement in T_m and T_c values were observed together with lower crystallinity content [80, 125]. It can be conclude that higher crystallization temperature and crystallinity content suggesting a possible nucleating role both type of the fumed nanosilica. It is interesting that between both nanosilica types lower crystallization temperatures and slightly higher crystallinity content in case of AR805 in comparison to AR974 were observed. Moreover, in case of AR974 nanofilled as-spun fiber crystallization temperature gradually increases with fumed silica content while in case of AR805 T_c is higher than for neat PP while is not changing with nanofiller content. These differences can be related to the different surface area and different surfactant used for both FS types. Most probably higher surface area and surfactant with short and branched chain that was used for the modification of silica AR974 affected better interfacial adhesion and was more effective as nucleating agent.

As it was mentioned before, for the composition with 0.5% vol. of the AR974 filler compatibilizer with a corresponding ratio 1:1 and 1:2 was added. From DSC analysis performed for the as-spun material the same melting temperature and crystallinity content in comparison to AR974-0.5 were obtained (Table 5.7.), T_m=162°C and X_c=41% respectively. However, if crystallization temperature and crystallinity content from the cooling stage will be compared, slightly higher values were detected for both compositions with compatibilizer, in particular T_c increases from 116.9°C for AR974-0.5 up to 117.5°C for the compositions with 0.5% vol. and 1% vol. of compatibilizer, and crystallinity content increases from 46.8% up to 49.5%. Higher values might suggest positive influence of the compatibilizer on the nanofiller distribution that affects crystallization condition and interfacial adhesion between filler and matrix.

With DR T_m for both compositions increases what can be attributed to the fact that during drawing process the folded-chain crystals become more perfect. It can be noted that T_m increases up to DR=10 while after with additional drawing (up to DR=15) the melting temperature does not increase anymore and tends to level off at

about 160°C. Similar behavior was already observed in case of HDPE-fumed silica fibers [82]. Crystallization temperature was found to be higher in case as-spun nanofilled fibers in comparison to neat PP. Moreover, with higher draw ration T_c decreased for the nanofilled fibers.

For all the compositions with nanofiller crystallinity content was higher than for neat PP. Moreover, with the DR crystallinity content increased. It can be observed that drawing process induced crystallinity content; in case of material drawn 5 times the improvement was around 5-9% for AR974 and 2-7% for AR805. In case of DR=10 it was around 2-4% for AR974 and 4-8% for AR805, for DR15 was in range of 2-5% for AR974 and AR805. Higher crystallinity content observed after drawing is a typical behavior, and it is related to the high degree of order and continuity of the crystalline phase [166]. From this data it can be observed that with higher DR this improvement becomes less significant and tends to level off at a value of about 53%. It can be concluded that during drawing with an increase of the draw ratio polymer chains orient themselves and crystallize rapidly in the draw direction [5]. As it was already mentioned before different research performed on the polyolefin fibers presents different kind of improvement and its difficult to have clear information of the effect of fumed nanosilica on the crystallization behavior of polypropylene fibers. From the overall view if the properties at ultimate DR (DR=10 and 15) will be compared slightly higher values in case of crystallinity content and both T_m and T_c temperatures were observed for the compositions with low nanofiller content 0.25% and 0.5% vol. From the SEM and TEM analysis good dispersion for these two compositions was already presented. This may indicates that apart from the drawing, change in degree of molecular orientation could arise from interactions between the filler and polymer matrix [166]. It can be conclude that since from data obtained for as-spun fibers the influence of fumed nanosilica on the nucleation process can be observed; in case of drawn material this effect was not well evidenced.

5.2.4 Mechanical properties

5.2.4.1 As-spun fibers

In Figure 5.12 and 5.13 representative curves of quasi-static tensile tests for as-spun and drawn neat and nanofilled PP fibers are reported, while in Table 5.9 tensile properties at yield and at break for as-spun material are summarized.

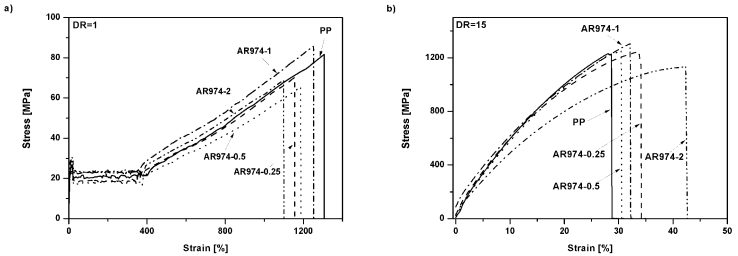

Figure 5.12. Representative curves of quasi-static tensile test of neat and nanofilled PP-AR974 fibers with different draw ratio (DR) (a) DR=1 and (b) DR=15.

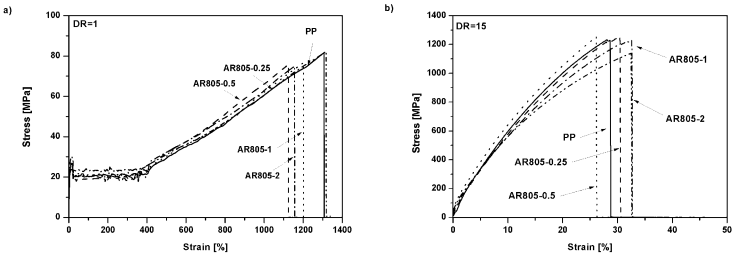

Figure 5.13. Representative curves of quasi-static tensile test of neat and nanofilled PP-AR805 fibers with different draw ratio (DR) (a) DR=1 and (b) DR=15.

Sample	E [GPa]	σ_b [MPa]	ε_b [%]	σ_y [MPa]	ε_y [%]
PP	0.48±0.06	83±7	1260±55	27±2	16±2
AR974-0.25	0.58±0.04	74±3	1160±28	24±1	14±1
AR974-0.5	0.67±0.02	70±6	1180±54	24±1	13±3
AR974-1	0.67±0.03	83±6	1250±68	29±3	14±2
AR974-2	0.68±0.01	62±8	1090±13	31±1	15±2
AR974-0.5/PPgMA-0.5	0.60±0.02	70±6	1304±80	28±1	15±3
AR974-0.5/PPgMA-1.0	0.66±0.04	70±2	1251±42	29±1	14±1
AR805-0.25	0.54±0.03	82±6	1275±61	25±2	13±1
AR805-0.5	0.60±0.06	78±3	1125±16	25±1	13±3
AR805-1	0.61±0.03	76±5	1203±44	26±2	14±1
AR805-2	0.65±0.02	72±5	1108±83	26±7	15±1

Table 5.9. Quasi-static tensile properties at yield and break of neat PP and nanofilled as-spun fibers

It is important to observe that undrawn fibers manifest a clear yield point at low strain followed by a wide plastic plateau and a strain hardening region until the break point (Fig. 5.12a and 5.13a). Drawing process produces a strong orientation of the macromolecules along the drawn direction and strain-induced crystallization of the amorphous regions, with a consequent increase of the fiber stiffness and disappearance of yielding phenomena (Fig. 5.12b and 5.13b). First of all, for all of the compositions higher elastic modulus was observed, improvement from 0.48 GPa for neat PP up to 0.58/0.54 GPa for AR974/805-0.25 and 0.68/0.65 GPa for AR974/805-2 was obtained. Tensile stress at yield (σ_y) slightly increased for the compositions with high nanofiller content (1 and 2% vol.), however slightly lower values were observed for the compositions with low fumed silica amount. The improvement of the yield strength is a signal of a quite good interfacial adhesion between PP and nanoparticles. This behavior was observed together with enhancement in elastic modulus what usually coursed decrease of the yield stress [170]. This follows from the fact that traditional fillers do not bear the load in the direction of deformation what confirms lower values for a stress at break (σ_b) and the strain at break (ε_b). However, for AR974-1 and AR805-0.25 the properties were slightly higher than for neat PP. It can be observed that both silica types gave very similar improvement; only in case of elastic modulus the difference between nanofillers was well visible and was related to the higher surface area of the AR974 in comparison to AR805. For the comparison in the Table 5.9 data obtained for the composition AR974-0.5 with compatibilizer were also introduced. It can be seen that in this case lower elastic modulus values were obtained for fibers with compatibilizer in comparison to composition only with 0.5% vol. of silica. In case of stress at break the values were the same, while strain at break and properties at yield increases. Higher elongation may indicate better nanofiller distribution what can leads to relatively lower stress concentration and cracking nucleation phenomena. Consequently, the smaller dimensions of silica aggregates are responsible for the improvement both of the strain at break and properties at yield.

5.2.4.2 Drawn Fibers

Elastic modulus (*E*) results obtained for different PP-fumed nanosilica fibers are reported in the Fig. 5.14 a) for silica type AR974, b) for AR805 and c) AR974 with compatibilizer, while stress at break (σ_B) and strain (ε_B) at break at break values are depicted in Figure 5.15 and Figure 5.16 respectively.

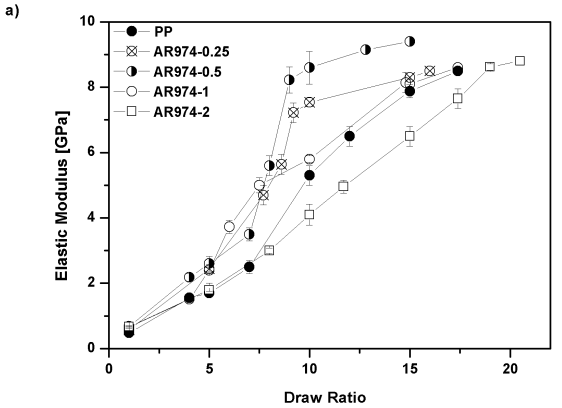

Figure 5.14a. Elastic modulus properties of neat and nanofilled PP-AR974 fibers for different draw ratio.

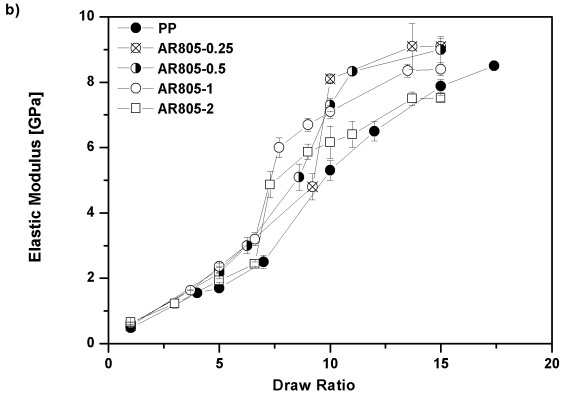

Figure 5.14b. Elastic modulus properties of neat and nanofilled PP-AR805 fibers for different draw ratio.

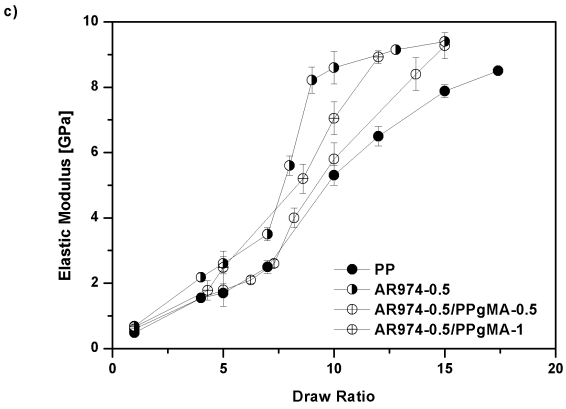

Figure 5.14c. Elastic modulus properties of neat and nanofilled AR974-0.5 fibers with and without compatibilizer for different draw ratio.

It is evident that presence of fumed nanosilica particles improved stiffness of tested material, especially at higher draw ratio. If values at different draw ratio (DR=10 and DR=15) will be compared, it can be seen that elastic modulus increased from 5.3 GPa and 7.9 GPa for neat PP up to 7.5 GPa and 8.3 GPa for compositions with 0.25%vol of fumed nanosilica and 8.6 GPa and 9.4 GPa with 0.5%vol of AR974. For nanosilica type AR805 compared values were equal 8.1 GPa and 9.1 GPa for AR974-0.25 and 7.3 GPa and 9.0 GPa for AR805-0.5. The improvement of around 40-55% was observed for both type of silica drawn fibers with DR=10 in comparison to neat PP. With a higher drawing (DR=15) enhancement decreased and reached values from 5% up to 20% for AR974 and from 7 up to 15% for AR805. In this study high improvement (up to 55%) was obtained at very low nanofiller loading of 0.25-0.5% vol for medium draw ratio (DR=10). The negative effect of high concentration of both nanosilica type (2% vol.), especially more visible for higher draw ratio (DR>10), can be explained in terms of filler dispersion aspect observed also in SEM and TEM analysis. In the Figure 5.14c properties for the composition with and without compatibilizer were reported. It is well known that the main role of compatibilizer is deagglomeration of filler particles and uniform distribution of the particles in a viscous polymer matrix under shear stress [171]. However, we can observe lower

values of elastic modulus in comparison to the same composition without compatibilizer. It can be concluded that the addition of compatibilizer did not play a significant role in the stiffness enhancement.

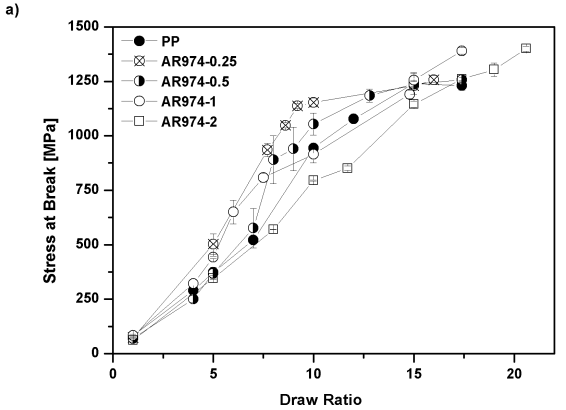

Figure 5.15a. Stress at break properties for neat and nanofilled PP-AR974 fibers for different draw ratio.

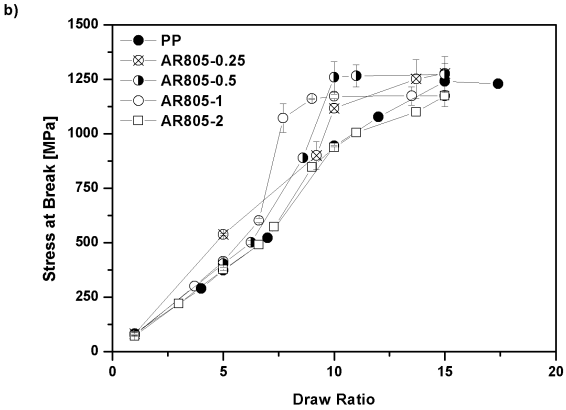

Figure 5.15b. Stress at break properties for neat and nanofilled PP-AR805 fibers for different draw ratio

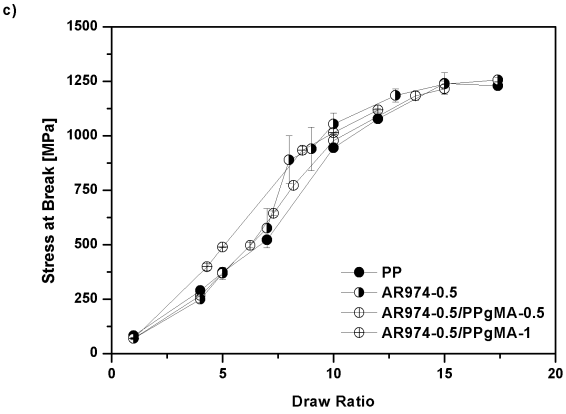

Figure 5.15c. Stress at break properties for neat and nanofilled AR974-0.5 fibers with and without compatibilizer for different draw ratio.

It is well known that the stress at break of compositions usually decreases with the addition of the nanofiller. In Fig. 5.15 a, b and c stress at break versus nanofiller volume fraction for different DR were plotted. In case of drawn PP-fumed nanosilica fibers higher values were obtained. If DR=10 will be taken as comparison point it can be observed that stress of about 1153 MPa for AR974-0.25 and 1054 MPa for AR974-0.5 while 944 MPa for neat PP were obtained. In case of fumed silica type AR805 the results were higher, at DR=10 stress at break for compositions with nanofiller content from 0.25% vol. up to 1% vol. were from 1117 MPa up to 1260 MPa. It can be noticed that for the compositions up to 0,5% vol of the fumed nanosilica for entire DR stress was higher in comparison to neat PP, while for nanofiller amount higher than 1% vol. obtained properties were slightly lower. It is known that in case of low nanofiller loading enhancement in tensile properties can be obtained because of better orientation of both silicate layers and molecular chain during fibers spinning [121]. Higher improvement in case of fibers with low nanofiller loadings (0.25-0.5% vol.) was also observed by Joshi and Viswanathan [145] in case of PP – Closite15A nanocomposites. This behavior might be due to the unavoidable aggregations of the silica layers at higher clay concentrations (>1% vol). The improvement in case of low nanofiller content was observed also by other

researchers [109, 145, 166]. Typically, fillers with very low aspect ratio like titanium or silicon dioxide have no positive effect on tensile property of the fiber. In this case, change in silica morphology occurring during spinning and drawing process played an important role in the enhancement of mechanical properties. The improvement was explained by Joshi [109] on the basis of modified clay platelets reinforcing the PP matrix at nanolevel due to nanodispersion resulting in combination of intercalated and exfoliated structure. The formation of intercalated/exfoliated structure is favored at higher temperature where the rate of crystallization is lower and the chain mobility is higher. Under this condition the polymer chain can diffuse into the interlayers of the clays. Processing condition, melt spinning at 230°C and drawing at 145°C, may favor intercalation and exfoliation of clay into the PP matrix. The surface area of dispersed clays increases with decrease in the particle size, what will result increase of volume fraction of the interfacial regions and helps in better stress transfer.

For the comparison in Figure 5.15c stress at break values versus draw ratio were plotted for the composition AR974-0.5 with and without compatibilizer. It can be seen that for low DR up to 10 higher stress at break was observed for the compositions with 1% vol. of Fusabond F613, while with further drawing process this difference become less significant and for fibers with DR≥10 stress at break had almost the same values for the compositions with and without compatibilizer.

It is important to underline that the dispersion of fumed silica nanoparticles leads to an interesting increase both elastic modulus and stress at break for compositions with low nanofiller content. In case of strain at break slightly lower values were found for as-spun nanocomposites (Tab. 5.9) while after drawing process the difference between PP and nanofilled fibers decreased and for DR>10 the values were almost identical. In Figure 5.15c strain at break properties for the compositions with and without compatibilizer were depicted. As it was already mentioned before for as-spun fibers slightly higher values were obtained for the compositions with compatibilizer, while with drawing process this differences becomes less significant and for fibers with DR≥10 the values were the same. It can be concluded that in case of strain at break there is no significant influence of the compatibilizer on the elongation of the material especially for drawn fibers.

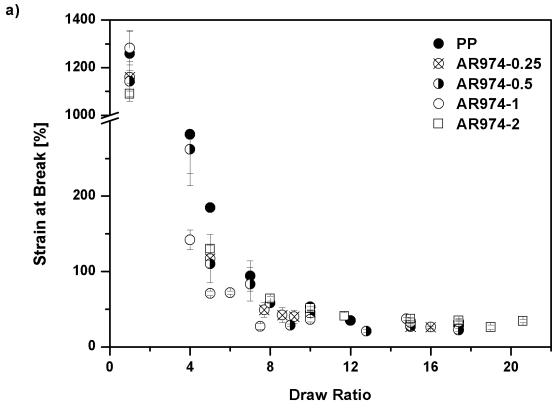

Figure 5.16a. Strain at break properties for neat and nanofilled PP-AR974 fibers for different draw ratio.

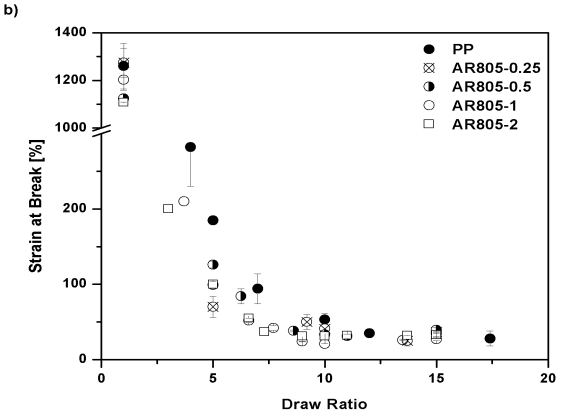

Figure 5.16b. Strain at break properties for neat and nanofilled PP-AR805 fibers for different draw ratio.

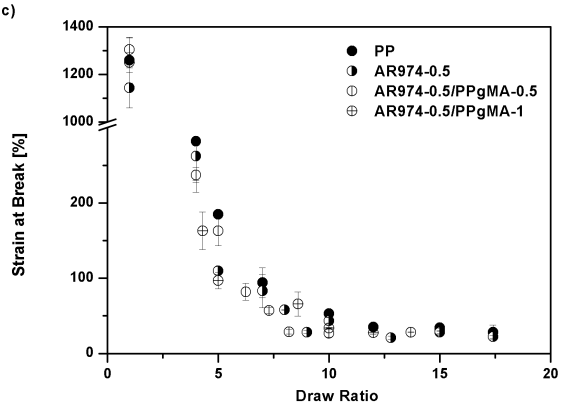

Figure 5.16c. Strain at break properties for neat and nanofilled AR974-0.5 fibers with and without compatibilizer for different draw ratio.

The toughening effect observed for fumed silica nanoparticles is very particular and interesting result because most of the time the stiffening effect was accompanied by reduction of the tensile strain at break, what was the most undesirable effect due to the introduction of nanofiller.

It can be concluded that the improvement in modulus observed together with enhancement in stress at break was obtained without affecting strain at break properties. For both of the nanosilica type the obtained results were very similar, however slightly higher modulus related to the higher surface area of PP-AR974 was observed. This kind of behavior is in agreement with previous reports about nanosilica composites where better mechanical properties were achieved through good dispersion of silica aggregates that are responsible for a further improvement of mechanical properties [82, 90, 103].

For PP fibers with different volume fraction of nanosilica, the enhancement of relative elastic modulus (REM) was calculated according to equation 4.1, and presented in the Figure 5.17 a) and b).

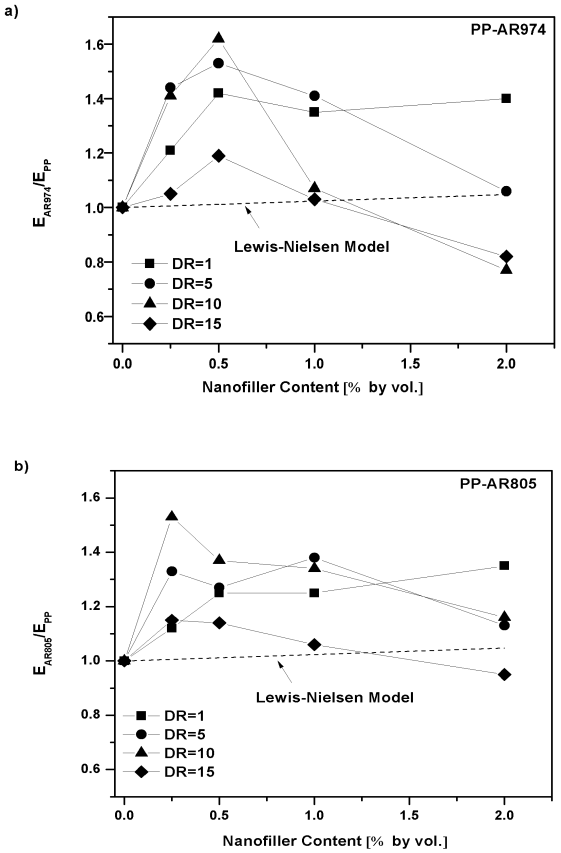

Figure 5.17. Relative elastic modulus of (a) PP-AR974 and (b) PP-AR805 nanocomposites fibers with different draw ratios as a function of nanofiller content.

The Figure 5.17 a and b depicted a significant effect of the fumed silica content on the Young's modulus of the nanocomposites. It can be observed that the relative elastic modulus was increasing up to compositions containing 1% vol. of the both types of the nanosilica, while the highest improvement was obtained for compositions AR974-0.5 and AR805-0.25. Moreover, the significant enhancement of the modulus can be observed up to DR=10, while for further drawing process, values decreased.

The stiffening effect provided by fumed silica nanoparticles can by modeled by considering the theoretical approaches developed for traditional microcomposites. In particular the elastic modulus can be represented by the modified Kerner equation proposed by Lewis and Nielsen [155] (equation 5.2).

In Fig.5.17a and b the experimental data for as-spun and for drawn fibers were compared with theoretical previsions. It can be observed that obtained relative elastic modulus was much higher than predicted by Lewis-Nielsen equation. This is probably related to the fact that model did not take into account the filler-matrix interaction that is very significant in case of drawn material.

It is well known that there are two parameters that affect the mechanical properties of the fibers, which are extent of exfoliation and the degree of crystallinity [121, 124]. In Figure 5.18a and 5.18b elastic modulus versus crystallinity content was plotted.

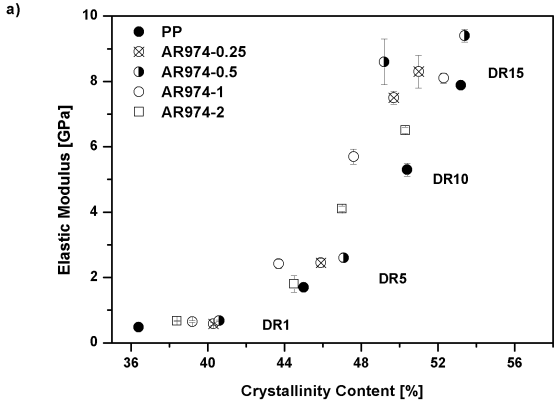

Figure 5.18a. Elastic modulus of neat and PP-AR974 fibers as a function of degree of polymer crystallinity.

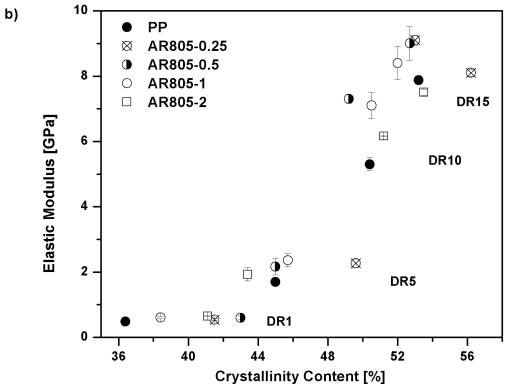

Figure 5.18b. Elastic modulus of neat and PP-AR805 fibers as a function of degree of polymer crystallinity.

As it was already mentioned before, crystallinity content for the as-spun fibers containing nanofiller was higher than for neat PP. However, it was observed that with DR>10 crystallinity content increases significantly only for compositions with low nanofiller content. For composition with 2% vol. significantly lower modulus together with crystallinity content was obtained. It can be noted that for other compositions with the crystallinity content elastic modulus increased, and the highest values were obtained for the AR974-0.5. This behaviour suggests that the improvement in mechanical properties is related to differences in polymer orientation which intimately relates to differences on degree of crystallinity and morphology developed during drawing [124],[128].

Some more information about spinnability and drawability could be obtained considering the mechanical draw ratio (λ_{MEC}) Eq.4.2, the true strength (σ^*_{MAX}) Eq.4.3 the processing draw ratio (λ_{PRO}) Eq. 4.6, and the total draw ratio (λ_{TOT}) Eq. 4.7 of selected fibers and compared in Table 5.10a and b.

For the as-spun fibers, higher true strength value was obtained for the neat PP. For example, the true strength of PP as-spun fibers was equal σ_{MAX}=1123 MPa and total draw ratio λ_{TOT}=148, whereas the correspondent values of the nanofilled PP as-spun fibers were between 737-1147 MPa for AR974 silica type and 870-1127 MPa for

AR805. In case of total draw ratios values were from 129 up to 150 for PP-AR974 and from 131 up to 150 for PP-AR805 as-spun fibers. It can be said that for most of the nanofilled fibers compositions slightly lower values were obtained, while for AR974-1 and AR805-0.25 the calculated values were slightly higher.

In the case of drawn fibers, true strength and mechanical draw ratio were very similar for both neat and nanofilled PP fibers. Also the total draw ratio indicates that fiber reinforced by fumed nanosilica could be spun and drawn at the same levels as PP fiber, confirming the good processability of fumed silica nanocomposites.

Moreover, a quantitative evaluation of the fiber properties and drawability of each composition could be remarked considering the draw-stiffening factor, calculated as the ratio between modulus of drawn fiber and modulus of as spun fiber, also reported in Table 5.10a and b. These values are directly dependent on the draw ratio, and the higher draw-stiffening factor of the PP fiber containing 0.25-0.5% of fumed silica AR974 and 0.25-1% of AR805 with respect to the neat PP fiber up to DR10 is well evident. Slightly lower values for 2% vol. of both types of the filler were observed.

Material	DR	Linear density[a] [tex]	Elastic modulus [GPa]	Stress at break [MPa]	Strain at break [%]	Tenacity[a] [cN/tex]	Calculated max. strength[b] σ_{MAX} [MPa]	Mechanical draw ratio λ_{MEC}	Total draw ratio λ_{TOT}	Relative stiffening factor
PP	1	178.3	0.48±0.01	83±4	1260±15	9.1	1123	13.6	148.1	1.0
	5	36.6	1.71±0.15	374±13	185±11	40.6	1066	2.85	153.3	3.6
	10	17.5	5.30±0.15	944±25	53±5	101.7	1444	1.53	173.4	11.0
	15	12.4	7.88±0.35	1240±50	34±3	133.0	1661	1.34	215.8	16.4
AR974-0.25	1	179.4	0.58±0.01	74±3	1160±45	8.1	870	12.4	135.5	1.0
	5	36.6	2.45±0.11	503±16	117±5	54.5	769	2.10	112.4	4.2
	10	17.5	7.50±0.20	1153±30	46±2	124.3	1507	1.43	162.0	13.0
	15	12.3	8.30±0.50	1230±13	36±4	132.3	1583	1.28	206.2	14.3
AR974-0.5	1	179.1	0.68±0.02	69±4	1144±55	7.5	932	12.6	137.2	1.0
	5	36.5	2.62±0.17	368±10	109±10	39.8	1091	2.17	116.7	3.9
	10	17.4	8.62±0.55	1054±45	43±6	113.7	1683	1.46	165.4	12.7
	15	12.4	9.41±0.25	1237±25	28±6	132.6	1673	1.36	219.1	13.8
AR974-1	1	179.1	0.65±0.01	83±2	1282±35	9.1	1147	13.8	150.5	1.0
	5	36.5	2.41±0.13	442±25	71±14	48.1	755	1.71	92.0	3.7
	10	17.4	5.70±0.45	915±45	36±12	99.0	1244	1.36	154.1	8.8
	15	12.3	8.10±0.35	1256±50	32±8	134.9	1658	1.32	212.6	12.5
AR974-2	1	178.8	0.67±0.02	62±2	1089±58	6.8	737	12.0	129.5	1.0
	5	36.6	1.81±0.16	346±17	129±13	37.6	792	2.30	123.1	2.7
	10	17.4	4.10±0.45	795±18	51±10	86.1	1153	1.45	164.3	6.1
	15	12.3	6.50±0.40	1145±38	37±5	123.3	1568	1.37	220.7	9.7

Table 5.10a. Selected mechanical properties of neat PP and nanofilled PP-AR974 fibers at various draw ratio (DR).

Material	DR	Linear density[a] [tex]	Elastic modulus [GPa]	Stress at break [MPa]	Strain at break [%]	Tenacity[a] [cN/tex]	Calculated max. strength[b] σ_{MAX} [MPa]	Mechanical draw ratio λ_{MEC}	Total draw ratio λ_{TOT}	Relative stiffening factor
AR805-0.25	1	179.7	0.54±0.01	82±2	1275±55	9.0	1127	13.7	149.7	1.0
	5	36.8	2.27±0.15	538±14	70±10	58.0	914	1.70	91.4	4.2
	10	176.7	8.10±0.17	1117±25	41±3	119.2	1575	1.41	159.7	15.0
	15	12.4	9.10±0.52	1277±11	36±4	137.0	1737	1.36	219.1	17.0
AR805-0.5	1	180.1	0.60±0.01	78±3	1125±45	8.5	955	12.2	133.4	1.0
	5	36.6	2.16±0.14	404±11	126±13	43.9	913	2.26	121.5	3.6
	10	17.5	7.30±0.50	1260±25	39±5	135.9	1751	1.39	157.5	12.2
	15	12.4	9.00±0.35	1273±20	33±4	136.6	1693	1.33	214.2	15.0
AR805-1	1	178.8	0.61±0.01	76±2	1282±25	8.3	990	13.0	142.0	1.0
	5	36.6	2.36±0.15	414±20	71±13	44.9	824	2.00	107.0	3.9
	10	17.5	7.10±0.35	1172±35	36±10	126.2	1418	1.21	137.1	11.6
	15	12.3	8.40±0.24	1175±45	32±7	126.2	1492	1.27	204.6	13.8
AR805-2	1	179.6	0.65±0.02	72±2	1108±40	7.9	870	12.1	131.5	1.0
	5	36.5	1.93±0.12	376±15	100±12	40.9	752	2.00	107.6	3.0
	10	17.5	6.16±0.65	936±10	33±11	100.7	1245	1.33	150.7	9.5
	15	12.4	7.51±0.30	1175±40	31±3	125.9	1539	1.31	211.0	11.6

Table 5.10b. Selected mechanical properties of neat PP and nanofilled PP-AR805 fibers at various draw ratio (DR).

Maximum attainable mechanical properties can be predicted by the intercept of the straight lines fitting the experimental values of modulus with the 1/DR according to equation 4.8.

Following this equation maximum attainable elastic modulus and stress at break can be predicted and the results for compositions with fumed nanosilica type AR974 are depicted in Figure 5.19 and 5.20 and summarized in Table 5.11.

Material	E^a_{max} [GPa]	σ^a_{bmax} [MPa]
PP	9.6±0.7	1492±104
AR974-0.25	11.5±0.6	1655±64
AR974-0.5	12.2±1.1	1584±73
AR974-1	10.4±0.4	1574±70
AR974-2	10.±0.8	1604±104
AR805-0.25	12.5±1.4	1633±85
AR805-0.5	12.7±1.0	1884±160
AR805-1	10.5±0.2	1594±123
AR805-2	8.6±0.3	1267±109

Table 5.11. Maximum attainable theoretical values of elastic modulus and stress at break of neat PP and fumed silica nanocomposite fibers.

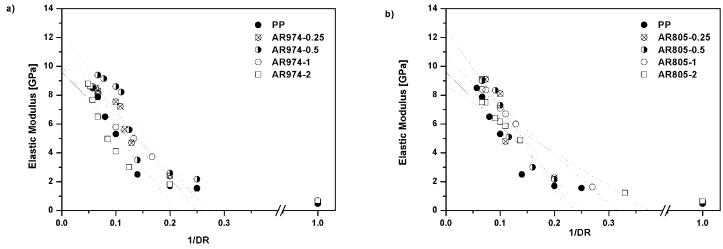

Figure 5.19. Extrapolated elastic modulus values versus 1/DR for neat and nanofilled PP-AR974 fibers.

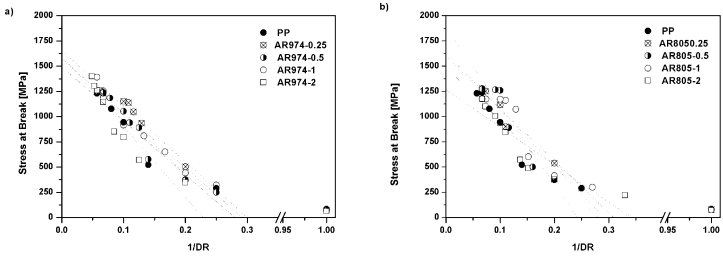

Figure 5.20. Extrapolated stress at break values versus 1/DR for neat and nanofilled PP-AR805 fibers.

It can be observed that theoretical attainable elastic modulus for all the nanocomposites were higher than for neat PP. The highest values were obtained in case of composition with AR974 for composition with 0.5% vol. (12.2 GPa) and 0.25% vol. (11.5 GPa). In case of silica type AR805 the highest attainable modulus was observed for compositions with 0.25% vol (12.5 GPa) and 0.5% vol (12.7GPa), while for AR805-2 values were slightly lower in comparison to neat PP. In case of stress at break, for all the nanocomposites fibers higher values were predicted by fitting. The highest stresses were obtained for compositions with 0.25% vol of AR974 (1655M Pa) and 2% vol. (1604 MPa) and for AR805 for compositions with 0.25% vol. (1633 MPa) and 0.5% vol (1884 MPa) in comparison to 1492 MPa for neat PP. However, big reduction of the stress at break was observed for the composition AR805-2 (1267 MPa), what is probably related to the not homogenous nanofiller dispersion.

5.2.5. DMTA analysis

In order to evaluate the effect of the SiO_2 nanoparticles into the PP matrix, thermomechanical properties were evaluated. Due to the very high surface area of the nanoparticles in the PP-AR974/AR805 nanocomposites, the applied stress are expected to be easy transferred from the matrix onto the silica particles, resulting in an enhancement of the mechanical properties. In Figure 5.21 and 5.22 storage modulus and tan delta values derived from dynamic mechanical analysis of neat and nanofilled PP fibers with different draw ratio are reported.

A marked rise in the storage moduli with the nanofiller content for DR=1 can be observed (Fig. 5.21.a and 5.22.a). The highest improvement was obtained for AR974/AR805-2. However, for drawn fibers the best enhancement was observed for compositions with low nanofiller content 0.25 and 0.5% vol. while for 2% vol. the modulus was lower even than that for neat PP. Similar behavior, as improvement for compositions with low nanofiller content was observed by Joshi [145]. This enhancement in the storage modulus may be related to the immobilized or restricted mobility in the interphase regions caused by clay-polymer interaction. Moreover, obtained results are in agreement with mechanical properties of the corresponding samples where a maximum values for low nanofiller content in tensile modulus were also recorded. The physical polymer-filler interaction due to the presence of hydrogen bonds at the composite interface hinders the molecular chain mobility around the nanoparticles, and the larger availability of hydroxyl groups for high surface area nanoparticles leads to a more effective block of segmental motion of the macromolecular. This is a proof that thermomechanical as well as mechanical properties of nanocomposites could be higher if nanoparticles were more finely dispersed into the polymer matrix.

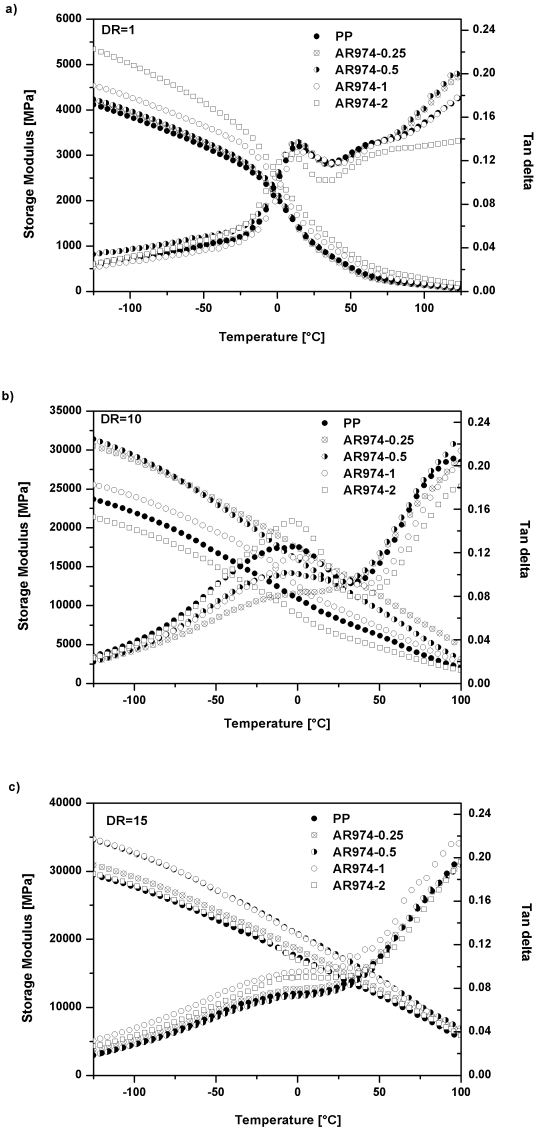

Figure 5.21 Storage modulus and tan delta of neat and nanofilled PP-AR974 fibers with different draw ratios (a) DR=1, (b) DR=10 and (c) DR=15.

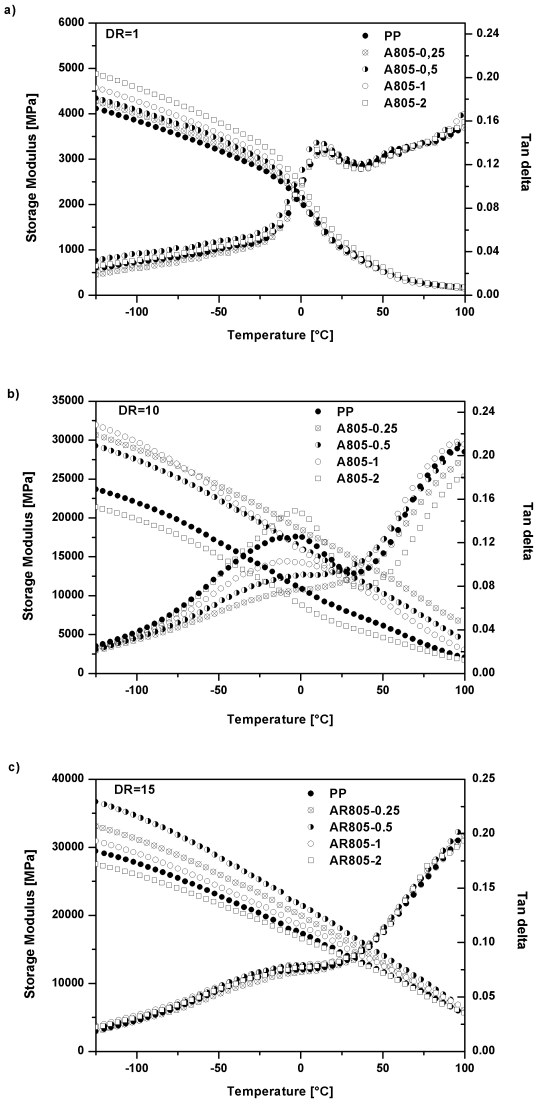

Figure 5.22 Storage modulus and tan delta of neat and nanofilled PP-AR805 fibers with different draw ratios (a) DR=1, (b) DR=10 and (c) DR=15.

In the Fig. 5.23 and 5.24 loss modulus for all of the compositions with different draw ratio were potted while some relevant values were summarized in Table 5.12.

Polypropylene exhibits three relaxations localized in the range of -80°C (γ), 10°C (β) and 100°C (α). For as-spun PP one relaxation peak at 5.6°C was observed, identified as β-relaxation, while for drawn fibers new peak at 69°C related to α-relaxation starts to be visible and with increasing nanoparticle content the α-relaxation shifts to higher temperatures. The β-relaxation corresponds to the T_g of PP, and does not change significantly with varying nanoparticle content; only for AR974-2 lower values were observed. However, after drawing process T_g shifted to lower temperature values, from 6.1°C for neat as-spun PP up to -28°C for DR=10 and -25°C for DR=15. Moreover with the nanofiller content T_g temperature increased, for DR=10 from -28°C for neat PP up to -17.0°C and for DR=15 up to -12.4°C for AR974-1. For PP-AR805 T_g increased for DR=10 up to -22°C and for DR=15 up to -21°C. According to Vladimirov at al. [163] shift of T_g to higher temperatures is due to the interactions between polymer chains and nanoparticles. In our case, this interaction was more efficient after drawing process that causes better distribution of the nanoparticles inside the matrix. Moreover, higher T_g temperatures were obtained for AR974 with higher surface area where better interaction was expected. It can be observed that with drawing process loss modulus peak was lowering and broadening. Some authors explain this behaviour as an indication of the greater constraints on the relaxation of the amorphous phase and thereby improvement in the mechanical properties [138].

The ratio of loss modulus to storage modulus is measured as mechanical loss factor or tan δ. The variation of tan δ as a function of temperature is represented in the Figure 5.21 and 5.22. The broadening of tan δ peak can be observed with drawing process. This behavior is probably related to the restriction of the mobility of the chain of the matrix polymer [138].

Material	T_g [°C]	E'_{glass} [GPa]	$E'_{rubbery}$ [GPa]	S*	T_g [°C]	E'_{glassy} [GPa]	$E'_{rubbery}$ [GPa]	S*
DR=1								
PP	6.1	2.89	0.15	18.7	-	-	-	-
AR974/805-0.25	6.1	2.93	0.13	20.6	5.9	2.98	0.15	18.5
AR974/805-0.5	5.3	3.02	0.12	23.2	5.2	3.12	0.15	19.7
AR974/805-1	6.2	3.37	0.17	19.2	5.2	3.22	0.14	20.9
AR974/805-2	-1.0	3.73	0.27	12.7	5.6	3.45	0.17	19.2
DR=10								
PP	-28.5	16.6	2.10	6.00	-	-	-	-
AR974/805-0.25	-21.8	21.2	5.40	2.92	-23.5	22.0	6.87	2.20
AR974/805-0.5	-28.3	20.4	3.41	4.98	-28.3	19.9	4.61	3.32
AR974/805-1	-17.0	17.3	3.01	4.76	-27.5	20.4	2.98	5.87
AR974/805-2	-21.8	12.7	1.68	6.56	-21.8	12.8	1.68	6.66
DR=15								
PP	-25.0	20.6	5.54	2.72	-	-		-
AR974/805-0.25	-21.2	22.0	6.45	2.41	-21.7	23.9	6.52	2.66
AR974/805-0.5	-21.8	25.0	7.00	2.56	-20.7	25.9	6.84	2.79
AR974/805-1	-12.4	24.7	6.35	2.88	-21.0	21.9	6.88	2.20
AR974/805-2	-18.8	21.2	5.98	2.55	-21.4	19.8	6.11	2.24

Table 5.12 Glass transition temperature (T_g), storage modulus at glassy and rubbery state and S* transition intensity of neat and nanofilled PP fibers.

In order to study the effect of the filler of composites the intensity of the transition (S*) was calculated according to the equation 4.9 and the data are reported in Table 5.12 [131]. A higher intensity of transition (*S**) refers to the higher mobility and content of amorphous phase. In case of as-spun material higher S* values for AR974/AR805 were obtained for all of the compositions with the exception of AR974 with 2% vol of. However, for drawn fibers (DR=10 and 15) values were lower than for neat PP, only for AR974/805-2 for DR=10 and AR974-1 for DR=15 the values were higher. This means that after drawing process the mobility of the macromolecular chains was suspended what indicates a stiffening effect provided by the nanofillers.

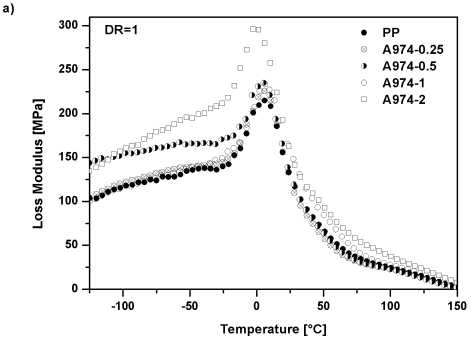

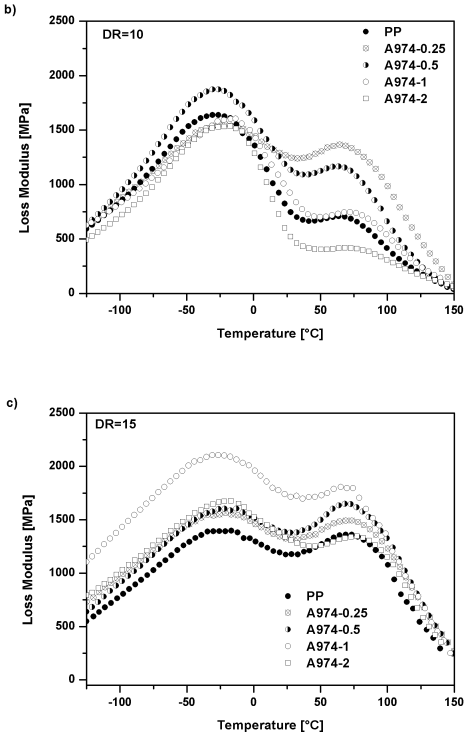

Figure 5.23. Loss modulus of neat and nanofilled PP-AR974 fibers with different draw ratios (a) DR=1, (b) DR=10 and (c) DR=15

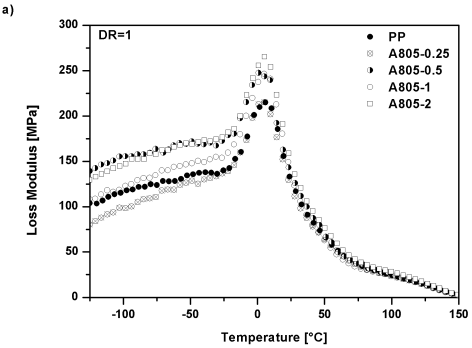

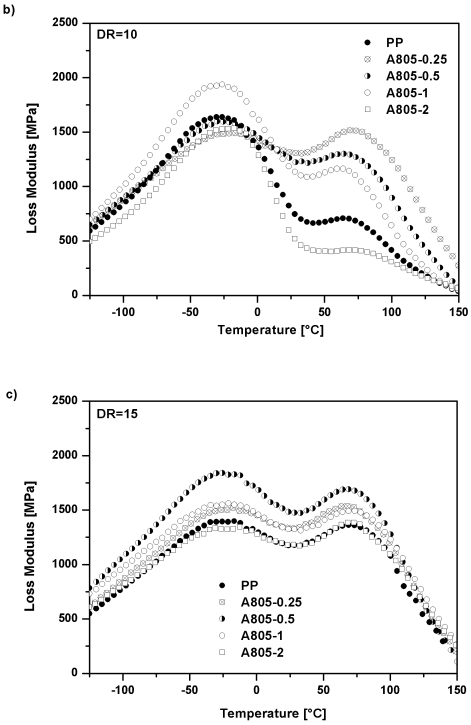

Figure 5.24. Loss modulus of neat and nanofilled PP-AR805 fibers with different draw ratios (a) DR=1, (b) DR=10 and (c) DR=15

5.2.6. Creep test

The creep tests were carried out in order to determine the deformation behavior of the material under a constant load. In this experiment a constant stress σ_0 equal 3MPa was applied to a sample and the strain was monitored as a function of time. In Figure 5.25 and 5.26 isothermal creep compliance curves for neat and nanocomposite polypropylene fibers for various draw ratios under a constant load of 3MPa for 3600s, is reported. Several mechanical models, representing response of a viscoelastic material under creep condition have been developed. Among various models, Burgers model described by eq. 4.13 was applied for our material. The

creep compliance curves of PP and fumed nanosilica composites at different draw ratio are compared in Figure 5.25 and 5.26 with the fitted data according to the Burgers model [143].

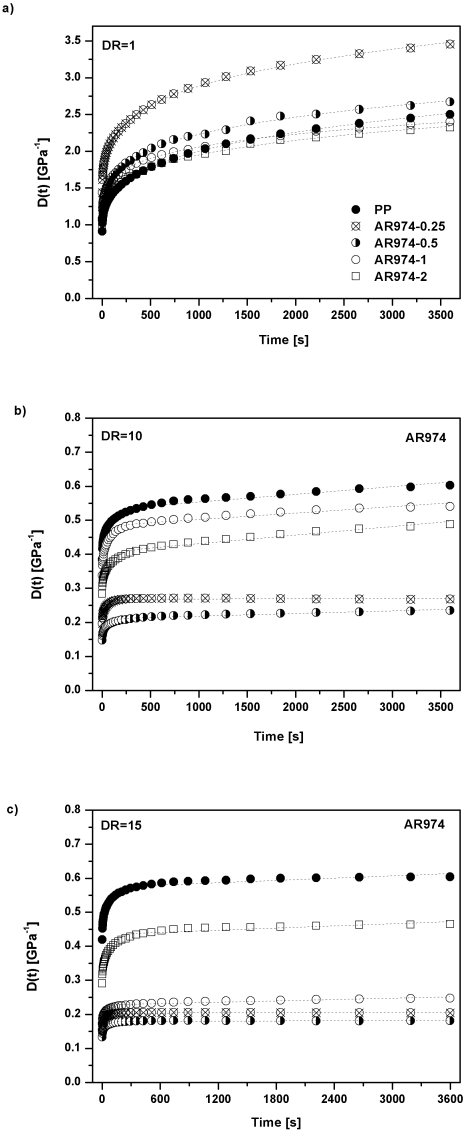

Figure 5.25 Creep compliance curve of neat and nanofilled PP-AR974 fibers at different draw ratio (a) DR=1, (b) DR=10 and (c) DR=15.

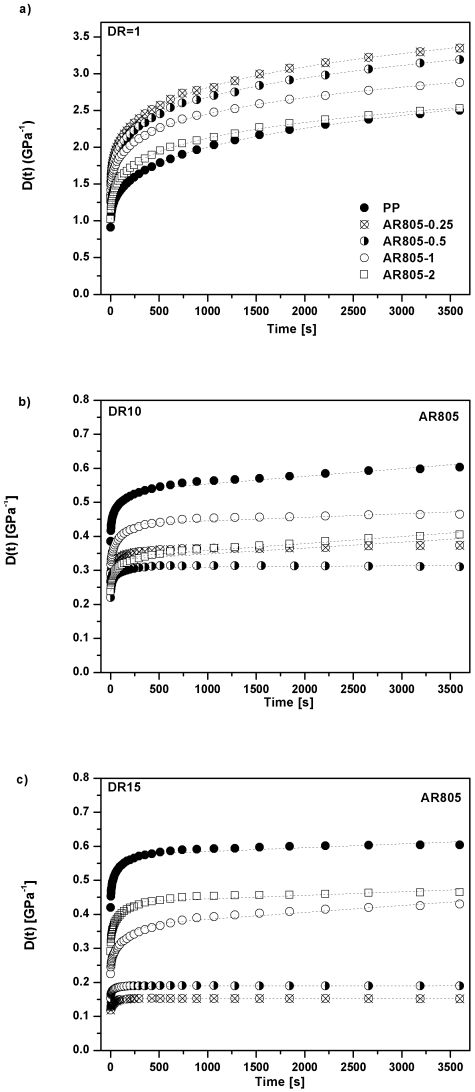

Figure 5.26. Creep compliance curve of neat and nanofilled PP-AR805 fibers at different draw ratio (a) DR=1, (b) DR=10 and (c) DR=15.

Material	E_M [MPa]	η_K [GPa·s]	E_K [MPa]	η_M [GPa·s]	R^2
DR=1					
PP	0.925±0.003	4524±230	1.449±0.036	284±25	0.987
AR974-0.25	0.590±0.005	3831±240	1.091±0.051	197±25	0.982
AR974-0.5	0.793 ±0.003	4840±186	1.351±0.040	221±22	0.983
AR974-1	0.993±0.002	5917±139	1.694±0.042	294±17	0.981
AR974-2	0.981±0.003	5701±160	1.562±0.034	358±22	0.981
AR805-0.25	0.626±0.004	3885±220	1.086±0.046	162±20	0.982
AR805-0.5	0.644±0.004	4120±201	1.176±0.042	176±20	0.983
AR805-1	0.680±0.003	4477±180	1.333±0.037	201±19	0.982
AR805-2	0.825±0.003	4138±166	1.450±0.035	218±19	0.982
DR=10					
PP	2.38±0.40	44326±236	9.09±0.1	684±10	0.972
AR974-0.25	4.81±0.15	310560±790	16.66±0.2	697±3	0.968
AR974-0.5	6.26±0.13	128040±932	20.34±0.2	501±6	0.978
AR974-1	2.75±0.30	52994±189	11.33±0.5	1152±7	0.970
AR974-2	3.28±0.36	59572±189	10.21±0.4	846±10	0.981
AR805-0.25	10.13±0.32	57306±325	9.12±0.2	787±2	0.915
AR805-0.5	4.22±0.23	515198±123	14.28±0.3	684±6	0.956
AR805-1	3.18±0.31	95419±205	9.33±0.5	766±7	0.973
AR805-2	3.89±0.25	48309±404	12.5±0.4	1099±11	0.979
DR=15					
PP	2.21±0.45	89525±224	8.26±0.5	548±78	0.967
AR974-0.25	6.21±0.82	228832±404	23.80±0.2	704±27	0.964
AR974-0.5	7.04±0.78	1075268±561	27.03±0.2	1051±41	0.962
AR974-1	3.14±0.52	95419±205	8.62±0.4	689±86	0.973
AR974-2	5.46±0.62	115080±808	22.73±0.2	962±54	0.967
AR805-0.25	8.06±0.62	4284490±425	37.04±0.2	1203±36	0.957
AR805-0.5	6.33±0.63	2881844±404	33.33±0.2	1246±16	0.982
AR805-1	3.14±0.35	95328±205	8.60±0.2	688±26	0.973
AR805-2	3.89±0.43	149285±226	8.77±0.5	927±34	0.958

Table 5.13. Fitting parameters of the creep data of neat and nanofilled PP fumed silica fibers at different draw ratio, according to the Burgers model.

It is evidenced that the introduction of fumed silica nanoparticles leads to a significant improvement of the creep stability of the nanocomposites material. Even if at DR=1 the creep compliance of the nanocomposite fibers is higher than for the neat PP, with drawing process significant improvement can be observed for nanofilled fibers. It is worth to notice that for as-spun material the highest creep compliance was obtained for the compositions with low amount of nanosilica (0.25 and 0.5% vol.). However, also the best creep stability for high DR was observed for compositions with low nanofiller amount. It is interesting to evaluate the effect of the filler content on the creep behaviour of the composites. In Fig. 5.27a and b the relative creep compliance values at 2000s are depicted.

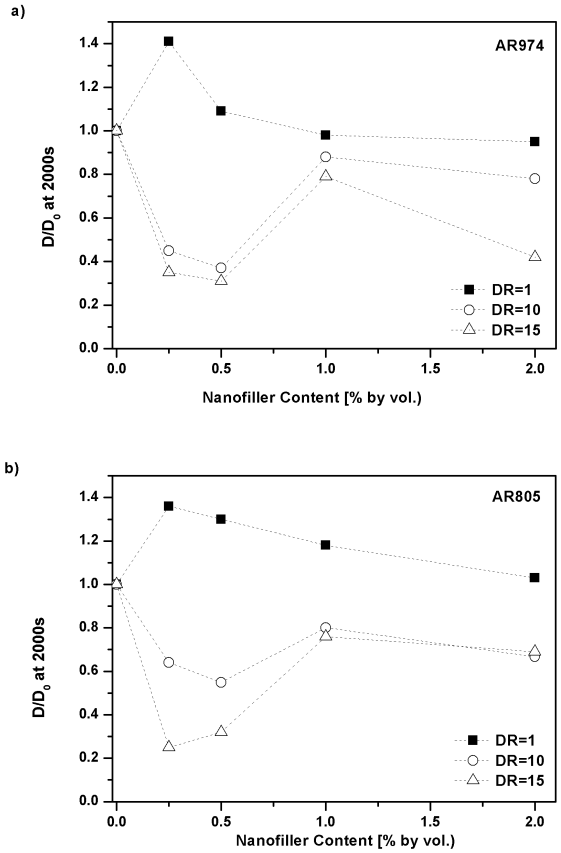

Figure 5.27. Relative creep compliance at 2000s of neat and nanofilled PP fibers with (a) AR974 and (b) AR805 at different draw ratio.

In case of as-spun material the enhancement of the creep stability was only observed for compositions PP-AR974 with 1 and 2% vol. of the filler. This is probably related with better filler matrix interaction obtained for fumed silica AR974 characterized by higher surface area than silica AR805. However, it is evident that the creep compliance of the composites decreases for drawn fibers with low nanofiller content. This effect is comparable to that observed in case of elastic modulus, that the behaviour of the material is mainly governed by the good filler distribution which is improved during drawing process.

Similar results were already reported by Dorigato for PE-different fumed nanosilica type nanocomposites [104] and D'Amato in case of HDPE-AR974 high performance nanocomposites fibers [82]. In this work obtained improvement was related to the fact that intercalation of nanoparticles may effectively reduce the polymer chain motion, affecting the stress transfer at a nanoscale level, which has positive effect on the final creep stability of the composite material.

Creep behavior of PP and fumed nanosilica nanocomposites can be analyzed considering viscoelastic mechanical models available for thermoplastic materials. Among all of them, the most well-known is Burger (or four parameters) and fitting according to this model was used for our materials [83]. In the Table 5.13 parameters derived from the fitting are summarized. It can be observed that the increase in the draw ratio produces an increase in elastic (E_K, E_M) and viscous components (η_K η_M). Comparing fitting parameter of the neat and nanofilled PP fibers, the conclusion is that all the parameters elastic and viscous for drawn material are higher than obtained for neat PP. In particular much higher values were observed for viscous component of Maxwell element [η_M]. Similar behavior already reported in case of polyamide fibers was explained considering fact that η_M parameter rules the deformation behavior of the material for long creep time what gives more effective stabilizing effect provide by fumed silica at long testing time [85].

5.2.9. Summary PP-FS fibres

Fumed nanosilica Aerosil®AR974 and Aerosil®AR805 can be successfully produced by a combined melt-extrusion and hot-drawing process up to 1 % vol. clay loading. Difference between both silica types as higher surface area of AR974 and different type of surface modification causes better matrix filler interaction and slightly affected the thermal and mechanical properties for as-spun material. However, in case of drawn fibers where the interfacial adhesion was improved during drawing process the obtained results were very similar for both types of the FS filler. Both types of the PP-FS fibers can be drawn at high draw ratio (up to ~20). The incorporation of the nanoclay into the PP matrix, especially in the low percentage content, leads to the

improvement over a wide range of properties. The tested samples exhibited an enhancement in elastic modulus and stress at break, whereas no significant variations of deformation at break were observed. The thermal stability of composite fiber was higher in comparison to neat PP. The addition of low amount of nanoclay (0.25-1 % vol.) was found to be sufficient to improve the tensile mechanical properties.

Nanofilled PP fiber with 0.5% vol. of both type of FS with respect to the neat PP showed higher attainable modulus (about 12.2 and 12.7 GPa vs 9.6 GPa) and stress at break (1584 MPa and 1884 MPa vs 1492MPa) maintaining the draw ratio at the same level.

DMTA evidenced stiffening effect observed as higher storage modulus for the compositions with nanosilica particles especially at higher draw ratio. Creep test evidenced a reduction of creep compliance with respect to the neat PP fibers for drawn material.

The improvements in mechanical properties observed in nanofilled PP-FS fibers was attributed to the good dispersion of fumed nanosilica particles at a high draw ratio, which promotes molecular orientation and crystallization of the amorphous region

Chapter VI

GENERAL CONCLUSIONS

High density polyethylene and polypropylene and their composites with organically modified hydrotalcite (LDH) and fumed nanosilica were successfully compounded by melt compounding and spun by combining melt-extrusion and hot-drawing process. In order to compare processing condition on the final properties of material, preliminary characterization was performed on the nanocomposites plates. Enhancement in thermal stability and elastic modulus together with good tensile properties at break were observed for both types of tested materials. However, the improvement was not satisfactory because of the presence of nanocomposites aggregates in the polymer matrix.

In order to improve the nanofiller distribution the same compositions were performed through two-step process; melt mixing and hot-drawing. The final material in form of thin fibers (final diameter ~100μm at DR=20) were thermo-mechanically tested and the following conclusions have been leaded:

- Presence of nanofiller does not affect the drawability and spinnability of the polymer matrix.
- Morphology and XRD analysis revealed a high degree of exfoliation of LDH in fibers containing 1-2 % by wt. of nanoclay, which was particularly evident after drawing. SEM and TEM analysis were performed for both type of nanofilled fibers and confirmed homogenous dispersion of the filler together with intercalation and partial exfoliation.
- In both cases the incorporation of clay into a polyolefin matrix enhanced its thermal stability by acting as a superior insulator and mass transport barrier to the volatile products generated during decomposition, making the diffusion path of the oxygen more tortuous, and thus retarding the thermo-oxidative process.

- The tensile modulus of nanofilled fibers rose with the nanofiller content and drawing ratio. In comparison to neat HDPE improvement of about 30% for LDH-1 with DR=10 in comparison to 9% for as-spun and 5% for melt compounded material was obtained. Similar behavior was observed in case of PP-fumed silica nanocomposites. Elastic modulus for composition with 0.5% vol. of silica type AR974 and AR805 increased of about 60% and 43% for fibers with DR=10, in comparison to 40% and 25% in case of as-spun material and only 3% and 1% for melt compounded plates. This positive effect was attributed to the good dispersion and alignment of nanoparticles induced during drawing process, which promotes molecular orientation and crystallization of the amorphous region.
- Moreover, tensile stress at break and strain at break of composite fibers approximately corresponded to those of the neat matrix.
- DMTA tests evidenced stiffening effect observed as higher storage modulus for the all compositions with nanoparticles especially at higher draw ratio.
- Creep tests evidenced a certain reduction of the creep compliance with respect to the neat fibers matrix over the whole range of investigated draw ratios and temperatures.
- The existence of an optimal amount of the nanofiller was observed. The critical concentration of nanofiller for fiber spinning was found at 2%. Above this concentration, both nanofiller types cannot be easily dispersed; clay will agglomerate in micrometric clusters acting as defects and stress concentration points that decrease drawability and polymer alignment.
- Considering the thermo-mechanical characterization of the several fibers compositions, both type of used nanocomposite showed the best balanced properties with 0.5-1% wt. of the filler.

Based on the studies it can be concluded that both type of used nanoparticles at higher draw ration effectively reinforced polyolefins matrix.

REFERENCES

1. Treloar, L.R.G., *Calculations of elastic moduli of polymer crystals: I. Polyethylene and nylon 66.* Polymer, 1960. **1**(0): p. 95-103.
2. White, J.L., K.C. Dharod, and E.S. Clark, *Interaction of melt spinning and drawing variables on the crystalline morphology and mechanical properties of high-density and low-density polyethylene fiber.* Journal of Applied Polymer Science, 1974. **18**(9): p. 2539-2568.
3. Andrews, J.M. and I.M. Ward, *The cold-drawing of high density polyethylene.* Journal of Materials Science, 1970. **5**(5): p. 411-417.
4. Capaccio, G. and I.M. Ward, *Preparation of ultra-high modulus linear polyethylenes; effect of molecular weight and molecular weight distribution on drawing behaviour and mechanical properties.* Polymer, 1974. **15**: p. 233-238.
5. Capaccio, G., T.A. Crompton, and I.M. Ward, *Ultra-high modulus polyethylene by high temperature drawing.* Polymer, 1976. **17**(644-645).
6. Vlasblom, M.P. and J.L.J. Van Dingenen, *The manufacture, properties and applications of high strength, high modulus polyethylene fibers.* at Bunsell, A. R., Schwartz P. "Handbook of Tensile Properties of Textile and Technical Fibres", Woodhead Publishing in Textiles, 2009: p. 437-485.
7. Ward, I.M. and P.J. Lemstra, *Production and properties of high -modulus and high-strength polyethylene fibers.* Kikutani, T., Jaffe, M., Hearle, J. W. S., Eichhor, S., at Handbook of textile fibre structure: Fundamentals and manufactured polymer fibres, Woodhead Publishing in Textiles, 2009. **I**: p. 352-393.
8. Capaccio, G. and I.M. Ward, *Effect of molecular weight on the morphology and drawing behaviour of melt crystallized linear polyethylene.* Polymer, 1975. **16**: p. 239-243.
9. Perkins, W.M., N.J. Capiati, and R.S. Porter, *The effect of molecular weight on the physical and mechanical properties of ultra-drawn high density polyethylene.* Polymer Engineering and Science, 1976. **16**: p. 200-203.
10. Smith, P. and P. Lemstra, *Ultra-high-strength polyethylene filaments by solution spinning / drawing.* Journal of Materials Science, 1980. **15**(2): p. 505-514.
11. Ward, I.M., *Developments in oriented polymers 1970–2004.* Plastics, Rubbers and Composites, 2004. **33**: p. 189-194.
12. Gupta, R.K., E. Kennel, and K.-J. Kim, *Polymer Nanocomposite Handbook.* Taylor and Francis Group, LLC, 2010: p. 22-44.
13. http://apps.webofknowledge.com/.
14. Zhang, M.Q., M.Z. Rong, and K. Friedrich, *Processing and properties of nanolayered nanoparticle reinforced thermoplastic composites* in Handbook of Organic-Inorganic Hybrid Materials and Nanocomposites, ed. Nalwa H.S. Amerrican Scientific Publishers, California, 2003. **II**: p. 113-150.

15. Mark, J.E., *Ceramic reinforced polymers and polymer-modified ceramics,*. Polymer Engineering & Science, 1996. **36**: p. 2905-2920.
16. Von Werne, T. and T.E. Patten, *Preparation of structurally well defined polymer-nanoparticle hybrids with controlled/ living radical polymerization.* Journal of the American Chemical Society, 1999. **121**: p. 7409-7410.
17. Herron, H. and D.L. Thorn, *Nanoparticles. Uses and relationships to molecular clusters.* Advanced Materials, 1998. **10**: p. 1173-1184.
18. Hedayati, M., et al., *Ball milling preparation and characterization of poly (ether ether ketone)/surface modified silica nanocomposite.* Powder Technology, 2011. **207**(1–3): p. 296-303.
19. In-Yup, J. and B. Jong-Beom, *Nanocomposites derived from polymers and inorganic nanoparticles.* Materials, 2010. **3**: p. 3654-3674.
20. Reedy, C.S. and C.K.J. Das, *Polypropylene-nanosilica filled composites: Effects of epoxy-resin-grafted nanosilica on the structural, thermal and dynamical mechanical properties.* Journal of Applied Polymer Science, 2006. **102**: p. 2117-2124.
21. Han, K. and M. Yu, *Study of the preparation and properties of UV-blocking fabrics of a PET/TiO_2 nanocomposites prepared by in situ polycondensation.* Journal of Applied Polymer Science, 2006. **100** p.1588-1593.
22. Chae, D.W. and B.C. Kim, *Characterization of polystyren/zinc oxide nanocomposite prepared from solution mixing.* Polymers for Advanced Technologies, 2005. **16**: p. 846-850.
23. Nielsen, L., *Models for permeability of filled polymer systems.* Journal of Macromolecular Science and Chemistry, 1967: p. 929-942.
24. Blumstein, A., *Polymerization of adsorbed monolayer II. Thermal degradation of the inserted polymer* Journal of Polymer Science: Part A: Polymer Chemistry, 1965. **3**: p. 2665.
25. Wang, H., et al., *Transparent poly(methyl metacrylate)/silica/zirconia nanocomposites with excelent thermal stabilities.* Polymer Degradation and Stability, 2005. **87**: p. 319-327.
26. Du, L. and B. Qu, *Structural characterization and thermal oxidation properties of LLDPE/MgAl-LDH nanocomposites.* Journal of Materials Chemistry, 2006. **16**: p. 1549-1554.
27. Gilman, J.W., *Flammability and thermal stability studies of polymer layered-silicate clay/ nanocomposites.* Applied Clay Science, 1999. **15**: p. 31-49.
28. Song, L., et al., *Study on the properties of flame retardant polyurethane/organoclay nanocomposite.* Polymer Degradation and Stability, 2005. **87**: p. 111-116.
29. Paul, D.R. and L.M. Robeson, *Polymer nanotechnology: Nanocomposites.* Polymer, 2008. **49**(15): p. 3187-3204.
30. Sarwar, M.I., S. Zulfiqar, and Z. Ahmad, *Polyamide–silica nanocomposites: mechanical, morphological and thermomechanical investigations.* Polymer International, 2008. **57**(2): p. 292-296.
31. Zimmermann, L., et al., *High refractive index films of polymer nanocomposites.* Journal of Materials Resistance, 1993. **8**: p. 1742-1748.

32. Sinha Ray, S. and M. Okamoto, *Polymer/layered silicate nanocomposites: a review from preparation to processing.* Progress in Polymer Science, 2003. **28**(11): p. 1539-1641.
33. Ciardelli, F., et al., *Review Nanocomposites based on polyolefins and functional thermoplastic materials.* Polymer International, 2008. **57**: p. 805-836.
34. Alexandre, M. and P. Dubois, *Polymer-layered silicate nanocomposites: preparation, properties and uses of a new class of materials.* Materials Science and Engineering 2000. **28**: p. 1-63.
35. Causin, V., et al., *Crystallization behavior of isotactic polypropylene based nanocomposites.* Journal of Thermal Analysis and Calorimetry, 2007. **90**(3): p. 849-857.
36. Miyata, S., *Anion-exchange properties of hydrotalcite-like compounds.* Clays and Clay Minerals, 1983. **31**: p. 305-311.
37. López-Salinas, E., et al., *Structural characterization of synthetic Hydrotalcite-like* $[Mg_{1}\text{-}xGa_{x}(OH)_{2}](CO_{3})_{x/2}\cdot mH_{2}O$. Langmuir, 1997. **13**(17): p. 4748-4753.
38. Velu, S., et al., *Synthesis of new Sn-incorporated layered double hydroxides and their thermal evolution to mixed oxides.* Chemistry of Materials, 1999. **11**(8): p. 2163-2172.
39. Leroux, F. and J.-P. Besse, *Polymer interleaved layered double hydroxide: A new emerging class of nanocomposites.* Chemistry of Materials, 2001. **13**(10): p. 3507-3515.
40. Chen, W. and B. Qu, *Enhanced thermal and mechanical properties of poly(methyl acrylate)/ZnAl layered double hydroxide nanocomposites formed by in situ polymerisation.* Polymer Degradation and Stability, 2005. **90**(1): p. 162-166.
41. Chen, W., L. Feng, and B. Qu, *Preparation of nanocomposites by exfoliation of ZnAl layered double hydroxides in nonpolar LLDPE slution.* Chemistry of Materials, 2004. **16**(3): p. 368-370.
42. Ding, P. and B. Qu, *Synthesis and characterization of exfoliated polystyrene/ZnAl layered double hydroxide nanocomposite via emulsion polymerization.* Journal of Colloid and Interface Science, 2005. **291**(1): p. 13-18.
43. Li, B., et al., *Preparation of poly (methyl methacrylate)/LDH nanocomposite by exfoliation-adsorption process.* Colloid and Polymer Science, 2003. **281**(10): p. 998-1001.
44. Hsueh, H.-B. and C.-Y. Chen, *Preparation and properties of LDHs/polyimide nanocomposites.* Polymer, 2003. **44**(4): p. 1151-1161.
45. Zammarano, M., et al., *Delamination of organo-modified layered double hydroxides in polyamide 6 by melt processing.* Polymer, 2006. **47**(2): p. 652-662.
46. Costantino, U., et al., *New nanocomposites constituted of polyethylene and organically modified ZnAl-hydrotalcites.* Polymer Degradation and Stability, 2005. **90**: p. 586-590.
47. Itoh, T., et al., *The self-assembling properties of stearate ions in hydrotalcite clay composites.* Langmuir, 2003. **19**(22): p. 9120-9126.

48. Costa, F.R., et al., *Morphology and fracture behaviour of polyethylene/Mg–Al layered double hydroxide (LDH) nanocomposites.* European Polymer Journal, 2006. **42**: p. 2140-2152.
49. Costa, F.R., et al., *Nanocomposites based on polyethylene and Mg–Al layered double hydroxide. I. Synthesis and characterization.* Polymer 2005. **46**: p. 4447-4453.
50. Costa, F.R., et al., *Nanocomposites based on polyethylene and Mg–Al layered double hydroxide. Part II. Rheological characterization.* Polymer, 2006. **47**(5): p. 1649-1660.
51. Ding, P. and B. Qu, *Structure, thermal stability, and photocrosslinking characterization of HDPE/LDH nanocomposites synthesized by melt-intercalation.* Journal of Polymer Science Part B: Polymer Physics, 2006. **44**(21): p. 3165-3172.
52. Hasegawa, N. and A. Usuki, *Silicate layer exfoliation in polyolefin/clay nanocomposites based on maleic anhydride modified polyolefins and organophilic clay.* Journal of Applied Polymer Science, 2004. **93**(1): p. 464-470.
53. Koo, J.H., *An overview of nanoparticles.* at Polymer Nanocomposites. Processing, characterization and applications. The McGraw-Hill Companies, Inc., 2006.
54. Friedlander, S.K., *Synthesis of nanoparticles and their agglomerates: aerosol reactord.* R&D Status and Trends in Nanoparticles, Nanostructured Materials, and Nanodevices in the United States, ed. Siegel, R.W. Hu, E.and Roco, M.C., 1998: p. 83-88.
55. Barthel, H. and L.R. Weis, *Fumed silica -production, properties, and applications.* at Organosilicon Chemistry. ed. Auner, N. and Weis, J., 1996: p. 761-778.
56. Rauwendaal, C.H., *Polymer Extrusion.* Hanser Publishers, Munchen, 1986: p. 20-25.
57. Kruder, G.A., *Extrusion.* in "Encyclopedia of Polymer Science and Engineering ed. John Wiley & Sons Inc., New York, 1985: p. 571-631.
58. Amornsakchai, T., et al., *Development of high strength polyethylene fiber from local materials for ballistic application. in Thailand Materials Science and Technology Conference.* Klong Luang, Pathumthani, 2006.
59. White, J.L. and D.D. Choi, *Polyolefins: Processing, structure development and properties* ed. Hanser, Munich, 2005.
60. Wishman, M. and G.E. Hagler, *Polypropylene Fibers.* in "Handbook of Fiber Science and Technology. Fiber Chemistry ed. Lewin, P. and Pearce E. M. Marcel Dekker, New York, 1985. **1**: p. 371-497.
61. Beyreuther, R. and H. Brunig, *Dynamics of Fibre Formation and Processing.* ed. Springer, Berlin, 2007.
62. Dees, J.R. and J.E. Spruiell, *Structure development during melt spinning of linear polyethylene fibers.* Journal of Applied Polymer Science, 1974. **18**(4): p. 1053-1078.
63. Kikutani, T., *Structure development in synthetic fiber producton.* at Handbook of textile fibre structure. ed. Eichhorn, S.J., Hearle, J.W.S., Jaffe, M., and Kikutani, T. Woodhead Publishing in Textiles

2009: p. 157-180.
64. Ziabicki, A., *Orientation mechanisms in the development of high-performance fibers*, in *Orientational Phenomena in Polymers*, L. Myasnikova and V.A. Marikhin, Editors. 1993, Steinkopff. p. 1-7.
65. Peacock, A.J., *Handbook of Polyethylene. Structures, Properties and Applications.* Marrcel Dekker, Inc. New York, 2000: p. 27-42.
66. Kamamoto, T. and R.S. Porter, in Integration of Fundamental Polymer Science and Technology. ed. Kleintjens, L.A. and Lemstra, P.J. New York, Elsevier 1986: p. 168-177.
67. Graff, G., *Modern Plastics Encyclopedia* New York, McGraw-Hill, 1993: p. 209.
68. Wang, L.-H., R.S. Porter, and T. Kanamoto, Polymer Comunications, 1990. **31**: p. 457.
69. Kalb, B. and A.J. Pennings, *Maximum strength and drawing mechanism of hot drawn high molecular weight polyethylene.* Journal of Materials Science, 1980. **15**(10): p. 2584-2590.
70. Capaccio, G., T.A. Crompton, and I.M. Ward, *Drawing behavior of linear polyethylene. II. Effect of draw temperature and molecular weight on draw ratio and modulus.* Journal of Polymer Science: Polymer Physics Edition, 1980. **18**(2): p. 301-309.
71. Hallam, M.A., et al., *A study of the effect of molecular weight on the tensile strength of ultra-high modulus polyethylenes.* Journal of Materials Science, 1986. **21**(12): p. 4199-4205.
72. Penning, J.P., D.J. Dijkstra, and A.J. Pennings, *Tensile force at break of gel-spun/hot-drawn ultrahigh molecular weight polyethylene fibres.* Journal of Materials Science, 1991. **26**(17): p. 4721-4726.
73. Selikhova, V.I., et al., *Special melting behaviour of highly oriented polyethylene.* Polymer Science U.S.S.R., 1986. **28**(2): p. 378-385.
74. Harutun, G.K., *Handbook of polypropylene and polypropylene composites.* Marcel Dekker, New York, 1999.
75. Tonnaer, H., *New synthetic organoclays offer improved flame retardancy and gas barrier properties.* Plastics Additives & Compounding, 2009. **11**(3): p. 14-17.
76. http://www.polymerpds.akzonobel.com/.
77. https://www.aerosil.com.
78. Van Krevelen, D.W., *Properties of polymers* Third Edition, Amsterdam, The Netherlands 1990.
79. Nielsen, L.E., *Mechnical Properties of Polymers and Composites.* 2nd ed. Marcel Dekker, New York 1974.
80. Rangasamy, L., E. Shim, and B. Pourdeyhimi, *Structure and tensile properties of nanoclay– polypropylene fibers produced by melt spinning.* Journal of Applied Polymer Science, 2011. **121**: p. 410-419.
81. Guo, Z. and B. Hagström, *Preparation of polypropylene/nanoclay composite fibers.* Polymer Engineering & Science, 2013: p. n/a-n/a.
82. D'Amato, M., et al., *High performance polyethylene nanocomposite fibers.* eXPRESS Polymer Letters, 2012. **6**(12): p. 954-964.

83. Ramírez-Vargas, E., et al., *Structural characterization of LDPE/EVA blends containing nanoclay-flame retardant combinations.* Journal of Applied Polymer Science, 2012. **123**(2): p. 1125-1136.
84. Wang, Q., et al., *Polypropylene/layered double hydroxide nanocomposites.* Journal of Materials Chemistry, 2012. **22**: p. 19113-19121.
85. Marega, C., et al., *Perkalite as an innovative filler for isotactic polypropylene-based nanocomposites.* Journa of Nanoscience and Nanotechnology, 2009. **9**: p. 2704-2714.
86. Costa, F.R., et al., *LDH as nanofiller: Organic modification and dispersion in polymers.* Macromolecular Symposia, 2011. **301**: p. 46-54.
87. Lei, Y. and W. Qianghua, *Effects of an intercalating agent on the morphology and thermal and flame-retardant properties of low-density polyethylene/layered double hydroxide nanocomposites prepared by melt intercalation.* Journal of Applied Polymer Science, 2012. **123**: p. 316-323.
88. Bocchini, S., et al., *Influence of nanodispersed hydrotalcite on polypropylene photooxidation.* Macromolecular Nanotechnology, 2008. **44**: p. 3473-3481.
89. Kloprogge, J.T. and R.L. Frost, *Fourier transform infrared and raman spectroscopic study of the local structure of Mg-, Ni-, and Co-Hydrotalcites.* Journal of Solid State Chemistry, 1999. **146**: p. 506-515.
90. Kontou, E. and M. Niaounakis, *Thermo-mechanical properties of LLDPE/SiO_2 nanocomposites.* Polymer, 2006. **47**: p. 1267-1280.
91. McCrum, N.G., B.E. Ready, and G. Williams, *Anelastic and dielectric effects in polymeric solids.* Wiley, New York 1967; reprinted by Dover Publications, New York 1991.
92. Ciardelli, F., et al., *Nanocomposites based on polyolefins and functional thermoplastic materials.* Polymer International, 2008. **57**: p. 805-836.
93. Hippi, U., et al., *Compatibilization of polyethylene/aluminum hydroxide (PE/ATH) and polyethylene/magnesium hydroxide (PE/MH) composites with functionalized polyethylenes.* Polymer, 2003. **44**: p. 1193-1201.
94. Kolarik, J., et al., *High-density polyethylene/cycloolefin copolymer blends part I: phase structure, dynamic, mechanical tensile, and impact properties.* Polymer Engineering and Science, 2005. **45**: p. 817-826.
95. Tian, Y., et al., *Effect of the ethylene-acrylic acid melt index on the structural characteristics and properties of high-density polyethylene/layered double hydroxide nanocomposites prepared via the master-batch method.* Journal of Composite Materials, 2012. **0**: p. 1-12.
96. Wei, C. and Q. Baojun, *LLDPE/ZnAl LDH-exfoliated nanocomposites: effects of nanolayers on thermal and mechanical properties.* Journal of Materials Chemistry, 2004. **14**: p. 1705-1710.
97. Peng, D. and Q. Baojun, *Synthesis of exfoliated PP/LDH nanocomposites via melt-intercalation: structure, thermal properties, and photo-oxidative behavior in comparison with PP/MMT nanocomposites.* Polymer Engineering & Science, 2006: p. 1152-1159.

98. Costa, F.R., U. Wagenknecht, and G. Heinrich, *LDPE/Mg-Al layered double hydroxide nanocomposite: Thermal and flammability properties.* Polymer Degradation and Stability, 2007. **92**: p. 1813-1823.
99. Ke, Y.C. and P. Stroeve, *Polymer-layered silicate and silica nanocomposites.* Elsevier, Amsterdam 2005.
100. Deshmane, C., et al., *On striking variation in impact toughness of polyethylene-clay and polypropylene-clay nanocomposite systems: The effect of clay-polymer interaction.* Material Science & Engineering A, 2007. **458**: p. 150-157.
101. Marega, C., et al., *Reduction in tactoid size as a means for reinforcing high-density polyethylene/montmorillonite nanocomposites.* Journal of Applied Polymer Science, 2009. **113**(6): p. 3920-3928.
102. Xu, J.-T., Q. Wang, and Z.-Q. Fan, *Non-isothermal crystallization kinetics of exfoliated and intercalated polyethylene/montmorillonite nanocomposites prepared by in situ polymerization.* European Polymer Journal, 2005. **41**(12): p. 3011-3017.
103. Dorigato, A., M. D'Amato, and A. Pegoretti, *Thermo-mechanical properties of high density polyethylene – fumed silica nanocomposites: effect of filler surface area and treatment.* Journal of Polymer Research, 2012. **19**: p. 9889-9900.
104. Pegoretti, A., A. Dorigato, and A. Penati, *Tensile mechanical response of polyethylene – clay nanocomposites.* eXPRESS Polymer Letters 2007. **1**(3): p. 123-131.
105. Ahmed, S. and F.R. Jones, *A review of particulate reinforcement theories for polymer composites.* Journal of Materials Science, 1990. **25**(12): p. 4933-4942.
106. Marega, C., et al., *The effect of a synthetic double layer hydroxide on the rate of III phase transformation of poly(1-butene).* eXPRESS Polymer Letters, 2011. **5**(12): p. 1050-1061.
107. He, D. and B. Jiang, *The elastic modulus of filled polymer composites.* Journal of Applied Polymer Science, 1993. **49**: p. 617.
108. Mareri, P., et al., *Mechanical behaviour of polypropylene composites containing fine mineral filler: effect of filler surface treatment.* Composites Science and Technology, 1998. **58**: p. 747-752.
109. Joshi, M., A. Shaw, and B.S. Butola, *Studies on composite filaments from nanoclay reinforced polypropylene.* Fibers and Polymers, 2004. **5**(1): p. 59-67.
110. *ASTM D123-09 Standard terminology relating to textile.* 2009.
111. Dabrowska, I., et al., *Organically modified hydrotalcite for compounding and spinning of polyethylene nanocomposites.* eXPRESS Polymer Letters, 2013. **7**(11): p. 936-949.
112. Kissinger, H.E., J. Res. Natl. Bur. Stand., 1956. **57**: p. 217.
113. Hoffman, J. and R.L. Miller, *Kinetics of crystallization from the melt and chain folding in polyethylene fractions revisited: theory and experiment* Polymer, 1997. **33**: p. 3151.

114. Xiaolei, C., et al., *Nonisothermal crystallization kinetics of high-density polyethylene/barium sulfate nanocomposites.* Polymer Engineering and Science, 2009. **49**: p. 2342-2349.
115. Lonkar, S.P., et al., *Thermal, mechanical, and rheological characterization of polypropylene/layered double hydroxide nanocomposites.* Polymer Engineering and Science, 2012. **52**(9): p. 2006-2014.
116. Xiuqin, Z., et al., *Polypropylene/montmorillonite composites and their application in hybrid fiber preparation by melt-spinning.* Journal of Applied Polymer Science, 2004. **92**: p. 552–558.
117. Chantrasakul, S. and T. Amornsakchai, *High strength polyethylene fibers from high density polyethylene/organoclay composites.* Polymer Engineering and Science, 2007. **47**(6): p. 943-950.
118. Clements, J., G. Capaccio, and I.M. Ward, *Melting behavior of ultrahigh modulus linear polyethylene.* Journal of Polymer Science: Polymer Physics Edition, 1979. **17**(4): p. 693-703.
119. Jaffe, M., J.D. Menczel, and W.E. Bessey, *Fibers.* at Turi, E. A. Thermal characterization of polymeric materials, Second edition, Academic Press, San Diego
1981: p. 1767-1954.
120. La Mantia, F.P., R. Marino, and N. Tzankova Dintcheva, *Morphology modification of polyethylene/clay nanocomposite samples under convergent flow.* Macromolecular Materials and Engineering, 2009. **294**: p. 575-581.
121. Lee, S.H. and J.R. Youn, *Properties of polypropylene/layered-silicate nanocomposites and melt-spun fibers.* Journal of Applied Polymer Science, 2008. **109**(2): p. 1221-1231.
122. Soitong, T. and J. Pumchusak, *The relationship of crystallization behavior, mechanical properties, and morphology of polypropylene nanocomposite fibers.* Journal of Materials Science, 2011. **46**: p. 1697-1704.
123. Rattanawijan, W. and T. Amornsakchai, *Polyethylene composites. I. Composite fibers of high density polyethylene.* Journal of Applied Polymer Science, 2012. **124**: p. 501-509.
124. Sulong, A.B., et al., *Process optimization of melt spinning and mechanical strength enhancement of functionalized multi-walled carbon nanotubes reinforcing polyethylene fibers.* Composites Part B: Engineering, 2011. **42**(1): p. 11-17.
125. Lorenzi, D., et al., *Spinability of nanofilled polypropylene.* Macromolecular Symposia, 2011. **301**: p. 73-81.
126. La Mantia, F.P., et al., *Morphology and properties of polyethylene/clay nanocomposite drawn fibers.* Macromolecular Materials and Engineering, 2008. **293**(1): p. 83-91.
127. Dintcheva, N.T., R. Marino, and F.P. La Mantia, *The role of the matrix-filler affinity on morphology and properties of polyethylene/clay and polyethylene/compatibilizer/clay nanocomposites drawn fibers.* E-Polymers, 2009. **054**.

128. Bilotti, E., et al., *Synergistic reinforcement of highly oriented poly(propylene) tapes by sepiolite nanoclay.* Macromolecular Journals, 2010. **295**: p. 37-47.
129. Tomka, J.G., *Textile Fibres*, in *Comprehensive Polymer Science and Supplements*, G. Editor-in-Chief: Allen, Editor. 1989, Pergamon: Amsterdam. p. 487-510.
130. Fambri, L., S. Bragagna, and C. Migliaresi, *Biodegradable fibers of Poly-L,DL-lactide 70/30 produced by melt spinning.* Macromolecular Symposia, 2006. **234**: p. 20-25.
131. Fambri, L., K. Kesenci, and C. Migliaresi, *Characterization of modulus and glass transition phenomena in poly(L-lactide)/hydroxyapatite composites.* Polymer Composites, 2003. **24**(1): p. 100-108.
132. Capaccio, G. and I.M. Ward, *The drawing behavior of polyethylene copolymers.* Journal of Polymer Science: Polymer Physics Edition, 1984. **22**(3): p. 475-484.
133. Stadler, F.J., *Dynamic-mechanical behavior of polyethylenes and ethene/α-olefin-copolymers: Part II. α- and β-relaxation.* Korean Journal of Chemistry Engineering, 2011. **28**(3): p. 954-963.
134. Ardanuy, M., et al., *Structure and properties of polypropylene/hydrotalcite nanocomposites.* Polymer Composites, 2010. **31**(5): p. 870-878.
135. Passaglia, E., et al., *Modulated crosslinking of polyolefines through radical processes in the melt.* Macromolecular Materials and Engineering, 2004. **289**: p. 809-817.
136. Kline, D.E., J.A. Sauer, and A.E. Woodward, *Effect of branching on dynamic mechanical properties of polyethylene.* Journal of Polymer Science, 1956. **22**(102): p. 455-462.
137. Díez-Gutiérrez, S., et al., *Dynamic mechanical analysis of injection-moulded discs of polypropylene and untreated and silane-treated talc-filled polypropylene composites.* Polymer, 1999. **40**(19): p. 5345-5353.
138. Jayanarayanan, K., S. Thomas, and K. Joseph, *Morphology, static and dynamic mechanical properties of in situ microfibrillar composites based on polypropylene/poly (ethylene terephthalate) blends.* Composites Part A: Applied Science and Manufacturing, 2008. **39**(2): p. 164-175.
139. Sumita, M., et al., *Dynamic mechanical properties of polypropylene composites filled with ultrafine particles.* Journal of Applied Polymer Science, 1984. **29**: p. 1523-1530.
140. Turi, E., *Thermal characterization of polymeric materials.* 2nd Edition, Academic Press, Brooklyn, New York, 1997.
141. Clarke, R.L. and M. Braden, *Modified Arrhenius equation for the frequency dependence of the transition temperatures of polymers.* Biomaterials, 1989. **10**(5): p. 349-352.
142. Nitta, K.H. and A. Tanaka, *Dynamic mechanical properties of metallocene catalyzed linear polyethylenes.* Polymer, 2001. **42**(3): p. 1219-1226.
143. Pegoretti, A., *Creep and fatigue behavior of polymers nanocomposites.* at Nano- and micro- mechanics of polymer blends and composites. ed. Karger-Kocsis J., Fakirov S. Hanser Publications, Cincinnati, 2009: p. 301-339.

144. Wang, Z.D. and X.X. Zhao, *Modeling and characterization of viscoelasticity of PE/SiO_2 nanocomposite films under constant and fatigue loading.* Materials Science and Engineering: A, 2008. **486**(1–2): p. 517-527.
145. Joshi, M. and V. Viswanathan, *High-performance filaments from compatibilized polypropylene/clay nanocomposites.* Journal of Applied Polymer Science, 2006. **102**(3): p. 2164-2174.
146. Pegoretti, A., et al., *Recycled poly(ethylene terephthalate)/ layered silicate nanocomposites: morphology and tensile mechanical properties.* Polymer, 2004. **45**: p. 2751-2759.
147. Ranade, A., et al., *Maleated and non-maleated polyethylene–montmorillonite layered silicate blown films: creep, dispersion and crystallinity.* Polymer, 2005. **46**(18): p. 7323-7333.
148. Starck, P. and B. Löfgren, *Thermal properties of ethylene/long chain α-olefin copolymers produced by metallocenes.* European Polymer Journal, 2002. **38**(1): p. 97-107.
149. Ward, I.M., *Mechanical Properties of Solid Polymers* John Wiley and Sons LtD. Weinheim, 1983.
150. Findley, W.N., J.S. Lai, and K. Onaran, *Creep and relaxation of nonlinear viscoelastic materials: with an introduction to linear viscoelasticity.* Dover Publications Inc., New York, 1989.
151. Dorigato, A. and L. Fambri, *Thermo-mechanical behavior of polyamide 12—polyamide 66 recycled fiber composites.* Polymer Composites, 2011. **32**(5): p. 786-795.
152. Barus, S., et al., *Preparation of polymeric hybrid nanocomposites based on PE and nanosilica.* Polymer, 2009. **50**(12): p. 2595-2600.
153. Drozdov, A.D. and A. Dorfmann, *The stress-strain response and ultimate strength of filled elastomers.* Computational Materials Science, 2001. **21**: p. 395-417.
154. Fu, S.Y., G. Xu, and Y.W. Mai, *On the elastic modulus of hybrid. Particle/short fiber/polymer composites.* Composites Part B: Engineering, 2002. **33**: p. 291-299.
155. Lewis, T.B. and L.E. Nielsen, *Dynamic mechanical properties of particulate-filled composites.* Journal of Applied Polymer Science,, 1970. **14**: p. 1449-1471.
156. Nielsen, L.E. and R.F. Landel, *Mechanical Properties of Polymers and Composites.* Dekker, New York, 1994.
157. Klocek, P., *Handbook of Infrared Optical Materials. CRC Press.* 1991.
158. Nicolais, L. and L. Nicodemo, *Strength of particulate composite.* Polymer Engineering & Science, 1973. **13**: p. 469-477.
159. Szazdi, L., et al., *Quantitative estimation of the reinforcing effect of layered silicates in PP nanocomposites.* Polymer, 2006. **47**: p. 4638-4648.
160. Nielsen, L.E., *Simple theory of the stress-strain properties of filled polymers.* Journal of Applied Polymer Science, 1966. **10**: p. 97-103.
161. Dorigato, A., *Viscoelastic and fracture behaviour of polyolefin based nanocomposites.* PhD thesis, Department of Materials Engineering and Industrial Technologies, University of Trento 2009.

162. Silverstein, R.M., G.C. Bassler, and T.C. Morrill, *Spectroscopic identification of organic compounds,*. ed. Wiley, New York, 1991.
163. Vladimirov, V., et al., *Dynamic mechanical and morphological studies of isotactic polypropylene/fumed silica nanocomposites with enhanced gas barrier properties.* Composites Science and Technology, 2006. **66**: p. 2935-2944.
164. Wu, C.L., et al., *Tensile performance improvement of low nanoparticles filled-polypropylene composites.* Composites Science and Technology, 2002. **62**(10–11): p. 1327-1340.
165. Bikiaris, D.N., et al., *Compatibilisation effect of PP-g-MA copolymer on iPP/SiO_2 nanocomposites prepared by melt mixing.* European Polymer Journal, 2005. **41**(9): p. 1965-1978.
166. Srisawat, N., M. Nithitanakul, and K. Srikulkit, *Characterizations of fibers produced from polypropylene/silica composite.* Journal of Metals, Materials and Minerals, 2009. **19**: p. 53-58.
167. Liu, X. and Q. Wu, *PP/clay nanocomposites prepared by grafting-melt intercalation.* Polymer, 2001. **42**: p. 10013-10019.
168. Rottstegge, J., et al., *Polymer nanocomposite powders and melt spun fibers filled with silica nanoparticles.* Journal of Applied Polymer Science, 2007. **103**(1): p. 218-227.
169. Chiu, C.-W., C.-A. Lin, and P.-D. Hong, *Melt-spinning and thermal stability bahavior of TiO_2 nanoparticle/polypropylene nanocomposite fibers.* Journal of Polymer Research, 2011. **18**: p. 367-372.
170. Galeski, A., *Strength and toughness of crystalline polymer systems.* Progress in Polymer Science, 2003. **28**: p. 1643-1699.
171. Kroshefsky, R.D., J.L. Price, and D. Mangaraj, *Role of compatibilization in polymer nanocomposites.* Rubber Chemistry and Technology, 2009. **82**(3): p. 340-368.

Appendix I

Fiber spinning of polypropylene-kaolinite composites

A1. Materials

Isotactic polypropylene (PP, Sabic PP505P, MFI = 3.6dg/min) in the form of pellets was used as polymer matrix. As a nanofiller kaolinite (K, Paralux, supplied by Vale, Brasil) with specific surface area $12m^2/g$ and average diameter of about 0.9μm was selected. For the masterbach production a co-rotating intermershing twin-screw extruder Cextral BC21 (Firminy, France) was used, with increasing temperature profile from hopper to rod die from 150-200°C and with 250 rpm. The polypropylene – kaolinite (PP-K) masterbatch produced in this way and containing from 10 up to 30% by wt. of the filler was kindly supplied by Centre des Materiaux des Mines d'Alès – Ecole des Mines d'Ales, France.

A2. Experimental part – fiber spinning and drawing

Polypropylene fibers containing kaolinite in the range 1-30% wt. were produced in a two-steps process, i.e. compounding and melt-spinning.

Fibers were produced after direct mixing and compounding of selected formulation by using a Thermo Haake PTW16 intermeshing co-rotating twin screw extruder (screw diameter=16 mm; L/D ratio=25; rod die diameter 1.65 mm). The screws rotation speed was regulated depending on the melt flow of material in order to maintain residence time of 20 min and to produce nanofilled polyolefines fibers with diameter of about 500 μm. The temperature profile was gradually increased from hopper to rod die T_1 = 130 °C, T_2 = 200 °C, T_3 = 210 °C, T_4 = 220 °C, T_5 = 230 °C.

In the Table A1 designation and formulation of PP-K nanocomposites are reported. From the obtained MFI results it can be noted that the melt flow values decreases with the percentage of kaolinite in the polymer matrix with an almost linear dependence on the PP-K composition.

Sample	Polypropylene -PP [%]	Kaolinite -K [%]	MFI [dg/10min]
PP	100	0	3.61±0.07
PP-K1	99	1	-
PP-K3	97	3	-
PP-K10	90	10	3.28±0.02
PP-K20	80	20	2.59±0.02
PP-K30	70	30	1.67±0.02

Table A1. Designation and formulation of PP nanocomposites (in percentage by weight).

After melt spinning as- spun filaments with 500μm diameter were collected, and then drawn in air at 145°C, at various draw ratio (DR) from 5 to at least 15. All the fibers were characterized by misroscopy technique (TEM), thermal (TGA, DSC) and mechanical analysis.

A3. Results and discussion

A3.1 Morphology

The effect of compounding and the quality of kaolinite dispersion in PP matrix was tested by TEM analysis. The transversal cross section of PP-K20 fibers with 500μm is depicted in the Figure A1.

According to the TEM observations PP-K20 composite fiber shows homogeneous nanofiller dispersion within the polymer matrix. The nanofiller size are between 3μm up to 100nm.

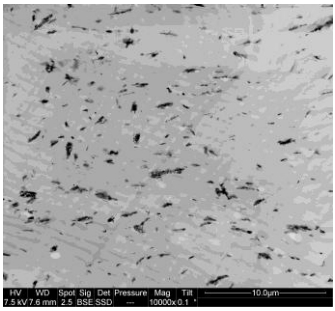

Fig. A1a. PP-K20 with magnification 10000x

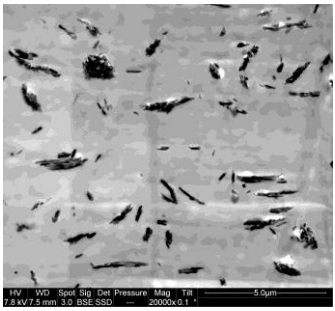

Fig. A1b. PP-K20 with magnification 20000x

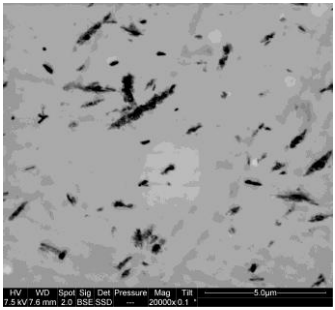

Fig. A1c. PP-K20 with magnification 20000x

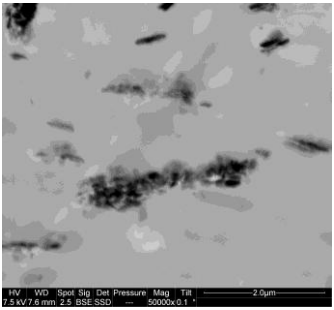

Fig. A1d. PP-K20 with magnification 50000x

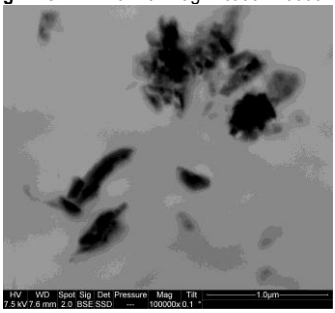

Fig. A1e.PP-K20 with magnification 100000x

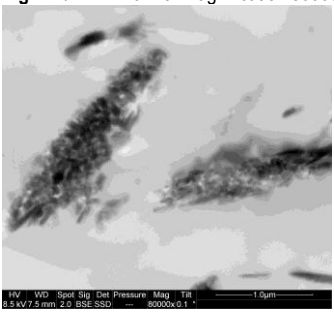

Fig. A1f. PP-K20 with magnification 100000x

Figure A1a-f. TEM micrograph of PP-K20 as-spun fiber performed at different magnification

A3.2. Thermal properties

In order to study the influence of nanofiller content on the thermal stability of polypropylene TGA analysis was performed. Representative TGA curves of as-spun fibers are reported in Figure A2. The results show one-step degradation for all samples evidencing the beneficial effect of kaolinite on the thermal stability for all the nanocmposite fibers in comparison to neat PP.

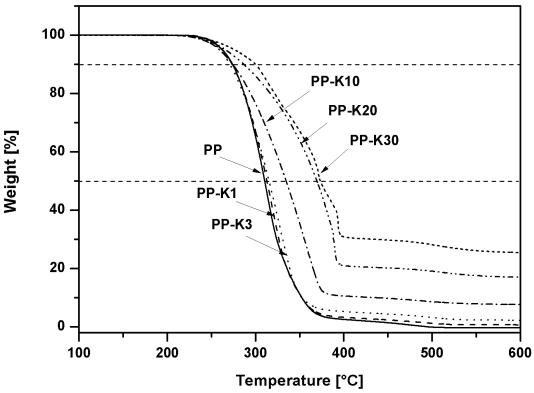

Figure A2.TGA curves of neat and nanofiller PP-K fibers under air atmosphere.

Sample	Temperature of 10% mass loss $T_{0.1}$ [°C]	Temperature of 50% mass loss $T_{0.5}$ [°C]	Residual mass at 600°C $m_{Residual}$ [%]
PP	271.3	310.0	0.0
PP-K1	273.0	312.6	0.9
PP-K3	273.6	315.4	2.6
PP-K10	275.0	335.0	7.5
PP-K20	287.6	370.3	17.3
PP-K30	303.0	374.5	25.4

Table A2. Results of TGA analysis of neat and nanofilled PP as-spun fibers performed under air atmosphere.

The decomposition temperature at which 10% and 50% mass loss occurred, and residual mass at 600°C were reported in Table A2. Obtained data proved that kaolinite positively affected the thermal degradation stability. It can be observed that for all of the compositions with nanofiller higher initial degradation temperature ($T_{0.1}$) was obtained in comparison to neat PP. At 50% weight mass loss an improvement of up to 5°C was observed for the compositions with 1-3% wt. of the filler, whereas in case of compositions with 10-30% wt. the degradation occurred at 25-60°C higher than that of neat PP. Residual mass at 600°C is directly dependent on the nanofiller content, ranging between 0.9% for PP-K1 up to about 25.4% for PP-K30 fibers. It can be concluded that the incorporation of the kaolinite into the polymer matrix enhances its thermal stability.

A3.3 DSC analysis

In Table A3 results of DSC analysis for as-spun and drawn PP-K fibers were reported.

Sample	DR	Melting Temperature [°C]	Crystallinity Content (I heating) X_c [%]	Crystallization Temperature [°C]	Crystallinity Content (cooling) X_c [%]
PP	1	162.0	41.3	113.2	46.3
	10	180.5	50.0	123.5	47.2
	15	175.0	50.4	123.5	46.2
PP-K1	1	162.7	46.5	117.8	50.7
	10	172.8	55.1	117.9	51.2
	15	179.8	58.7	116.0	50.2
PP-K3	1	162.2	44.4	122.3	51.3
	10	174.7	53.0	120.2	50.6
	15	177.1	57.7	119.4	50.0
PP-K10	1	164.2	44.7	124.2	54.2
	10	178.1	56.8	123.2	52.4
	15	176.6	56.7	123.1	51.2
PP-K20	1	163.7	42.8	121.0	53.1
PP-K30	1	163.5	44.6	123.4	51.1

Table A3. Results of the DSC analysis: melting temperature (T_m), crystallinity content (X_c) and crystallization temperature (T_c) for neat and nanofilled PP-K fibers at different draw ratio (DR) values.

From the DSC analysis it can be observed that the kaolinite presence raised the melting temperature (T_m) for all the compositions up to 10% wt. of the filler, while after the temperature starts to decrease. Similar behavior was also observed in case of crystallization temperature (T_c). The highest value was observed for PP-K10 composition and with higher nanofiller content the temperature starts to decrease. In case of crystallinity content for as-spun fibers, the values increases with the kaolinite presence from 46.3% for neat PP up to 54.2% with 10% wt. of the filler and similar as T_c and T_m for higher nanofiller amount starts to decrease.

Moreover, in the Table A3 for some compositions data obtained for drawn fibers (DR=10 and 15) were reported. It can be noted that for drawn nanofilled fibers, in particular for DR=15 higher melting temperature were observed in comparison to neat PP with. Similar behavior was observed if crystallinity content (in both cooling and heating scan). The improvement was from 5% up to 8% in case of nanofilled fibers in comparison to neat PP. However, lower crystallization temperature (T_c) in comparison to neat PP was observed for the compositions with 1 and 3% wt of kaolinite, while for PP-K10 the values were very similar to neat PP.

According to obtained results it can be concluded that in case of PP-K fibers kaolinite act as nucleating agent.

A3.4. Mechanical properties

In the Table A4 mechanical properties obtained for as-spun fibers were reported.

Sample	Elastic Modulus E [GPa]	Stress at yield σ_y [MPa]	Strain at yield ε_y [%]	Stress at break σ_b [MPa]	Strain at break ε_b [%]
PP	0.60±0.07	30.2±1.6	11.3±0.8	81.7±1.5	1276±25
PP-K1	0.58±0.03	26.2±1.5	12.0±0.5	77.6±2.0	1278±87
PP-K3	0.70±0.01	30.5±2.8	11.8±0.5	75.1±3.7	1343±30
PP-K10	1.00±0.17	39.0±3.5	10.0±2.6	66.8±2.0	1232±48
PP-K20	1.05±0.08	35.1±2.0	8.7±1.0	55.1±4.5	1017±67
PP-K30	1.12±0.06	30.3±3.0	3.5±0.5	43.6±3.6	861±70

Table A4. Quasi-static tensile properties of as-spun polypropylene-kaolinite nanocomposites with different nanofiller content.

It is important to underline that for all the compositions with high nanofiller content significantly higher elastic modulus was observed. In particular improvement from 0.60G Pa for neat PP up to 1.12 GPa for PP-K30 was obtained, while in case of compositions with 1 and 3% wt. the values were only slightly higher than for neat PP. Tensile stress at yield (σ_y) slightly increases for the compositions with high nanofiller content (PP-K10 and PP-K20) while for low nanofiller content (PP-K1) slightly lower values were observed. Improvement in yield strength can be a signal of good interfacial adhesion between filler and matrix. Enhancement of the elastic modulus and strength at yield was observed together with lower strain at yield, expecially very strong reduction was observed for the compositions with high nanofiller content (PP-K20 and PP-K30). If the properties at break will be compared it can be noted that significant reduction in stress and strain was observed for the compositions with high kaolinite content ,while for fibers with 1% and 3% wt. of filler stress at break was only slightly lower and in case of strain at break even small improvement (for PP-K3) was observed.

In the Figure A3, A4 and A5 elastic modulus, stress at break and strain at break for drawn fibers versus draw ratio were reported.

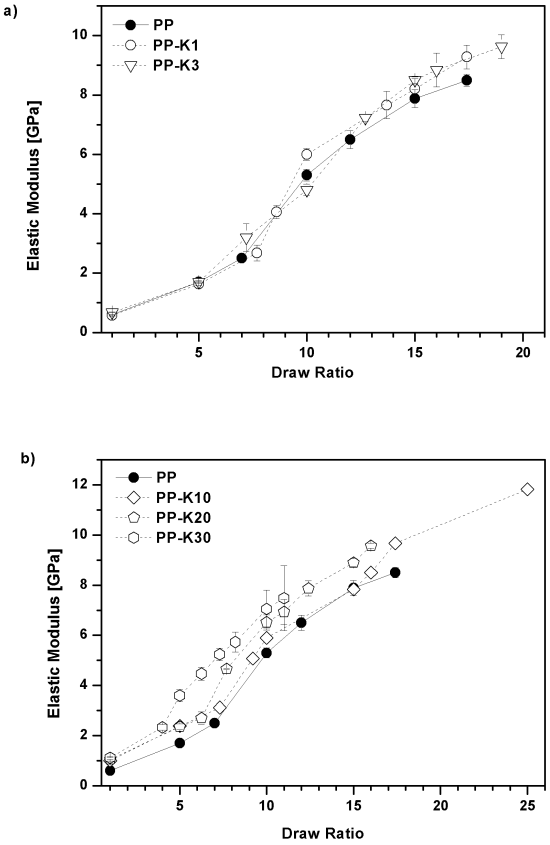

Figure A3. Elastic modulus properties of neat and nanofilled PP-K fibers (a) with low nanofiller content and (b) with high nanofiller content for different draw ratio.

In the Figure A3a elastic modulus versus draw ratio for nanocomposite PP-K fibers with low and in the Figure A3b with high nanofiller content were represented. In case of low nanofiller content (1% and 3% wt.) for low draw ratio (DR<10) no improvement in modulus was observed. Within the drawing process (for DR>) slightly higher elastic modulus for nanofiller fibers, improvement from 7.9 GPa for neat PP up to 8.2 GPa for PP-K1 and 8.5 GPa for PP-K3 at DR=15 was obtained. In the Figure A3b results for the compositions with nanofiller content from 10% up to 30% wt. were depicted. In case of the nanocomposite fibers enhancement in elastic modulus in all

draw ratio range was obtained. For example for DR=10 modulus raised from 5.3 GPa for neat PP up to 5.9 GPa for PP-K10, 6.5 GPa for PP-K20 and 7.1 GPa for PP-K30, while for DR=15 enhancement from 7.9 GPa for neat PP up to 8.9 GPa for PP-K20 was recorded. It is important to underline that for compositons with 10% wt. of kaolinite, better drawability with maximum modulus equal 12GPa was obtained (DR=25) in comparison to 8.5 GPa of neat PP (DR=17).

It is well known that the stress at break of compositions usually decreases with the addition of the nanofiller. In the Figure A4 a and b stress at break for low and high nanofiller content fibers were reported. For compositions with nanofiller content up to 3% wt., similar as in case of modulus, for low DR the same values were observed as for neat PP. However with the drawing process, stress at break increases and for DR=15 significant improvement was obtained. For example for DR=10 stress for neat PP was equal 775 MPa while for fibers with only 1% wt. stress equal 923 MPa and for 3% wt. of kaolinite 900 MPa was observed. For higher DR (DR=15) this improvement is even more significant and stress reached values of 1240 MPa and 1166 MPa for PP-K1 and PP-K3 respectively in comparison to 906 MPa for neat PP.

If the results for fibers with high kaolinite content will be taken into consideration, it can be seen that higher stress at break was observed only at higher draw ratio. In particular for DR=15, stess for neat PP (906MPa) was lower than reported for PP-K10 (990MPa), PP-K20 (932MPa) and PP-K30 (924MPa). It is important to underline that most of the time the stiffening effect is accompanied by reduction of the tensile properties at break, while in case of polypropylene kaolinite drawn fibers enhancement in stress at break was observed even for high nanofiller loadings.

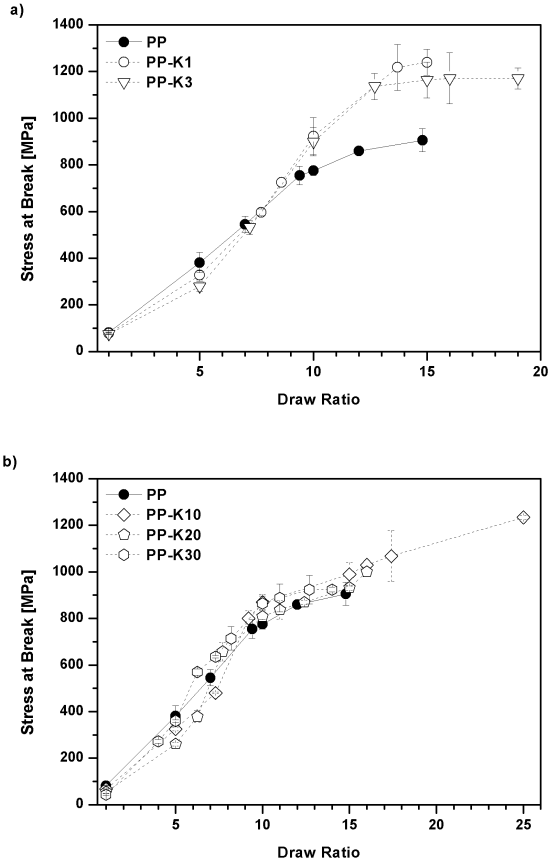

Figure A4. Stress at break properties of neat and nanofilled PP-K fibers (a) with low nanofiller content and (b) with high nanofiller content for different draw ratio.

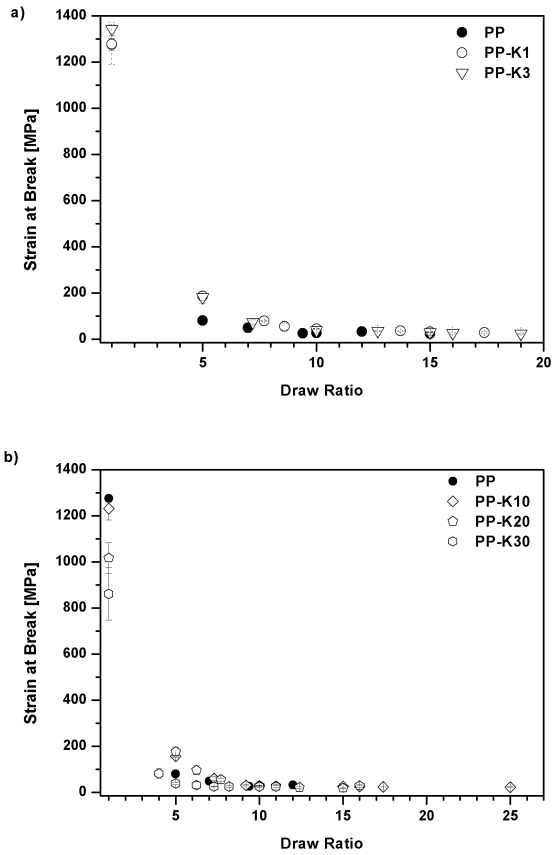

Figure A5. Strain at break properties of neat and nanofilled PP-K fibers (a) with low nanofiller content and (b) with high nanofiller content for different draw ratio.

In the Figure A5 strain at break for nanocomposite PP-K fibers with a) low and b) high nanofiller content were reported. As it can be expected for low nanofiller loading (Fig. 5A) no significant reduction in elongation at break was observed for nanofilled fibers. However, for fibers with high nanofiller content (Fig. 5b) significant reduction of strain at break was observed for low draw ratio, while with drawing process the behavior of neat and nanofiller fibers was very similar.

It can be concluded that for fibers drawn with higher draw ratio (DR>10) significant improvement in modulus observed together with enhancement in stress at break was obtained without affecting strain at break properties. This bahavior can be related to the homogeneous kaolinite dispersion inside the polymer matrix, that enhanced the filler-polymer intefacial adhesion and is responsible for the improvement of machanical properties.

A4. Summary PP-K fibers

PP composites with low (up to 3% wt.) and high (up to 30% wt.) kaolinite content were successfully prepared through melt spinning and hot drawing process. In both cases, the dispersion of nanoparticles enhanced the elastic modulus of PP positively affecting the stress at break and decreasing strain at break but only for compositions with high nanofiller content (20% and 30% wt.) at low draw ratio. Moreover, kaolinite significantly improved the thermla stability and crystallinity content acting as a nuclation agent. These results confirmed that polypropylene reinfored by kaolinite could be easily spinned into nanofilled fibers with better thermo-mechanical properties.

Future research

This are promissing results for the production of high quality fibers of nanocomposite polypropylene.

PUBLICATIONS AND CONGRESS PRESENTATIONS

PUBLICATIONS

Published

I. Dabrowska, .L Fambri, A. Pegoretti, G. Ferrara

Organically modified hydrotalcite for compounding and spinning of polyethylene nanocomposites.

eXPRESS Polymer Letter, No. 7 (2013) 936-949.

L. Fambri, I.Dabrowska, A. Pegoretti, R. Ceccato

Melt spinning and drawing of polyethylene nanocomposite fibers with organically modified hydrotalcite.

Journal of Applied Polymer Science, in press

In submission (Polymer Composite)

I. Dabrowska, .L Fambri, A. Pegoretti, G. Ferrara

Viscoelastic behavior of HDPE nanocomposites fibers.

In preparation

I. Dabrowska, *et al.*

Compounding and characterization of polypropylene-fumed silica nanocomposite.

I. Dabrowska, *et al.*

Melt spinning and drawing of polypropylene-fumed silica nanocomposite fibers.

Congress Presentations

I. Dabrowska, L. Fambri, A. Pegoretti, G. Ferrara

Perkalite organoclay for the production of nanocomposite polyethylene fibers.

Eurofillers 2011 – Oral presentation

Dresden, Germany 21-25 August 2011

I. Dabrowska, L. Fambri, A. Pegoretti

Compounding and spinning of polyolefins nanocomposites.

Sao Carlos Advanced School on Materials Science and Engineering - Poster
Sao Carlos, Brazil – 25-31 March 2012;

I. Dabrowska, L. Fambri, A. Pegoretti, G. Ferrara

Compounding and spinning of polypropylene nanocomposites with fumed nanosilica.

European Polymer Federation – EPF 2013 – Oral presentation

Pisa, Italy 16-21 June 2013

I. Dabrowska, L. Fambri, M. Batistella, J.-M. Lopez-Cuesta

Compounding and spinning of polypropylene nanocomposites with kaolinite.

16th European Conference On Composite Materials –ECCM 16 - Submitted abstract

Seville, Spain – 22-26 June 2014

Acknowledgements

I would like to express gratitude to Prof. Luca Fambri and Prof. Alessandro Pegoretti for giving me an opportunity to join they research group and they assistance, guidance and unconditional support during my PhD study.

I would gratefully thank Dr. Giuseppe Ferrara (LyondellBasell Industries-Basell Poliolefine Italia S.r.l. "Giulio Natta" R & D, Ferrara) for help in materials donation, TEM analysis and important suggestions during my PhD study.

I would like to thank Dr. Flavio Fava (Clariant Masterbatches (Italia) SPA) for help in materials donation and useful information during nanocomposite with Perkalite preparations.

I would gratefully thank Prof. Riccardo Ceccato for help with X-Ray Diffraction analysis on nanocomposites and helpful comments during paper preparation.

Moreover, I would like to thank Dr. Miroslav Slouf and Dr. Tatana Vackova (Institut of Macromolecular Chemistry, Praque, Czech Republic) for TEM analysis and Microhardness tests performed on polypropylene nanocomposites.

Furthermore, I would like to thank to Prof. Jose-Marie Lopez-Cuesta and dr. Marcos Batistella (Centre des Materiaux des Mines d'Alès, France) for a donation and opportunity to work with kaolinite nanocomposites.

In particular I would like to thank the technicians (Alfredo Casagranda, Claudia Gavazza) for their precious help in the experimental activity.

My special gratitude to all with whom I have shared everyday work and friendship: Ibrahim, Thiago, Luiz, Annalisa, Eleonora, Francesca, Matteo, Denis, Mauro, Andrea, Diego, and all the other colleagues.

Last but not least, I would gratefully thank my family for the loving support through all of these years, without them nothing would be possible. My parents, Danuta and Wlodzimierz, my sisters Aldona, Ewa and Karolina, and my grandmom Anna.

Trento, November 2013